NUREG/CR-3680

Relationship Between the Gas Conductivity and Geometry of a Natural Fracture

Prepared by T. W. Schrauf, D. D. Evans

University of Arizona

Prepared for
U.S. Nuclear Regulatory
Commission

GPO Printed copy price: $5.50

NUREG/CR-3680

Relationship Between the Gas Conductivity and Geometry of a Natural Fracture

Manuscript Completed: January 1984
Date Published: April 1984

Prepared by
T. W. Schrauf, D. D. Evans

Department of Hydrology and Water Resources
University of Arizona
Tucson, AZ 85721

Prepared for
Division of Health, Siting and Waste Management
Office of Nuclear Regulatory Research
U.S. Nuclear Regulatory Commission
Washington, D.C. 20555
NRC FIN B7291
Under Contract No. RES-04-81-224

ABSTRACT

In recent years considerable interest in determining the relationship between the hydraulic conductivity of a rock fracture and its average aperture has developed. The present study involved both theoretical and experimental studies of the geometrical factors which influence gas conductivity of rock fractures. Theoretical analysis of parallel plate gas flow revealed that the gas conductivity of a fracture is the same as for incompressible fluids and can be expected to follow a cubic law relationship. Application of the cubic law to practical field test situations, however, was found to be limited by uncertainties in flow boundary conditions, nonlinearity of flow behavior, and effects of fracture surface roughness. Quantitative assessment of uncertainties in flow boundary conditions including elliptical injection boundaries, secondary intersecting fractures, and estimation of effective radius was performed. Nonlinear flow behavior was also analyzed and the results applied to measurements of gas flow rate through a single natural fracture. Evaluation of these results suggested a general flow equation of the form: $-(dp/dx) = av + bv^2$, where a and b are constant coefficients defined by a fracture's average aperture and surface roughness.

TABLE OF CONTENTS

	Page
ABSTRACT	iii
TABLE OF CONTENTS	v
LIST OF FIGURES	vii
LIST OF TABLES	ix
EXECUTIVE SUMMARY	1
1. INTRODUCTION	3
1.1 Description of Problem	3
1.2 Objective and Scope of Work	5
1.3 Previous Work	5
1.3.1 Parallel Plate Studies	6
1.3.2 Rock Fracture Studies	8
2. THEORETICAL DEVELOPMENT	11
2.1 Gas Conductivity of a Fracture	11
2.1.1 Validity of Parallel Plate Model	11
2.1.2 Derivation of Cubic Law for Gas Flow	11
2.2 Parallel Plate Gas Flow Equations	16
2.2.1 Continuity Equation	16
2.2.2 Linear Flow Equations	17
2.2.3 Non-Linear Flow Equations	24
2.3 Factors Influencing Gas Flow Rates	28
2.3.1 Limitations on the Cubic Law for Gas Flow	29
2.3.2 Elliptical Fracture Intercepts	30
2.3.3 Intersecting Fractures	32
2.3.4 Effective Radius	35
2.4 Relationship between Average and Deformation Apertures	38

TABLE OF CONTENTS--Continued

	Page
3. LABORATORY MEASUREMENTS	41
3.1 Experimental Approach	41
3.1.1 Sample Preparation	41
3.1.2 Measurement of Sample Stress-Strain Behavior	43
3.1.3 Experimental Apparatus	43
3.1.4 Test Procedures	57
3.2 Experimental Results	61
3.2.1 Fracture Aperture Measurements	61
3.2.2 Fracture Flow Measurements	69
4. DISCUSSION OF RESULTS	81
4.1 Comparison of Average and Deformation Apertures	81
4.2 Evaluation of Flow Equation Constants	81
5. CONCLUSIONS AND SUMMARY	105
6. LIST OF SYMBOLS	107
7. GLOSSARY OF SELECTED TERMS	110
8. REFERENCES CITED	111
APPENDIX A. SUMMARY OF FINITE DIFFERENCE MODEL RESULTS	114
APPENDIX B. FRACTURE POROSITY TEST DATA	115
APPENDIX C. FRACTURE FLOW TEST DATA	123

LIST OF FIGURES

Figure		Page
1.1	Flow regime chart	7
2.1	Fluid flow through a fracture	13
2.2	Linear flow field pressure distribution for $P_1 = 2P_2$	19
2.3	Comparison of isothermal and adiabatic flow rates	21
2.4	Radial pressure distribution for $P_1 = 2P_2$ and $R_2 = 10R_1$	23
2.5	Ratio values versus pressure squared gradient for e = 100 μm	31
2.6	Effect of deviation angle on radial flow rate	33
2.7	Definition of fracture inflows and outflows	34
2.8	Effect of intersecting fracture on radial flow rate	36
2.9	Dependence of flow rate on effective radius	37
2.10	Three fracture deformation models	39
3.1	Photograph of fracture surface	42
3.2	Stress-strain curve for sample no. 1, 4th and 5th load cycles	45
3.3	Stress-strain curves for sample no. 2, 1st, 2nd, and 3rd load cycles	46
3.4	Schematic of flow regulating and monitoring manifold	47
3.5	Detail of sample boundary girdle	49
3.6	Detail of center hole piping	50
3.7	Schematic of air pycnometer and pressure monitoring manifold	52
3.8	Photograph of sample loading frame	53
3.9	Photograph of data monitoring system	54
3.10	Air pycnometer diagram	56
3.11	DCDT drift measurements	58
3.12	Sample boundary conditions during testing	59
3.13	E_v and E_d versus applied normal stress for porosity test no. 1	62
3.14	E_v and E_d versus applied normal stress for porosity test no. 1 (loading cycle only)	63
3.15	E_v and E_d versus applied normal stress for porosity test no. 2 (loading cycle only)	64
3.16	E_v and E_d versus applied normal stress for linear flow field tests	67
3.17	Summary of aperture measurements for linear flow field tests	68
3.18	E_v and E_d versus applied normal stress for radial flow field tests	70
3.19	Pressure-flow rate data for all linear flow field tests with n = 2	72

LIST OF FIGURES--Continued

Figure		Page
3.20	Pressure-flow rate data for linear flow field tests no. 1-5, 9, and 10 with n = 2	73
3.21	Summary of aperture measurements for radial flow field tests	74
3.22	Injection pressure correction for radial flow field tests	75
3.23	Pressure-flow rate data for all radial flow field tests with n = 2	76
3.24	Pressure-flow rate data for radial flow field tests no. 1-6 with n = 2	77
3.25	Pressure-flow rate data for all radial flow field tests with n = 1.82	79
3.26	Pressure-flow rate data for all radial flow field tests no. 1-6 with n = 1.82	80
4.1	E_v versus E_d for porosity test no. 1	82
4.2	E_v versus E_d for porosity test no. 2	83
4.3	E_v versus E_d for linear flow field tests	84
4.4	Relationship between average and hydraulic apertures	88
4.5	Curve fits for differing values of the parameter λ	90
4.6	Curve fits for differing values of JRC	92
4.7	Fracture surface roughness profile	93
4.8	Relationship between e_h and $\bar{e}$	95
4.9	Frequency histogram of surface angularity	97
4.10	Measured and predicted values of the nonlinear coefficient C	100

LIST OF TABLES

Table		Page
1.1	Comparison of Cubic Law and Experimental Conductivities	9
3.1	Stress-Strain Measurements for Intact Granodiorite Samples	44
3.2	Comparison of Fracture Volume Measurements for Different Test Configurations	65
4.1	Linear Flow Field Test Results	86
4.2	Radial Flow Field Test Results	87
4.3	Surface Roughness Permeability Reduction Factors	89
4.4	Surface Angularity Permeability Reduction Factors	96
4.5	Nonlinear Flow Factors	102
A.1	Determination of the Effect of Single Intersecting Fracture	114
B.1	Porosity Test No. 1	116
B.2	Porosity Test No. 2	118
B.3	Linear Flow Field Test-Fracture Porosity Data	120
C.1	Linear Flow Field Test	124
C.2	Radial Flow Field Test	128

RELATIONSHIP BETWEEN THE GAS CONDUCTIVITY AND GEOMETRY OF A NATURAL FRACTURE

JANUARY, 1984

EXECUTIVE SUMMARY

The objective of this study was to determine the relationship between the measured conductivity and average aperture of a natural fracture. This relationship provides the tool for indirectly measuring apertures of in situ fractures using borehole injection tests. Aperture and aperture distribution is one of the principal fracture parameters needed to characterize unsaturated flow in fractured rock. In this regard this study is but a small portion of a larger study to develop the capability for characterizing unsaturated fractured rock at proposed radioactive waste repository sites.

A brief review of previous work indicates that very little experimental data exists on the relationship between the aperture and conductivity of a natural fracture. Furthermore, interpretation of existing data is conflicting in part due to the lack of a consistent method for independently measuring the aperture of a fracture. This study was motivated by the existing confusion.

Theoretical consideration was given first to deriving basic pressure-flow rate equations using a parallel plate model. As gas is used as a testing fluid in the unsaturated zone, special consideration had to be given to compressible fluid flow. Results indicated that the fracture conductivity for compressible fluid flow was essentially identical to that for incompressible fluid flow for all flow velocities of practical interest. Nonlinear flow equations were also developed to account for nonlinear effects associated with irregularities of the fracture walls. While such effects could not be described precisely, dimensional analysis was used to provide a usable equation.

Consideration was also given to factors influencing in situ measurement, particularly with regard to deviations from assumed boundary conditions. Factors considered included elliptical injection boundaries, such as those created by nonperpendicular borehole/fracture plane intercepts, and intersecting secondary fractures.

Experimental work was undertaken using a large block of granodiorite containing a single natural fracture. Fracture aperture was measured directly by measuring fracture volume and dividing by the fracture area. This provided an independent estimate of fracture aperture which had not been available in previous fracture flow studies. Fracture closure was also measured independently and found to agree quite closely with changes in fracture aperture as determined from fracture volume

measurements. This close agreement suggests that fracture closure is largely related to improved mating of the fracture surfaces rather than deformation or crushing of surface asperities.

Fracture flow rate was measured as a function of injection pressure for apertures ranging from 200 to 600 microns using nitrogen gas as the testing fluid. Both linear and radial flow field geometries were used for these tests. Results indicated that the flow was generally nonlinear and well described by an equation of the form: $-dp/dx = av + bv^2$ where p is pressure, v is velocity, and a and b are constants given by the linear and nonlinear conductivities, respectively. The linear conductivity was found to be less than that predicted using a parallel plate model although the reduction was attributable to surface roughness and well described by existing empirical equations.

1. INTRODUCTION

1.1 Description

Fractures are important conduits for water movement within rock masses. Rock fractures often contribute substantially to rock mass permeability and porosity, particularly when the intact rock permeability and porosity are low. Additionally, fracture systems often influence flow directions and flow velocities. Herein the term fracture includes not only rock joints, or discontinuities with no shear displacement, but all significant rock discontinuities characterized by a small but open aperture.

Interest in the flow behavior of fracture systems arises in a number of practical applications. Commonplace among these are leakage and stability of dam foundations, mine drainage, slope stability, and well production characteristics. Considerable recent interest in fracture flow pertains to siting of high-level nuclear waste repositories. Such repositories are generally sited in low permeability rock types whose flow characteristics are dominated by rock fractures. Consequently accurate estimation of contaminant leakage rates as well as travel times and paths require assessment of the flow behavior of existing fracture systems. As some repositories may be sited within the unsaturated zone, consideration must also be given to estimating the moisture potential at which fractures drain and the capability for outflux of gaseous contaminants through drained fractures.

While fractured media have often been treated in terms of equivalent porous media, this approach becomes less desirable as fracture spacing and regularity of fracture systems increase. An alternative approach is to stochastically model a fracture system using the frequency distributions of its primary parameters, namely: orientation, areal extent, and conductivity. Fracture conductivity (see Glossary) is a function of both fracture aperture and surface characteristics such as roughness and contact area. In unsaturated flow, fracture aperture also determines the moisture potential at which a fracture will drain. Hence a means of measuring fracture aperture distributions is essential to a meaningful stochastic fracture model.

At present, no satisfactory means of direct aperture measurement is available. The effects of stress relief, blast damage, and/or drilling damage enlarge apparent fracture apertures as measured along exposed fracture traces. An alternative indirect approach is to measure a fracture's conductivity and compute an associated aperture on the basis of the relationship:

$$q = k_f \, e \, g\gamma(dh/dx)/\mu \qquad (1.1)$$

where q = flow rate per unit width of fracture, k_f = intrinsic permeability, e = average fracture aperture (see Glossary), γ = density of the fluid, g = gravitational acceleration, dh/dx = hydraulic gradient, and μ = the absolute viscosity of the fluid.

For flow between smooth parallel plates, $k_f = e^2/12$, and equation (1.1) becomes:

$$q = \frac{e^3 \gamma g}{12\mu} \frac{dh}{dx} \qquad (1.2)$$

Equation (1.2) is often referred to as the cubic law and has been commonly used to model fracture flow. Considerable controversy exists over the validity of the cubic law for rough natural fractures as experimental data are sparse and conflicting.

Much of the confusion regarding interpretation of experimental data on fracture flow is attributable to the difficulty of independently estimating the average aperture (see Glossary) of a fracture. Direct measurement is difficult since the apertures of natural fractures vary across the fracture surface. In previous experimental work, the average aperture of a natural fracture has been determined by estimating the smallest observed average aperture and then using measurements of aperture deformation (see Glossary) to determine relative changes in average aperture. The difficulty of this approach has been lack of an accurate, or even a standard, means of estimating the smallest observed aperture. Secondly, the method tacitly assumes that measured aperture deformation equals average aperture change which may not be the case at higher stress levels when contact area is large. The results have led to conflicting conclusions.

Another uncertainty is the applicability of the cubic law to the flow of compressible fluids, particularly highly compressible fluids such as gases. Interest in gas flow arises from its use as a test fluid within the unsaturated zone. Gas is preferable to water for this purpose as it eliminates the need to consider the effects of gravity and partial saturation although the thermodynamic character of the fluid expansion must then be considered.

Further difficulties in application of the cubic law arise from factors which influence the hydraulic gradient and hence the measured flow rate in test situations. For example, nonlinear flow behavior has been observed for rough natural fractures (Sharp, 1970; Iwai, 1976) under pressure gradients characteristic of field test gradients. The hydraulic gradient is also affected by the assumed boundary conditions. In the majority of field tests radial flow within a single fracture plane is induced by injection or withdrawal of fluid through a single borehole

intersecting the tested fracture. Uncertainties in boundary conditions arise from: elliptical injection boundaries caused by nonperpendicular intersection of the borehole axis with the fracture plane; flow branching caused by intersection of the tested fracture with secondary fractures; and estimation of an effective radius.

In this investigation the relationship between fracture conductivity and average fracture aperture is examined both theoretically and experimentally in an effort to either validate the cubic law or provide a usable substitute based on measurable fracture surface characteristics. Factors influencing field applications as discussed above are also studied and evaluated quantitatively. Details of the scope of this work are presented in the following section.

1.2 Objective and Scope of Work

The principal objective of this investigation was to determine the relationship between fracture conductivity as determined from fracture flow tests and average fracture aperture. This relationship provides the basis for either indirectly measuring average fracture apertures from flow test data or estimating fracture conductivity from direct measurement of average aperture. To this end the flow of gas through fractures was studied theoretically and then evaluated on the basis of simple laboratory tests.

One of the first considerations was the applicability of the cubic law to a highly compressible fluid such as gas. The problem was evaluated analytically and from this result simple analytical flow equations were obtained. Additionally the range of validity of the cubic law for gas flow was determined.

Uncertainty in radial flow field boundary conditions and their effect on observed flows was also reviewed and quantified. Factors included in this review were: elliptical versus circular injection boundaries, intersecting secondary fractures, and effective radius.

Laboratory studies were then conducted on a single natural fracture. The relationship between average and deformation fracture apertures was studied first by measuring fracture volume and deformation as functions of applied normal stress. Linear and radial flow field fracture conductivities were then measured as functions of both injection pressures and average fracture aperture. Unlike previous fracture flow studies, direct and independent determination of average fracture aperture was made by measurement of fracture volume.

1.3 Previous Work

Previous experimental work on flow through fractures is limited, particularly for rough natural fractures. The following review of previous

work in fracture flow summarizes the major studies of flow through parallel plate models and natural fractures.

1.3.1 Parallel Plate Studies

Much of the experimental data collected on fracture flow is based on flow between parallel plates constructed using a variety of man-made materials. The earliest comprehensive work on parallel plate flow of water was conducted by Lomize (1951) who studied the effect of aperture, surface roughness, and aperture variability (using wedge shaped and sinusoidal boundaries). Similar experiments were later performed independently by Louis (1969) with nearly identical results. A flow regime chart (Figure 1.1) which identified five distinct flow regions was formulated from these results. The cubic law (equation (1.2)) was found to be valid for Reynold's numbers (R_e) of less than 2300 and a surface roughness index (S) of less than 0.033. Reynold's numbers and roughness index are defined as:

$$R_e = \frac{2e\gamma v}{\mu} \tag{1.3}$$

and

$$S = \frac{\lambda}{2e} \tag{1.4}$$

where e = average aperture, γ = fluid density, v = fluid velocity, μ = fluid viscosity, and λ = mean height of surface asperities.

For boundary plates with a surface roughness index greater than 0.033, the observed flow rate in the laminar flow region was reduced by a factor C, which is inversely related to the surface roughness as given by (Louis, 1969):

$$C = \frac{1}{1 + 8.8(S)^{1.5}} \tag{1.5}$$

The surface roughness index of natural fractures is generally greater than 0.033 (Louis and Maini, 1970).

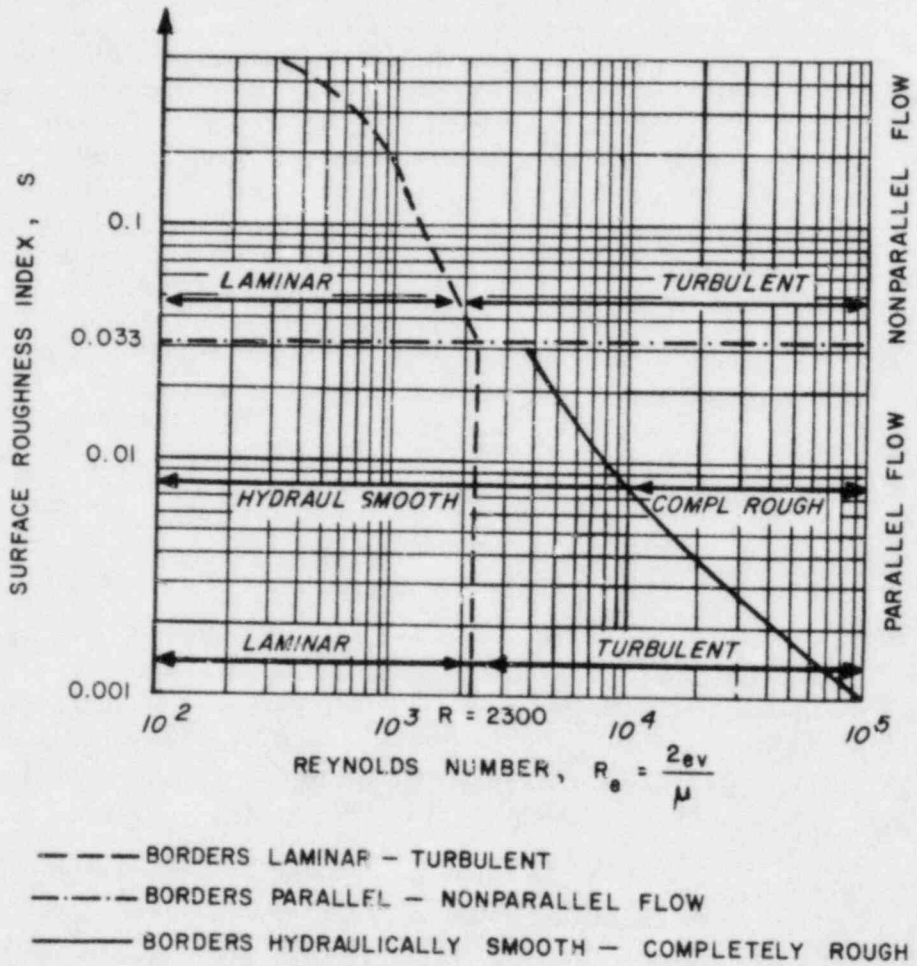

Figure 1.1. Flow regime chart.

Both studies discussed above were conducted on parallel plates with no contact points between the plates. Romm (1966) examined parallel plate flow through apertures as thin as 0.2 microns and confirmed the validity of the cubic law when applied to such superthin fractures.

1.3.2 Rock Fracture Studies

During the past several years, a number of studies of fluid flow through both natural and artificial rock fractures have been undertaken. Most of these studies have been concerned chiefly with the effect of applied stress on fracture conductivity and have not attempted to measure the relationship between fracture aperture and conductivity.

One of the earliest laboratory studies of flow through natural fractures (Sharp, 1970) examined one-dimensional water flow through a single fracture within a granite porphyry. Flow rates were measured for four different fracture apertures ranging from initial (normal stress equals sample weight) contact to a maximum increase of 130 microns. Fluid pressures were measured at several points along the flow path in order to delineate the areal pressure distribution across the fracture surface.

In all cases, Sharp observed that the flow rate was not a strictly linear function of applied hydraulic gradient as predicted by equation (1.2). Only the smallest aperture exhibited a linear relationship for hydraulic gradients less than 0.5. This nonlinearity was attributed to inertial losses and sporadic turbulence associated with the irregular boundaries of the fracture walls. Indeed, with the aid of an injected dye, Sharp was able to demonstrate channeling of the flow around points of contact. This observation was confirmed by the measured pressure distribution which indicated nonparallel equipotential lines.

The initial contact aperture was measured along one sample profile following completion of testing and found to average 270 microns although individual values ranged from 0 to nearly 600 microns. The equivalent hydraulic aperture, as calculated from equation (1.2), was found to be significantly larger (640 microns). This suggests some sample disturbance due to fracture extension between the direct and indirect determinations of initial contact aperture as the hydraulic aperture would be expected to be smaller than the average aperture.

Sharp developed equations of flow based on the effective aperture (minimum aperture tested = zero effective aperture) and concluded that flow rate varied as the square of the effective aperture. Based on Sharp's own calculations (Table 1.1), however, cubic law estimates of fracture conductivity were within 12% of measured for all apertures tested if the hydraulically determined aperture of 390 microns is used as a reference for converting the relative apertures to average apertures.

Table 1.1. Comparison of Cubic Law and Experimental Conductivities (after Sharp, 1970)

Effective Opening (μm)	Equivalent Parallel Plate Opening (μm)	Ratio Flow Rate/Hydraulic Gradient*		
		Cubic Law (cm^2/sec)	Experimental (cm^2/sec)	Ratio
250	640	183	171	1.07
510	890	502	571	0.88
1270	1650	3210	3430	0.94

*Based on slope of q/i as the hydraulic gradient $i \rightarrow 0$

A very comprehensive study of water flow through a single rock fracture was conducted by Iwai (1976) and involved both numerical and experimental work. Numerical models were formulated to evaluate the effect of boundary deviations from a parallel plate model, including deviation from a planar surface (fracture waviness), deviation from parallel sides (aperture variability), and reduction of flow cross section (increased contact area). While fracture waviness and aperture variability were both found to reduce resultant flow rates, these reductions were small, particularly for minor or moderate deviations. Reduction of flow cross section through increasing contact area was considerably more significant, with the expected flow rate decreasing hyperbolically with increasing contact area.

Iwai's experimental work consisted chiefly of measuring water flow rates as a function of fracture aperture. Core samples of basalt, marble, and granite were used for radial flow measurements by inducing tensile fractures perpendicular to the core axis. Two additional granite samples, one with a polished fracture surface, and one with a rectangular fracture surface for inducing one-dimensional (linear) flow, were also tested. Iwai's experimental results confirmed a cubic law relationship between flow rate and aperture. Fracture aperture changes were determined by externally measuring fracture deformation. The average fracture aperture was estimated by applying equation (1.2) to calculate the hydraulic aperture at the smallest observed flow rate (maximum observed closure) and adding the measured aperture change. Aperture sizes ranged from a few microns to a few hundreds of microns with most of the aperture variations achieved by normal loading of the sample fracture from the initial contact state. It is of note that the largest

deviations between average and hydraulic aperture were associated with the polished granite fracture probably as a result of increased contact area. Flow rates for the polished fracture were reduced slightly resulting in a nearly constant 15 micron reduction in computed hydraulic aperture.

Tests conducted on polished rock fractures by Kranz et al. (1979) and Engelder and Scholz (1981) have suggested inadequacies of the cubic law as applied to fracture flow. They found flow rates within thin fractures (less than 20 microns) were substantially reduced as an apparent consequence of reduction of cross sectional flow area. This reduction in cross-sectional area may be somewhat artificial considering the high applied stresses and smoothness of the polished fracture surfaces.

In situ measurements of fracture conductivity have been conducted (Pratt et al., 1977; Hardin et al., 1982) in association with direct measurements of joint deformation. Although the data appear to indicate lower flows than predicted by the cubic law, interpretation of the data is quantitatively difficult for several reasons:

(1) Analysis of the measured flow rate was complicated by uncertain boundary conditions;

(2) Saturated flow was assumed although water was used as the testing fluid within the unsaturated zone;

(3) Estimation of the initial aperture was uncertain;

(4) Joint deformations as measured on the exposed surface trace may not accurately reflect deeper subsurface fracture deformations.

2. THEORETICAL DEVELOPMENT

This chapter deals with the derivation of linear and nonlinear flow equations based on a parallel plate model for gas flow. Additionally, uncertainties in field measurement boundary conditions are examined and quantified in terms of their effect on measured flow rates. Finally, three fracture deformation models are examined to determine the relationship between average and deformation apertures when the fracture surfaces are in contact. The results form the basis for analyzing the laboratory measurements presented in Chapter 3.

2.1 Gas Conductivity of a Fracture

2.1.1 Validity of a Parallel Plate Model

As stated earlier, considerable controversy exists over the validity of a parallel plate model as applied to rough natural fractures. Indeed, numerous arguments exist against the use of a parallel plate model including:

(1) roughness of fracture surfaces;

(2) waviness of fracture surfaces; and

(3) contact between fracture surfaces.

Existing experimental and numerical data discussed in the previous chapter suggest that the magnitude of roughness and waviness effects are second order in comparison with the effect of contact area between fracture surfaces, at least for apertures under about 200 to 300 microns. As aperture increases, flow velocities are increased at similar pressure gradients; consequently roughness and waviness of the fracture surfaces become significantly more important by initiating turbulence and creating inertial forces.

The principal arguments in favor of a parallel plate model are that existing experimental data suggest it yields a very reasonable approximation of observed results and the limited amount of data available is insufficient to formulate a better model. It is important to note that while the hydraulic aperture and the average aperture may be different, existing experimental data indicate this difference to be a constant for any variation in the average aperture of a given fracture.

2.1.2 Derivation of Cubic Law for Gas Flow

For a viscous fluid with constant viscosity, the Navier-Stokes equation may be written:

$$\gamma \frac{D\underline{v}}{Dt} = -\nabla p + \gamma \underline{g} + \mu \nabla^2 \underline{v} + (K + \frac{\mu}{3}) \nabla(\nabla \cdot \underline{v}) \qquad (2.1)$$

where γ = fluid density, μ = fluid viscosity, ∇p = pressure gradient vector, $\underline{v}$ = velocity vector, $\underline{g}$ = gravity vector, K = bulk viscosity of the fluid, and D/Dt = total time derivative.

Considering one-dimensional laminar steady state gas flow through a fracture (Figure 2.1) and applying equation (2.1), we note:

(a) $\frac{D\underline{v}}{Dt} = (\gamma v_x \frac{\partial v_x}{\partial x}, 0)$ since flow is steady state and $v_y = 0$

(b) $\nabla^2 \underline{v} = (\frac{\partial^2 v_x}{\partial x^2} + \frac{\partial^2 v_x}{\partial y^2}, 0)$ since $v_y = 0$

(c) $\nabla(\nabla \cdot \underline{v}) = (\frac{\partial^2 v_x}{\partial x^2}, \frac{\partial^2 v_x}{\partial y \partial x})$ since $v_y = 0$

(d) $\gamma \underline{g} = (0,0)$ since γ is very small for gases

where the vectors are expressed in terms of their x and y components.

Hence, equation (2.1) reduces to:

$$(\gamma v_x \frac{\partial v_x}{\partial x}, 0) = -(\frac{\partial p}{\partial x}, \frac{\partial p}{\partial y}) + \mu(\frac{\partial^2 v_x}{\partial x^2} + \frac{\partial^2 v_x}{\partial y^2}, 0) + (K + \frac{\mu}{3})(\frac{\partial^2 v_x}{\partial x^2}, \frac{\partial^2 v_x}{\partial y \partial x}) \qquad (2.2)$$

Equation (2.2) may be rewritten as two separate equations for the x and y components, respectively:

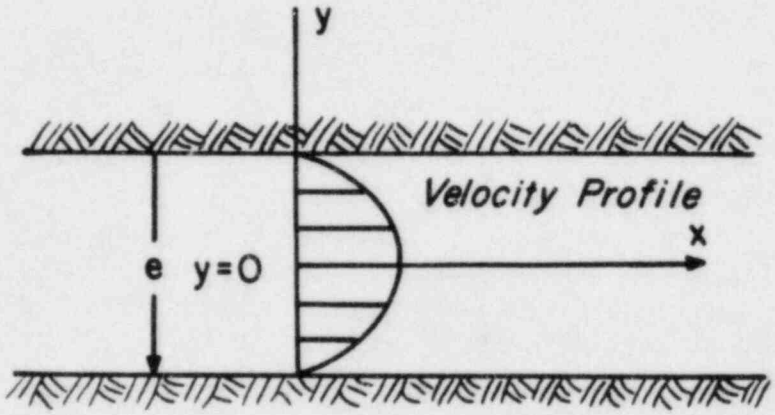

Figure 2.1. Fluid flow through a fracture.

$$\gamma v_x \frac{\partial v_x}{\partial x} = - \frac{\partial p}{\partial x} + \mu \left(\frac{\partial^2 v_x}{\partial x^2} + \frac{\partial^2 v_x}{\partial y^2} \right) + \left(K + \frac{\mu}{3} \right) \frac{\partial^2 v_x}{\partial x^2} \qquad (2.2a)$$

$$0 = - \frac{\partial p}{\partial y} + \left(K + \frac{\mu}{3} \right) \frac{\partial^2 v_x}{\partial y \partial x} \qquad (2.2b)$$

Solution of equation (2.2b) for the pressure distribution, $p(x,y)$, yields:

$$p(x,y) = \left(K + \frac{\mu}{3} \right) \frac{\partial v_x}{\partial x} + f(x) = g(x,y) + f(x) \qquad (2.2c)$$

Therefore we conclude that for strictly laminar flow, the pressure distribution is the sum of two functions. The first function varies with both x and y and is created by viscous forces associated with fluid dilation. The second function varies only with x and is associated with inertial and viscous forces directly associated with fluid flow in the x-direction. Intuitively it is expected that $f(x)$ is much larger than $g(x,y)$, and hence pressure can be considered for all practical purposes to vary only with x.

To solve equation (2.2) formally, we limit our discussion to slow flow (small values of v_x) and note in this case that inertial forces are negligible since:

$$\gamma v_x \frac{\partial v_x}{\partial x} = \frac{\gamma}{2} \frac{\partial v_x^2}{\partial x} \cong 0$$

when γ and v_x^2 are small.

Viscous forces associated with fluid dilation are also negligible since:

$$\frac{\partial^2 v_x}{\partial x^2} \text{ and } \frac{\partial^2 v_x}{\partial y \partial x} \cong 0$$

when v_x, or equivalently $\partial v/\partial x$ and $\partial \gamma/\partial x$, are small.

This simplification may also be valid when v_x is not small provided $(\partial v_x/\partial x)$ is very small compared with $(\partial v_x/\partial y)$. Just how small v_x must be in order that compressibility effects can be ignored is examined later in Section 2.3.1.

Equation (2.2a) now simplifies to nearly identical form with that obtained for an incompressible fluid:

$$\frac{\partial p}{\partial x} = \mu \frac{\partial^2 v_x}{\partial y^2} \tag{2.3}$$

where the hydraulic gradient is expressed solely by the pressure gradient since gravitational forces are negligible. As we have ignored viscous forces associated with fluid dilation, $(\partial p/\partial x)$ is considered independent of y. Hence integrating equation (2.3) twice with respect to y and applying the non-slip boundary conditions

$$v_x(e/2) = v_x(-e/2) = 0$$

to determine the constants of integration yields:

$$v_x = \frac{-1}{2\mu}\left(\frac{e^2}{4} - y^2\right)\frac{dp}{dx} \tag{2.4}$$

The maximum velocity occurs at y = 0, and is:

$$v_{max} = \frac{-e^2}{8\mu}\left(\frac{dp}{dx}\right) \tag{2.4a}$$

Integrating equation (2.4) over the profile width and dividing the result by the interval of integration, an equivalent average flow velocity is obtained:

$$v_{avg} = \frac{-e^2}{12\mu}\left(\frac{dp}{dx}\right) \tag{2.5}$$

The volumetric flow rate per unit width of fracture is q = v x e x 1, or:

$$q = \frac{-e^3}{12\mu} \left(\frac{dp}{dx}\right) \tag{2.6}$$

which is the familiar form of the "cubic law". Equations (2.5) and (2.6) are identical in form to Darcy's Law for porous media when the intrinsic permeability of the fracture is given by $e^2/12$.

2.2 Parallel Plate Gas Flow Equations

To apply equations (2.5) and (2.6) to fracture flow measurements, it is first necessary to describe the pressure distribution through space. In this section, the continuity equation is solved to provide analytical solutions for radial and linear flow rates as a function of fracture aperture and applied boundary conditions. This development parallels previous work by Muskat (1946) for porous media flow of gas and Maini (1971) for fracture flow of an incompressible fluid.

2.2.1 Continuity Equation

The equation of continuity for fluid flow is:

$$\nabla\cdot(\gamma\underline{v}) = -\left(\frac{\partial\gamma}{\partial t}\right) \tag{2.7}$$

Substitution of the pressure gradient ∇p for $\underline{v}$ as related by equation (2.5) in equation (2.7) results in:

$$\nabla\cdot(\gamma\nabla p) = \frac{12\mu}{e^2}\left(\frac{\partial\gamma}{\partial t}\right) \tag{2.8}$$

To express equation (2.8) in terms of a single dependent variable it is necessary to relate density to pressure. For an ideal gas, the equation of state is:

$$P = \frac{\gamma RT}{M} \tag{2.9}$$

where R = universal gas constant, T = absolute temperature, and M = molecular weight of the gas, P = absolute pressure.

For adiabatic conditions, T = a constant times $\gamma^{\left(\frac{1}{m} - 1\right)}$, where m = the ratio of specific heat at constant volume to that at constant pressure.

Hence equation (2.9) becomes:

$$\gamma = \gamma_o \, p^m \tag{2.10}$$

where γ_o = a constant of proportionality.

For an ideal gas under isothermal conditions, T = constant, m = 1, and γ_o = M/RT. Substitution of equation (2.10) into (2.8) yields;

$$\nabla^2 p^{m+1} = \frac{12(1+m)\mu}{\gamma_o e^2} \left(\frac{\partial p^m}{\partial t}\right) \tag{2.11}$$

While equation (2.11) is difficult to solve analytically because of its nonlinearity, Kirkham (1946) has indicated that for m = 1 and pressures very close to atmospheric (5 kPa gage pressure or less) equation (2.11) can be approximated to within 2.5% by:

$$\nabla^2 p_e = \frac{12\mu}{p_a e^2} \left(\frac{\partial p_e}{\partial t}\right) \tag{2.12}$$

where p_e = gage pressure, P_a = atmospheric pressure, which is identical to the form for incompressible fluids.

Under steady state conditions when $(\partial p^m/\partial t) = 0$, equation (2.11) takes the form of Laplace's equation for the variable p^{m+1}:

$$\nabla^2 p^{m+1} = 0 \tag{2.13}$$

Thus, for steady state gas flow the pressure distribution can easily be determined using existing solutions of Laplace's equation in terms of the variable p^{m+1}.

2.2.2 Linear Flow Equations

Two particular solutions of equation (2.11) are of interest in the present study: linear (one dimensional) flow, and radial flow between parallel constant pressure boundaries. While both adiabatic and isothermal flow are considered, gas flow through rock fractures is

considered to be closer to isothermal conditions since the mass and heat capacity of the rock is far greater than that of the gas.

2.2.2.1 Linear Flow Field. In a linear flow field the solution of equation (2.13) is:

$$P^{m+1}(x) = \frac{P_2^{m+1} - P_1^{m+1}}{L} x + P_1^{m+1} \qquad (2.14)$$

where P_1 = absolute pressure at x = 0 and P_2 = absolute pressure at x = L.

The pressure distribution described by equation (2.14) for air flow is presented in Figure 2.2 where pressure is expressed as a fraction of the injection pressure and distance as a fraction of the total flow path length. For the curves shown, $P_1 = 2P_2$, and m = 1 and 0.71 for the isothermal and adiabatic cases, respectively. Note the small difference in observed pressure distributions for the two thermodynamic extremes.

The pressure gradient is:

$$\frac{dP}{dx} = \frac{1}{(m+1)P^m} \frac{dP^{m+1}}{dx} = \frac{1}{(m+1)P^m} \frac{P_2^{m+1} - P_1^{m+1}}{L} \qquad (2.15)$$

Hence, equation (2.5) may be written as

$$v(P) = \frac{-e^2\alpha}{12(m+1)\mu} \frac{1}{P^m} \qquad (2.16a)$$

or

$$v(x) = \frac{-e^2\alpha}{12(m+1)\mu} [\alpha x + \beta]^{-m/(m+1)} \qquad (2.16b)$$

where

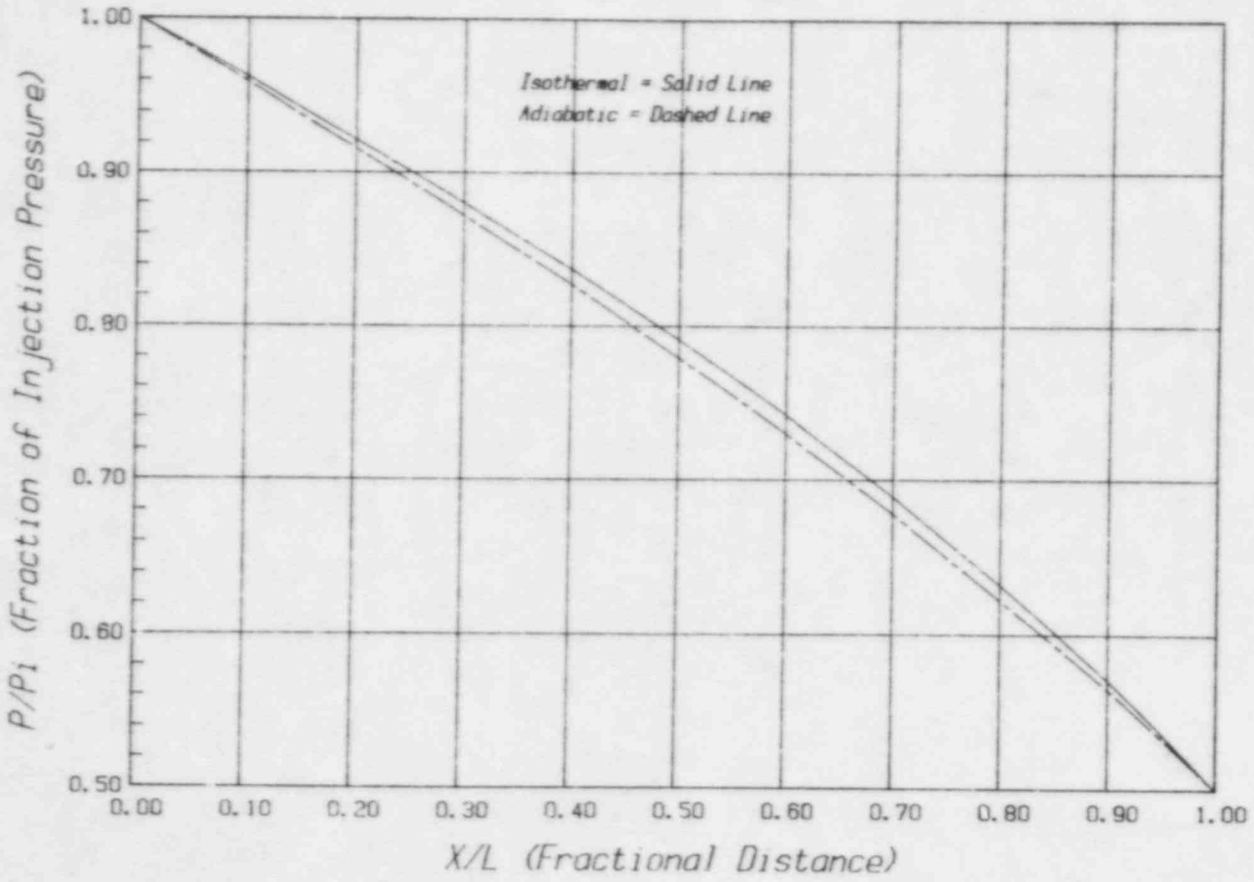

Figure 2.2. Linear flow field pressure distribution for $P_1 = 2P_2$.

$$\alpha = \frac{P_2^{m+1} - P_1^{m+1}}{L} \quad \text{and} \quad \beta = P_1^{m+1}$$

The volumetric flow rate per unit width of fracture flow cross-section may be determined directly from equations (2.16) by multiplying by the aperture width to yield:

$$q(p) = \frac{-e^3\alpha}{12(m+1)\mu} \left(\frac{1}{p^m}\right) \tag{2.17}$$

or equivalently in terms of the mass flow rate, $q_m = \gamma q$.

$$q_m = \frac{-e^3\alpha}{12(m+1)\mu} \left(\frac{\gamma}{p^m}\right) = \frac{-e^3\alpha\gamma_o}{12(m+1)\mu} \tag{2.18}$$

Hence, we find that the steady state mass flow rate is constant at any flow cross-section since γ_o = a constant. The ratio of adiabatic mass flow rate to isothermal mass flow rate is:

$$\frac{q_a}{q_i} = \frac{-2\gamma_a}{(1+m)\gamma_i} \frac{P_2^{m+1} - P_1^{m+1}}{P_2^2 - P_1^2}$$

$$= \frac{2}{(1+m)} \frac{1-(P_2/P_1)^{m+1}}{1-(P_2/P_1)^2} \tag{2.19}$$

This ratio is plotted for air flow (m = 0.71 for adiabatic case) in Figure 2.3 as a function of the ratio P_1/P_2. From this figure it is clear that the adiabatic flow rate is greater than the isothermal flow rate, particularly as the ratio P_1/P_2 increases. This results from the increased downstream density in adiabatic flow.

2.2.2.2 Radial Flow Field. For radial flow the solution of equation (2.13) is:

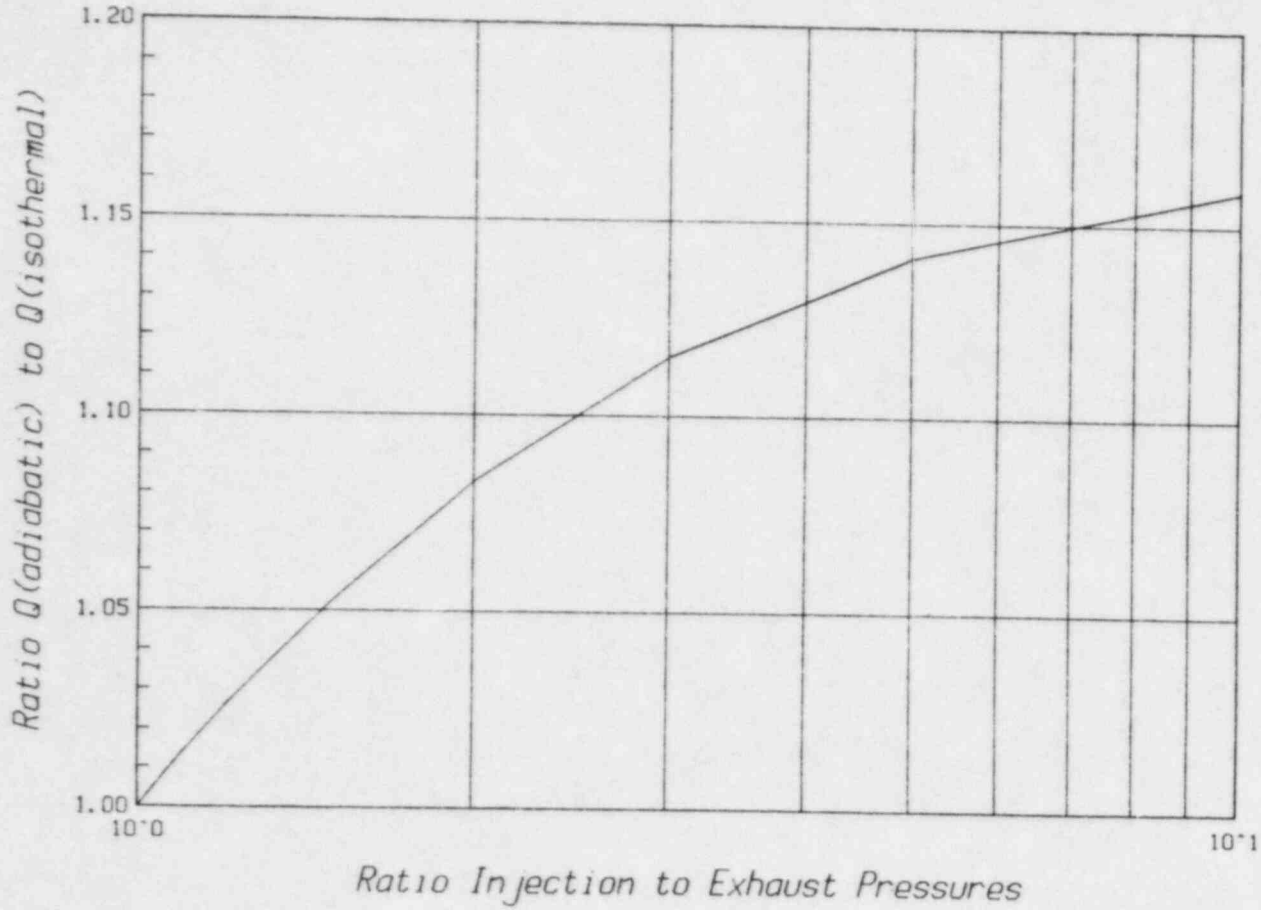

Figure 2.3. Comparison of isothermal and adiabatic flow rates.

$$p^{m+1}(r) = \frac{P_2^{m+1} - P_1^{m+1}}{\ln(r_2/r_1)} \ln(r/r_1) + P_1^{m+1} \qquad (2.20)$$

where P_2 = absolute pressure at r_2, $r_2 > r_1$, and P_1 = absolute pressure at r_1.

The pressure distribution described by equation (2.20) for air flow is presented in Figure 2.4 where pressure is expressed as a fraction of the injection pressure and distance as the ratio r/r_1. In the curves shown $P_1 = 2P_2$, $r_2 = 10r_1$, and m = 1 and 0.71. As for the linear case, small differences in pressure gradient are observed for the two cases. The pressure gradient is given by:

$$\frac{dp}{dr} = \frac{1}{(m+1)p^m} \frac{P_2^{m+1} - P_1^{m+1}}{\ln(r_2/r_1)} \frac{1}{r} \qquad (2.21)$$

Therefore equation (2.5) becomes:

$$v(r) = \frac{-e^2\alpha}{12(m+1)\mu} \frac{1}{r} [\alpha \ln(r) + \beta]^{-m/(m+1)} \qquad (2.22)$$

where

$$\alpha = \frac{P_2^{m+1} - P_1^{m+1}}{\ln(r_2/r_1)} \quad \text{and} \quad \beta = P_1^{m+1} - \alpha \ln(r_1)$$

Hence, the flow rate per unit depth of fracture is:

$$q = \frac{-e^3\alpha}{12(m+1)\mu} \frac{1}{p^m} \frac{1}{r} \qquad (2.23)$$

The total mass flow rate, Q_m, is given by:

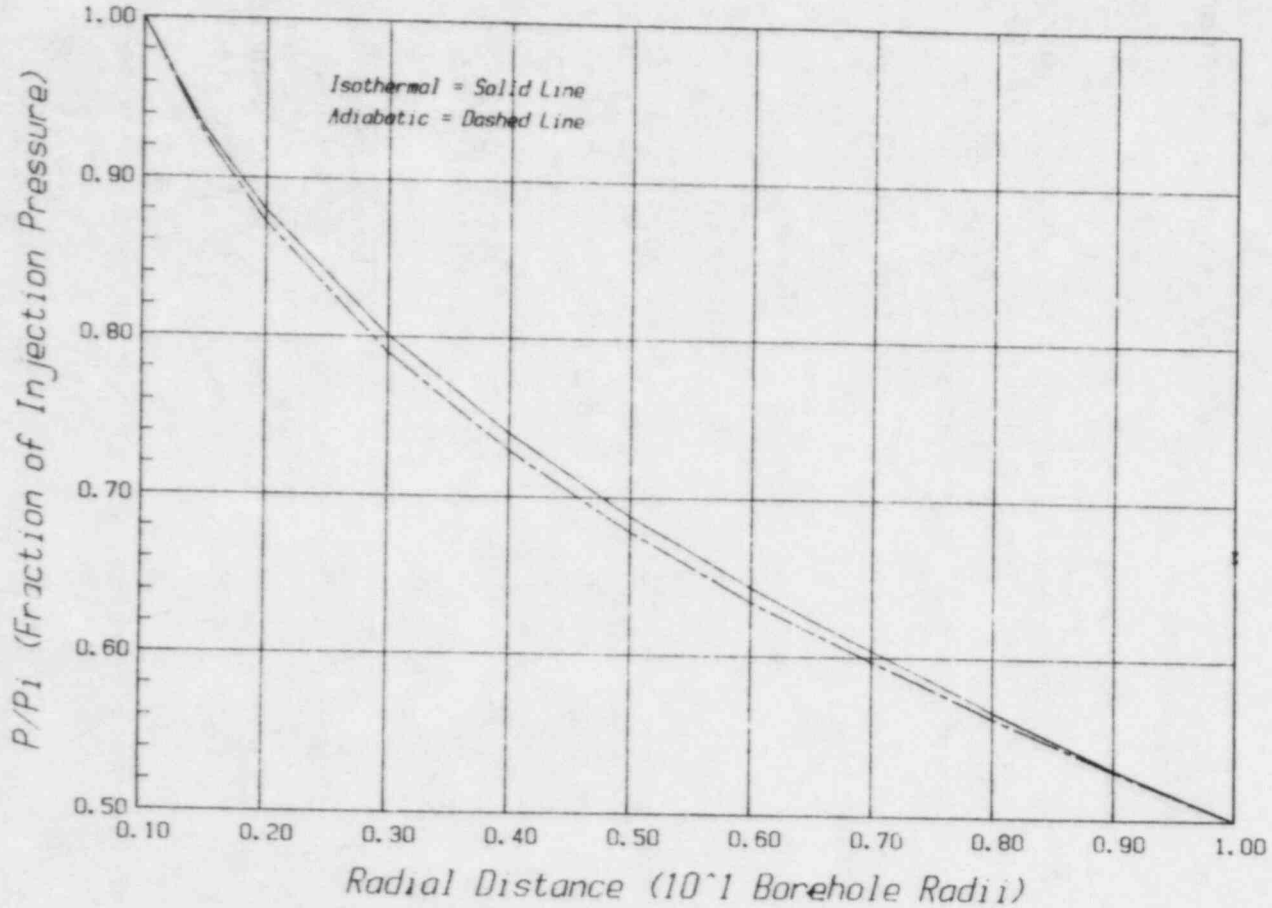

Figure 2.4. Radial pressure distribution for $P_1 = 2P_2$ and $R_2 = 10\ R_1$.

$$Q_m = \int_0^{2\pi} \gamma \, rq \, d\theta = \frac{-\pi e^3 \gamma_o \alpha}{6(m+1)\mu} \qquad (2.24)$$

The ratio of the adiabatic to isothermal mass flow rates is identical to that for a linear flow field (equation (2.19)).

2.2.3 Non-Linear Flow Equations

In the preceding sections, flow equations were derived assuming a linear relationship between the pressure gradient and mass flux of the fluid, as expressed by equation (2.5). Non-linear, or non-Darcian, flow may occur as a result of inertial losses arising from:

(1) entrance and exit losses along fracture injection or exhaust boundaries;

(2) changes in flow velocity along the flow path;

(3) initiation of turbulent flow.

Entrance and exit losses result from sudden changes in fluid velocity and turbulent eddy formation at points of abrupt change in flow cross sections. Changes in flow velocity along the flow path occur as a result of (1) changes in fluid density; (2) divergence of the flow paths, where the flow path width does not remain constant; and (3) tortuosity of the flow path around points of fracture surface contact. The last of these also contributes to localized eddy formation and consequent initiation of turbulent flow.

Inertial losses are generally proportional to the square of the velocity as these losses involve the kinetic energy of fluid masses. Under certain conditions, such as the existence of a viscous boundary layer, inertial losses may vary with the 1.75 to 1.85 power of velocity. Turbulent flow through smooth pipes is an example of this latter phenomenon.

To account for inertial energy losses, equation (2.5) may be written as (for example, see Muskat, 1946):

$$-\frac{dp}{dx} = av + bv^n \qquad (1.6 < n < 2.0) \qquad (2.25)$$

where a and b are constants dependent on the fluid properties and fracture geometry.

To evaluate the constant a, we note that as $v \to 0$, $v >> v^n$, and hence equation (2.25) approaches equation (2.5).

Due to the mathematical complexity of a fracture's geometry and the uncertainty in the source of the nonlinear term, exact evaluation of the coefficient b is not possible. Ward (1964) evaluated the coefficient b using dimensional analysis. He showed that for porous media if it is assumed that:

$$- \frac{dp}{dx} = f(v,k,\gamma,\mu) \tag{2.26}$$

where f = an unknown function and k = intrinsic permeability of the medium, then:

$$- \frac{dp}{dx} = f(v^w k^{(w-3)/2} \gamma^{w-1} \mu^{2-w}) \tag{2.27}$$

where w is the exponent of velocity. Combining equations (2.25) and (2.27) yields:

$$- \frac{dp}{dx} = \frac{\mu}{k} v + c\mu^{2-n} \gamma^{n-1} k^{(n-3)/2} v^n \tag{2.28}$$

where c represents a dimensionless constant. Although Ward found that c was a constant for a variety of porous media tested, Arbhabhirama and Dinoy (1973) found that c increased with increasing grain size. Intuitively this makes sense as the tortuosity (nonlinearity) of the flow paths increases with increasing grain size.

To account for density changes in gas flow, equation (2.28) is multiplied by γ to yield:

$$- \frac{dp^{m+1}}{dx} = \frac{(m+1)\mu}{\gamma_o k} v_m + \frac{(m+1)c\mu^{2-n}}{\gamma_o} k^{(n-3)/2} v_m^n \tag{2.29}$$

where $v_m = \gamma v$, the mass flux per unit area.

In terms of the measured total mass flow rate Q_m:

$$- \frac{dp^{m+1}}{dx} = \frac{(m+1)\mu}{\gamma_o k} \frac{Q_m}{w_f e} + \frac{(m+1)c}{\gamma_o} \mu^{2-n} k^{(n-3)/2} \frac{Q_m}{w_f e} \qquad (2.30)$$

where w_f = the width of the flow cross section.

To apply equation (2.30) to isothermal flow (m = 1) under specific boundary conditions we integrate along the flow path between the known boundary conditions. Implicit in this approach is the assumption that nonlinear inertial losses occur along the flow path only. This assumption is believed to be reasonable for very rough natural fractures and is supported by theoretical and experimental results presented in following sections.

For linear flow tests (linear being used here to denote parallel flow paths), $w_f = w_s$, the sample width; hence:

$$p_1^2 - p_2^2 = \frac{2\mu}{\gamma_o k} \frac{L}{e w_s} Q_m + \frac{2c}{\gamma_o} \mu^{2-n} k^{(n-3)/2} \frac{L}{e^n w_s^n} Q_m^n \qquad (2.31a)$$

or

$$p_1^2 - p_2^2 = a_\ell Q_m + c b_\ell Q_m^n \qquad (2.31b)$$

where a_ℓ and b_ℓ are constants related to the linear flow geometry and fluid properties.

For this special case v_m is constant along the flow cross section, and hence the pressure gradient is unchanged by inertial losses occurring over the flow path length.

If n = 2, we can define a Reynold's number R_k as the ratio of nonlinear to linear terms, or:

$$R_k = \frac{\gamma v k^{1/2}}{\mu} = \frac{b_\ell}{a_\ell} Q_m \qquad (2.32)$$

R_k differs from previous definitions of Reynold's numbers for fracture flow in that the characteristic length is $k^{1/2}$ instead of the hydraulic diameter, 2e, or radius, e/2, as used by others.

The associated friction factor, F_k, is:

$$F_k = - \frac{k^{1/2}}{\gamma} \frac{1}{v^2} \frac{dp}{dx} = \frac{1}{b_\ell} \frac{p_2^2 - p_1^2}{Q_m^2} \tag{2.33}$$

Equation (2.31) may be rewritten in terms of the dimensionless variables R_k and F_k as:

$$F_k = \frac{1}{R_k} + c \tag{2.34a}$$

In the linear or Darcian flow regime, $1/R_k >> c$ and:

$$F_k = \frac{1}{R_k} \tag{2.34b}$$

In the fully turbulent flow regime $c >> 1/R_k$ and:

$$F_k = c \tag{2.34c}$$

For radial flow, $w_f = 2\pi r$, hence equation (2.30) yields:

$$p_1^2 - p_2^2 = \frac{2\mu}{\gamma_o k} \frac{\ln(r_2/r_1)}{2\pi e} Q_m + \frac{2c\gamma^{n-2}k^{(n-3)/2}}{\gamma_o} \frac{1}{(2\pi e)^n} \frac{r_1^{1-n} - r_2^{1-n}}{n-1} Q_m^n \tag{2.35a}$$

or

$$p_1^2 - p_2^2 = a_r Q_m + c b_r Q_m^n \tag{2.35b}$$

where a_r and b_r are constants related to the radial flow geometry and fluid properties.

Defining a Reynold's number for radial flow is difficult since γv is no longer constant due to divergence of the flow paths. For the case of $n = 2$ we define R_k as for the linear case and recognize that R_k now contains a characteristic radius $r^* = (r_1 r_2 \ln(r_2/r_1))/(r_2 - r_1)$ such that $r_2 > r^* > r_1$, hence:

$$R_k = \frac{\gamma v k^{1/2}}{\mu} = \frac{k^{1/2}}{\mu} \quad \frac{r_2 - r_1}{2\pi e r_1 r_2 \ln(r_2/r_1)} \quad Q_m = \frac{b_r}{a_r} Q_m \qquad (2.36)$$

and

$$F_k = - \frac{k^{1/2}}{\gamma} \quad \frac{1}{v^2} \frac{dp}{dr} \quad = \frac{1}{b_r} \quad \frac{p_1^2 - p_2^2}{Q_m^2} \qquad (2.37)$$

Previous experimenters have defined γv as $Q_m/2\,er^*$ where r^* is a characteristic radius ranging from simply $r^* = r_1$ (Iwai, 1976) to r^* = the largest radius at which turbulent flow occurs (Baker, 1955). Both of these definitions are arbitrary and in the latter case difficult to define in the absence of an abrupt linear to turbulent flow transition.

With these definitions of R_k and F_k, equations (2.35) may be described by equations (2.34).

As a consequence of the variation of v_m over the flow path, the non-linear inertial losses are largest near the inner radius, and hence the pressure distribution is shifted towards a steeper pressure gradient near the inner radius.

2.3 Factors Influencing Gas Flow Rates

Several factors can influence measured flow rates, particularly under field testing conditions. In this section certain factors are considered and quantified including: velocity limitations, elliptical injection boundaries, intersecting secondary fractures, and effective radius.

2.3.1 Limitations on the Cubic Law for Gas Flow

At the beginning of this chapter the cubic law was found to be theoretically valid for fracture flow of a compressible fluid of constant viscosity, provided the flow velocity was sufficiently small. The assumption of constant viscosity is valid for nitrogen and air if the flow remains essentially isothermal.

To determine how small the velocity, v, must be in order that the ignored components of equations (2.2) are negligible, the velocity is computed using equations (2.4) and either (2.15) or (2.21).

For linear isothermal flow (m = 1):

$$v(x,y) = \frac{\alpha}{4\mu} \left(\frac{e^2}{4} - y^2\right) (\alpha x + \beta)^{-1/2}$$

and

$$\frac{\partial p}{\partial x} = \frac{\alpha}{2} (\alpha x + \beta)^{-1/2}$$

Hence the partial derivatives of v(x,y) are:

$$\frac{\partial v}{\partial x} = \frac{-\alpha^2}{8\mu} \left(\frac{e^2}{4} - y^2\right) (\alpha x + \beta)^{-3/2} \qquad (2.38a)$$

$$\frac{\partial^2 v}{\partial x^2} = \frac{3\alpha^3}{16\mu} \left(\frac{e^2}{4} - y^2\right) (\alpha x + \beta)^{-5/2} \qquad (2.38b)$$

$$\frac{\partial^2 v}{\partial y \partial x} = \frac{\alpha^2}{4\mu} (y)(\alpha x + \beta)^{-3/2} \qquad (2.38c)$$

Using equations (2.38), the ratio of the ignored forces in equations (2.2) to the pressure gradient as computed from the single term ($\mu \partial^2 v / \partial y^2$) are found to be:

Term Considered from Equations (2.2)		Ratio Formula	
$\gamma v \frac{\partial v}{\partial x}$	= inertial force	$\frac{-\gamma_o \alpha^2}{16\mu^2}(\frac{e^2}{4} - y^2)^2(\alpha x+\beta)^{-1}$	(2.39a)
$(K + \frac{4\mu}{3}) \frac{\partial^2 v}{\partial x^2}$	= ignored viscous forces in x-direction	$(K + \frac{4\mu}{3})\frac{3\alpha^2}{8\mu}(\frac{e^2}{4} - y^2)(\alpha x+\beta)^{-2}$	(2.39b)
$(K + \frac{\mu}{3}) \frac{\partial^2 v}{\partial y \partial x}$	= ignored viscous forces in y-direction	$(K + \frac{\mu}{3})\frac{\alpha}{2\mu}(y)(\alpha x+\beta)^{-1}$	(2.39c)

By inspection, the ratio equations will be maximum when $(\alpha x+\beta) = P^2(x)$ is smallest, that is at the exit point, $x = L$ assuming $P(0) > P(L)$, where $P^2(L) = P_2^2$. Equations (2.39a and b) will be maximized when $y = 0$. Intuitively this makes sense since the maximum velocity occurs midstream at the exit point. For viscous forces in the y-direction, equation (2.39c) will be maximum at the fracture boundaries ($y = e/2$, $-e/2$) where the rate of fluid dilation is greatest. Equations (2.26) are plotted for these maximums for the fracture aperture, $e = 100$ μm, and as a function of the factor $\alpha = \Delta P^2/L$ in Figure 2.5. While all of the ignored forces seem to be rather small, the inertial force is considerably larger than the others. Note that the ratio values expressed by Equations (2.39a and b) increase with the square of the aperture.

The inertial force may be expressed in terms of the fluid velocity by noting that equation (2.39a) may be written as $\gamma_o v^2$ or, for isothermal flow of an ideal gas, Mv^2/RT. Since γ_o is small for gases, the flow velocity can become rather large before inertial effects are significant. Nitrogen at room temperature can have a flow velocity of 30 m/s before inertial forces are 1% of the pressure gradient.

2.3.2 Elliptical Fracture Intercepts

The radial flow equations developed previously assume that the constant pressure boundaries are circular. Field borehole injection tests, however, often involve fractures which do not intersect the borehole axis perpendicularly resulting in an elliptical boundary. This problem has been considered by Wang et al. (1977), who indicated that the flow rate would be increased by the ratio of the elliptical perimeter to the circular circumference. A more exact solution was worked out by Bourke et al. (1980) using elliptical coordinates. He modified the radial flow rate equation (2.24) to the form:

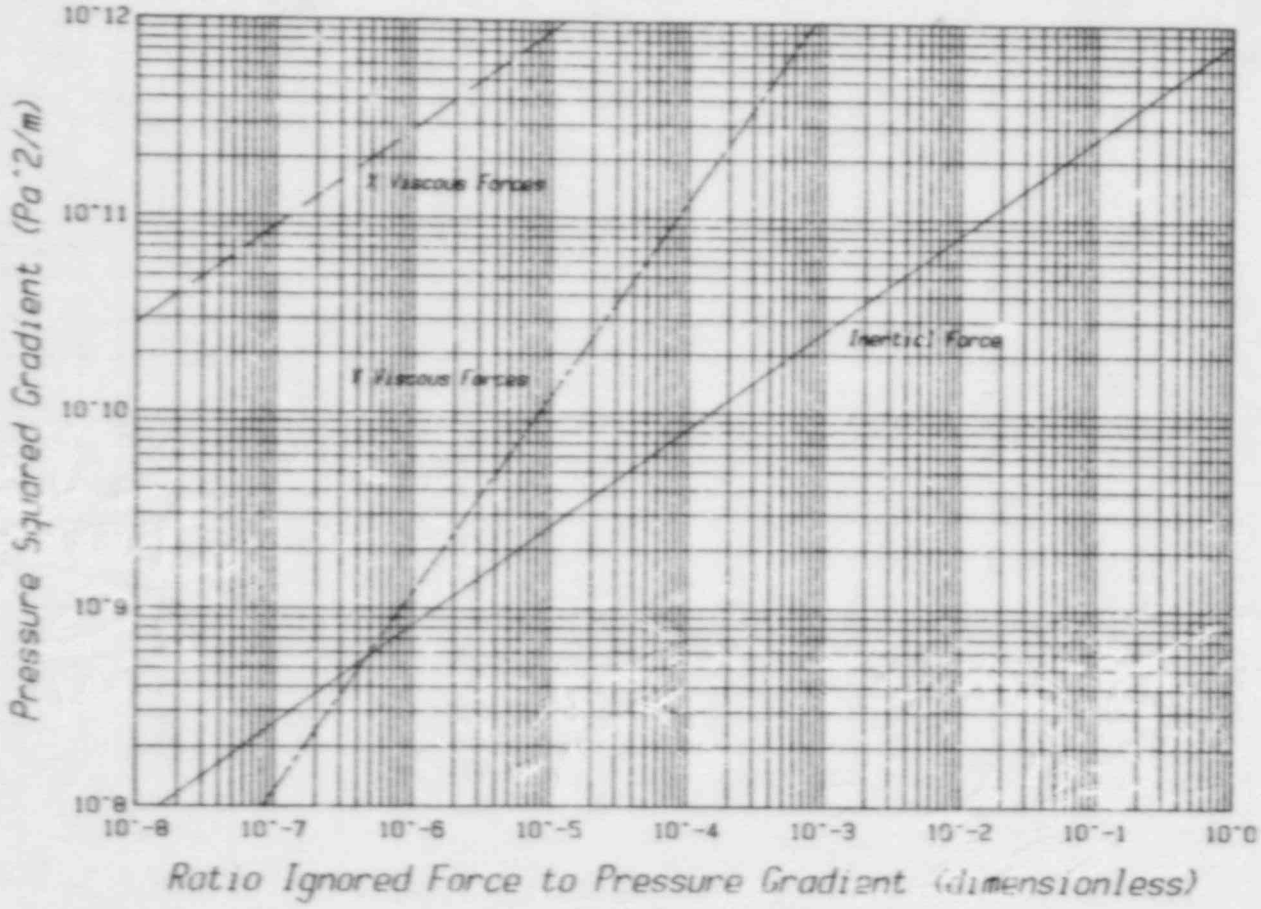

Figure 2.5. Ratio values versus pressure squared gradient for e = 100 μm.

$$Q_m = \frac{-\pi e^3 \gamma_o}{6(m+1)\mu} \frac{p_2^{m+1} - p_1^{m+1}}{\ln(r_2/r_1) + \ln \frac{2\cos\theta}{1+\cos\theta}} \qquad (2.40)$$

where θ = the angle between the normal to the fracture plane and the borehole axis.

This is equivalent to multiplying the borehole radius, r_1, by $(1 + \cos\theta)/2\cos\theta$. The ratio of Q_m (elliptical) to Q_m (radial) is given as a function of θ in Figure 2.6. From this figure it is seen that for deviations of less than 45° no major increase in flow rate is observed. As the angle increases beyond 45°, however, the flow rate increases rapidly, particularly for smaller ratios of r_2/r_1.

2.3.3 Intersecting Fractures

The flow equations developed in the previous section are based on the idealized case of a single fracture. Under actual field test conditions, secondary fractures often exist which intersect the tested fracture, causing branching of the flow and consequent distortion of the pressure distribution and measured flow rate for the tested fracture.

To quantify the influence of secondary intersecting fractures on observed radial flow rates from an injection borehole through a tested fracture, a study was conducted using a numerical approach. Gas flow was modeled using a modified version of the Prickett-Lonnquist finite difference model (Prickett and Lonnquist, 1971). A variable spacing rectangular model mesh was used to determine steady state pressure distribution and boundary fluxes within the principal fracture plane. As an approximation to constant pressure boundaries at infinity, constant pressure boundaries were placed at a distance of 100 borehole radii.

The influence of a single intersecting fracture was effected by withdrawing flows along the line (or nodal column) of fracture intersection. These flows were drawn off as a proportion of the inflow through the principal fracture directly upstream from the fracture intersection. Referring to Figure 2.7, conservation of mass requires:

$$Q_i = Q_1 + 2Q_2 \qquad (2.41)$$

where Q_i = upstream inflow along the principal fracture (nodal inflow), Q_1 = downstream outflow along the principal fracture (nodal outflow), and Q_2 = downstream outflow along one branch of the secondary fracture (nodal flow withdrawal).

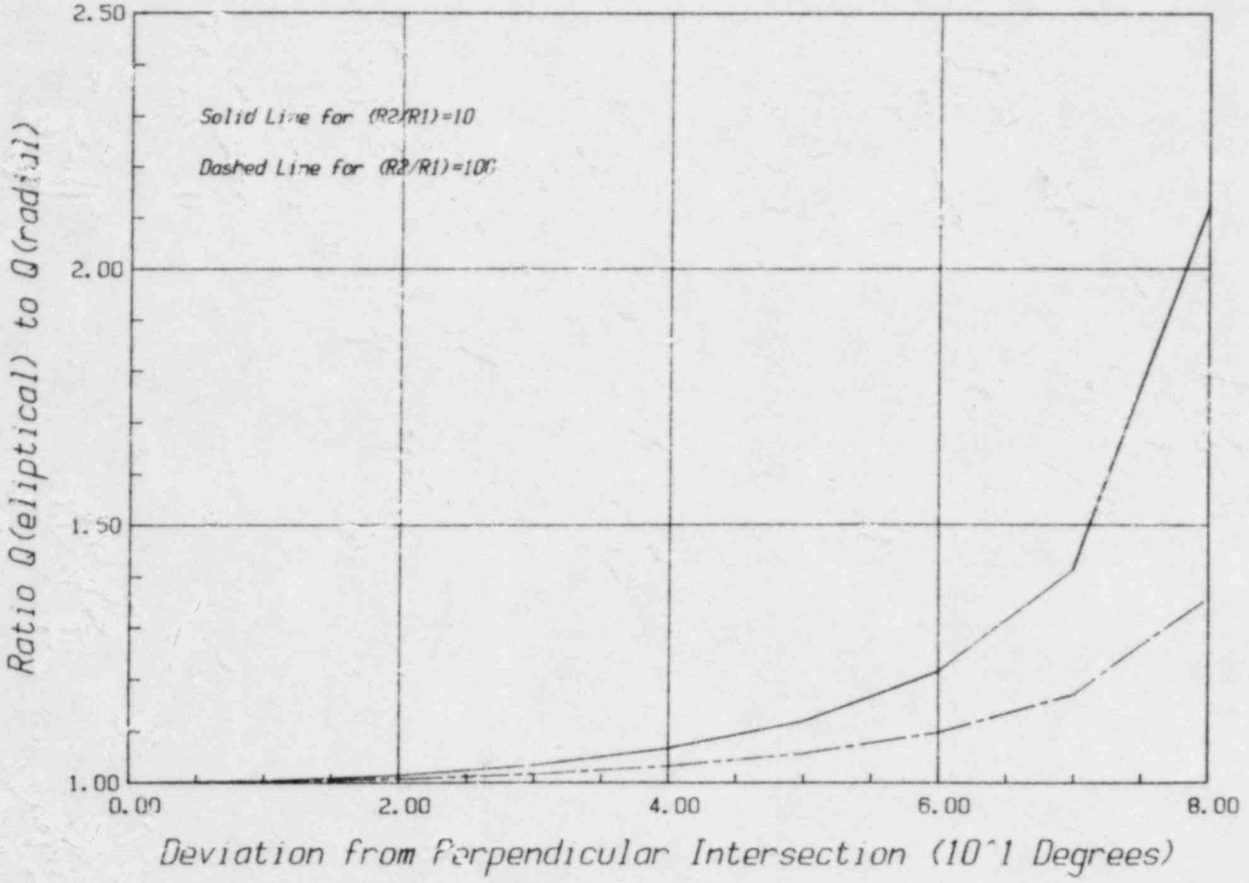

Figure 2.6. Effect of deviation angle on radial flow rate.

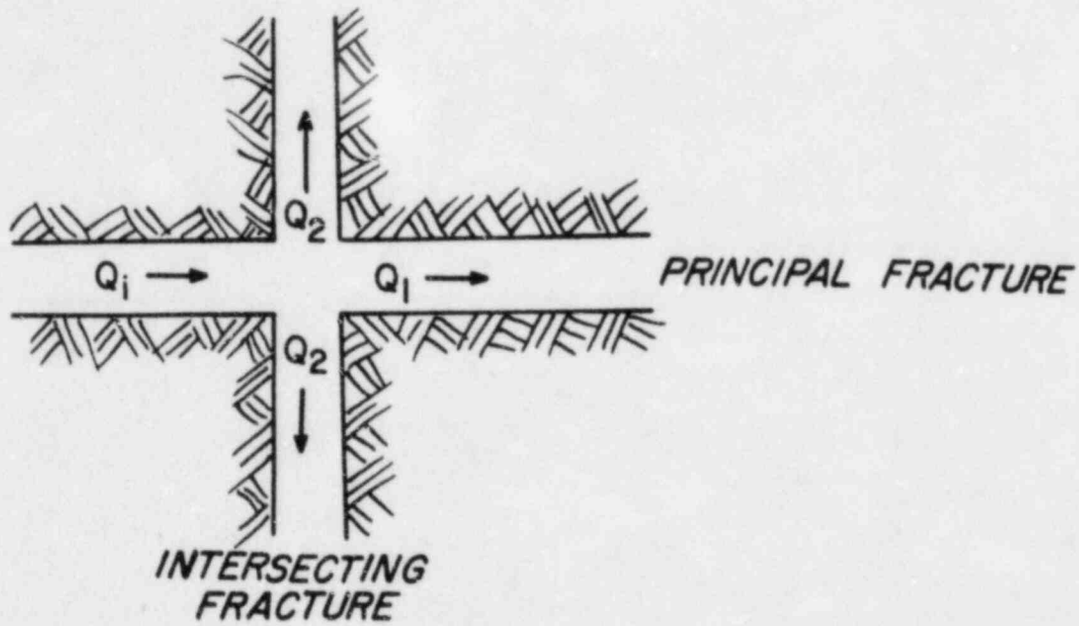

Figure 2.7. Definition of fracture inflows and outflows.

At steady state the downstream pressure gradients within both the secondary and principal fractures will be identical provided that the boundary conditions for both fractures are identical. This will be approximately true if both fractures have constant pressure boundaries at large distances from the line of intersection, where the boundary conditions are certainly identical. In this case the ratio of Q_1 to Q_2 is:

$$Q_1/Q_2 = e_1^3/e_2^3 \tag{2.42}$$

Hence, combining equations (2.41) and (2.42) we find:

$$Q_2 = \frac{Q_i}{2+(e_1/e_2)^3} \tag{2.43}$$

In deriving equation (2.43), inertial factors have been ignored. This is a reasonable assumption in light of experimental studies (Wilson and Witherspoon, 1970) on the effect of fracture intersections.

The results of the numerical study are summarized in Figure 2.8. These data indicate that intersecting secondary fractures are of minor importance when the aperture of the intersecting fracture is less than 50% that of the principal fracture. However, the influence of a secondary fracture increases considerably as its aperture increases above that of the principal fracture, rapidly approaching the flow level for a constant ambient pressure boundary along the line of fracture intersection. It is noted that the transition zone in terms of the ratio e_1/e_2 is abrupt as would be expected from examination of equation (2.43). The influence of secondary fractures also diminishes with distance from the injection well although even at radial distances of 20 well radii increases in flow rate up to 30% are noted. A complete summary of the data obtained is presented in Appendix A.

2.3.4 Effective Radius

Estimation of effective radius is a familiar problem in field measurements of conductivity. Effective radius is used here to denote the minimum radius at which the in situ or ambient pressure head is undisturbed. For single hole tests an effective radius must be estimated to reduce equation (2.24) to a single unknown, e. The dependence of the flow rate on the ratio r_2/r_1, where r_2 equals the effective radius is shown in Figure 2.9. As the ratio r_2/r_1 increases this dependence is shown to decrease.

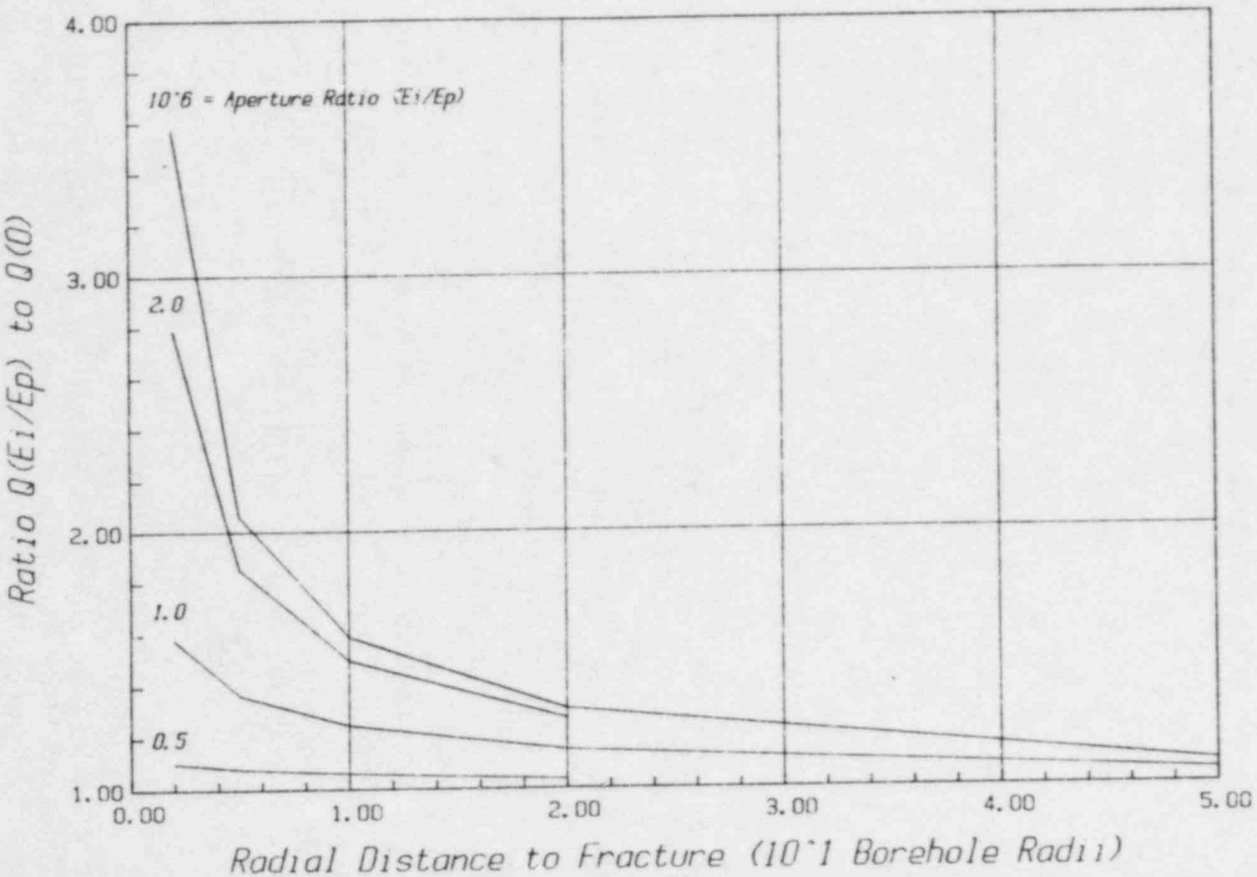

Figure 2.8. Effect of intersecting fracture on radial flow rate.

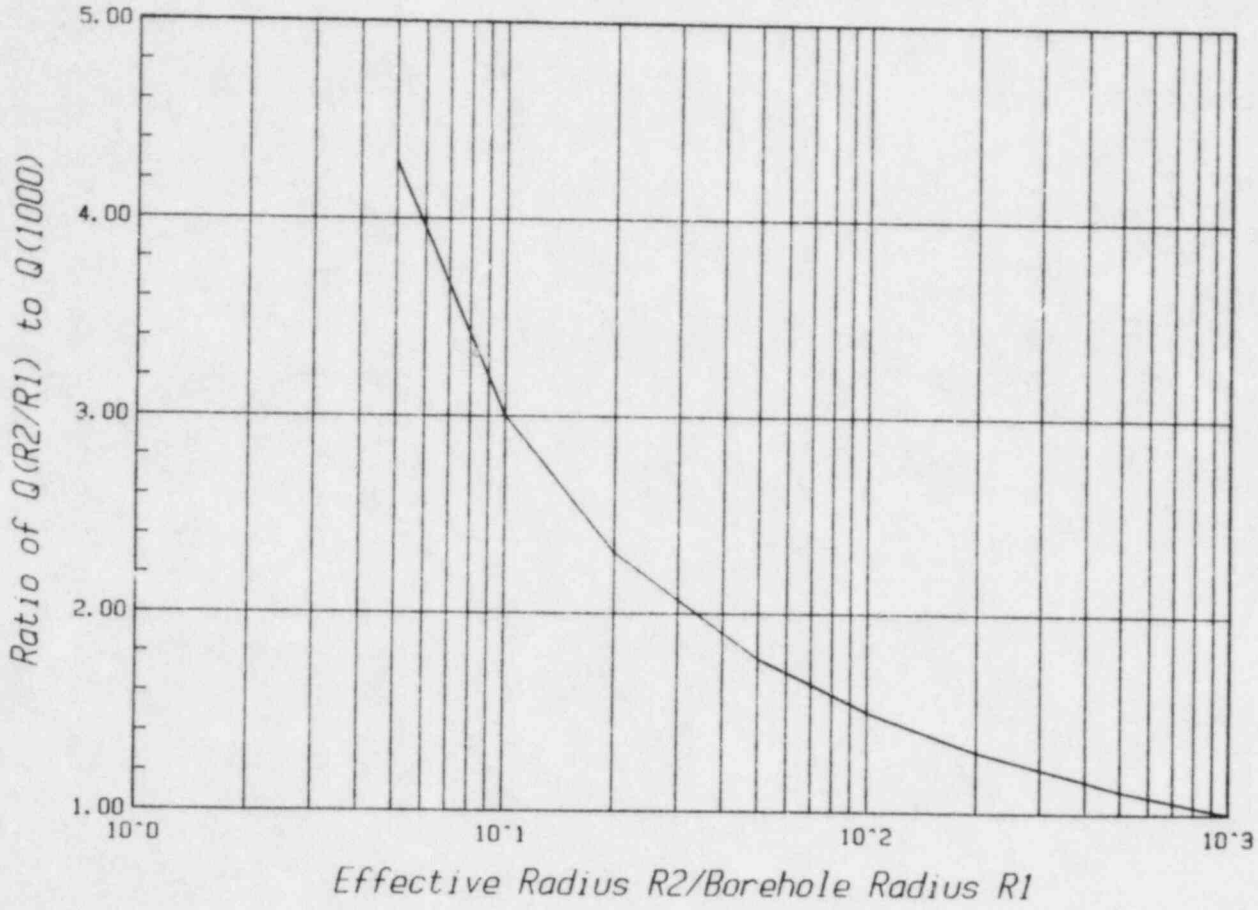

Figure 2.9. Dependence of flow rate on effective radius.

For gas flow through a single infinite fracture, the effective radius will rapidly increase with time owing to the low viscosity and density of gas. In reality, however, intersections with other fractures greatly reduces the effective radius by diverting flow and creating constant pressure boundaries as discussed in the previous section. For this reason it is suggested that one half the average spacing between intersecting fractures be used to estimate an effective radius for gas flow tests in fractured rock using a single injection hole. Where more accurate estimates of fracture conductivity are required, parallel observation holes should be drilled to provide better estimates of effective radius.

2.4 Relationship Between Average and Deformation Apertures

In all previous laboratory studies of fracture flow, measured aperture deformation has been assumed to equal actual changes in average aperture. Strictly speaking, this may not always be true.

The arithmetic average aperture of a fracture may be determined directly if its volume and area, or planar extent, are known since:

$$\bar{e} = \frac{V_f}{A_f} \tag{2.44}$$

where $\bar{e}$ = arithmetic average aperture, V_f = fracture volume, and A_f = fracture area (planar extent).

To determine the relationship between $\Delta\bar{e}$ and Δe_d, the aperture deformation, three fracture deformation models are considered (Figure 2.10).

In the first model, fracture deformation is limited to deformation of points of contact, hence:

$$\Delta V_f = (A_f - A_c)\Delta e_d \tag{2.45}$$

where A_c = the fracture contact area.

Hence,

$$\frac{\Delta\bar{e}}{\Delta e_d} = \frac{A_f - A_c}{A_f} = 1 - \frac{A_f}{A_c} \tag{2.46}$$

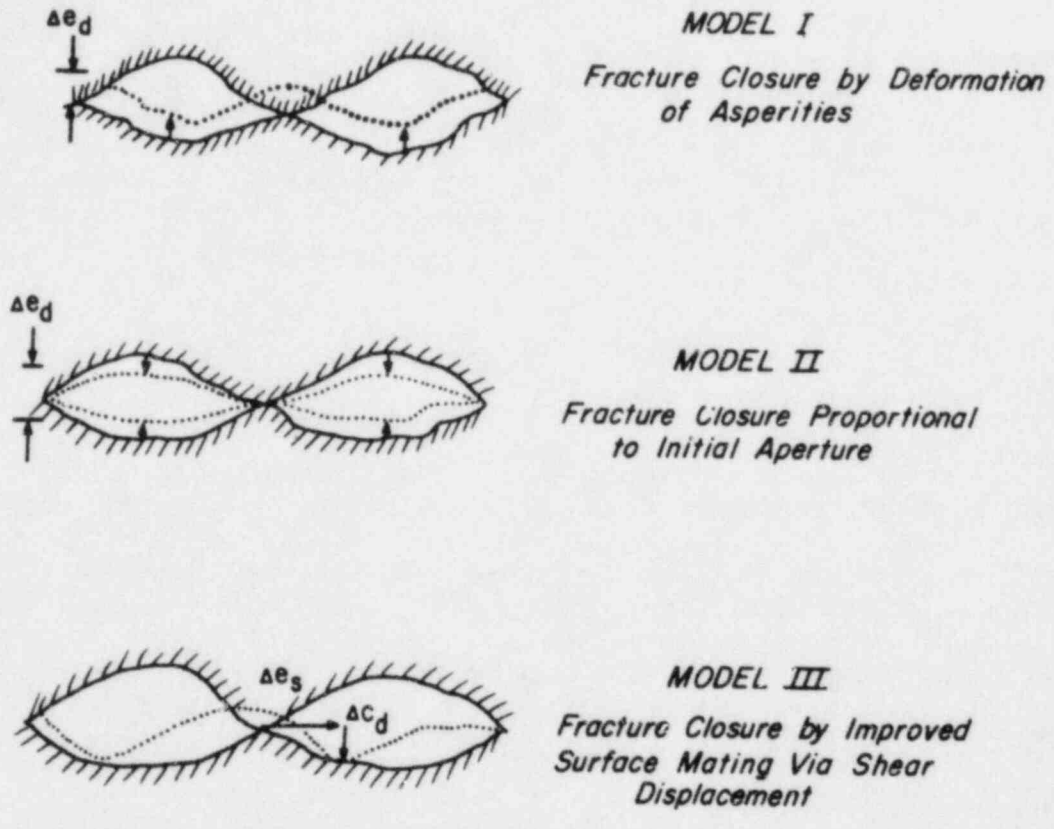

Figure 2.10. Three fracture deformation models.

or the arithmetic average aperture changes less than the deformation aperture, particularly when contact area is large.

In the second model, fracture contact area remains constant while deformation of the fracture walls creates a closure assumed to be proportional to the initial aperture. For this case, where at any point i on the fracture surface, $e_i(\text{new}) = ce_i(\text{initial})$, and c = a constant at a given applied stress:

$$\Delta\bar{e} = (1-c)\,\bar{e}(\text{initial}) \tag{2.47}$$

Although an exact relationship between Δe_d and fracture closure is not attainable in this particular case, it is reasonable to assume that $\Delta e_d = \Delta e_{max}$, or:

$$\Delta e_d = (1-c)\,e_{max}(\text{initial}) \tag{2.48}$$

Since $e_{max} > e$, $\Delta\bar{e}/\Delta e_d \leq 1$, as for the first model. However, as where the first model predicts that $\Delta\bar{e}/\Delta e_d \to 0$ with increasing normal stress, the second model predicts that $\Delta\bar{e}/\Delta e_d \to 1$ under the same conditions.

A third and final model is that of normal and shear displacement to accommodate mating of the fracture surface without fracture deformation. To analyze this model, it is easier to consider the shear and normal displacements separately. Under pure shear displacement, no fracture volume change occurs and hence $\Delta e = \Delta e_d = 0$. Under subsequent normal displacement up to the point where fracture contact is reestablished, $\Delta\bar{e} = \Delta e_d$.

3. LABORATORY MEASUREMENTS

This chapter presents the laboratory measurements of fracture conductivity, volume, and deformation using a large rock sample containing a single natural fracture. Included in this chapter are all aspects of the laboratory studies with separate sections devoted to the experimental approach or method and the experimental results. Actual discussion of the experimental results is deferred to the following section.

3.1 Experimental Approach

This section deals with all details of the testing equipment and methods. Specifically included are discussions of sample preparation, experimental apparatus, instrument accuracy, and testing procedures.

3.1.1 Sample Preparation

A large rock sample containing a single natural fracture was cut from a large rock block obtained from a surface outcrop. This method provided the easiest and quickest means of obtaining a representative fracture sample by eliminating the need for elaborate in situ cutting techniques.

The sample used for the testing discussed herein was acquired from a surface exposure near Washington Camp, Arizona, in the southern Patagonia Mountains. The bedrock here is a portion of a large granodiorite batholith, and the fracture contained within the sample is associated with a pervasive set of subhorizontal exfoliation joints. The joint surface (Figure 3.1) is coated with iron oxide staining and slight amounts of pyrite. Discoloration of the rock near the joint surface indicates slight weathering to a depth of a few centimeters. While the surface of the joint is quite rough, the overall surface is very planar and apparently well mated.

Since the natural fracture contained in the first sample was completely opened, the sample halves were separated and the exposed fracture surfaces protected during removal of the sample from the field. Upon arrival at the laboratory, the sample halves were remated with a protective rubber matting placed between the surfaces. A 1-inch diameter hole was then drilled perpendicular to and through the center of the fracture surface and the sample halves were bolted together to permit cutting of the sample. Cutting, or trimming of, the sample edges to form a rectangular parallelpiped was done with a 36-inch diameter circular diamond saw. This was followed by lapping of the sample sides to achieve a true rectangular shape, as the saw cut surfaces were not perfectly parallel and perpendicular to each other. The sample was then washed thoroughly, including the fracture surface, to remove all rock flour. The final dimensions of the prepared sample are 25.4 cm wide by 28.2 cm long by 28.0 cm high with the fracture surface inclined slightly at 3° to the horizontal.

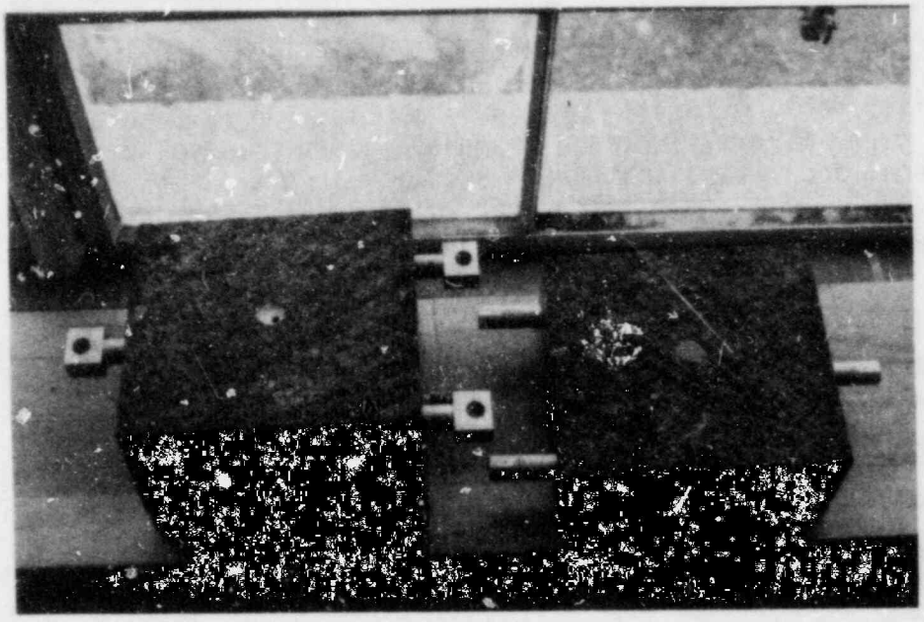

Figure 3.1. Photograph of fracture surface.

3.1.2 Measurement of Sample Stress-Strain Behavior

Knowledge of the stress-strain behavior of the rock samples tested is required to interpret measurements of fracture deformation, which due to practical limitations must include some intact rock deformation. To this end samples of granodiorite were loaded uniaxially to determine their stress-strain relations.

Two cores of granodiorite, 2 inches in diameter by 4 inches in length, were prepared and tested using bonded resistance strain gages with a 1/2-inch gage length. These samples were cored from a large block taken from the same outcrop as the fractured sample, with the axis of the core oriented so as to correspond with the direction of loading of the fractured sample. The first sample was initially load cycled three times; however, problems with the test instrumentation produced unsatisfactory results. The sample was then tested again by load cycling twice to a maximum applied stress of about 20 MPa. Due to the initial difficulties incurred during testing of the first sample, no information was obtained on strain hardening effects. Therefore, a second sample was load cycled three times to 20 MPa. While the second sample exhibited significant strain hardening following the initial load cycle, repeatable stress-strain behavior was observed for all subsequent load cycles. Good agreement was also found between the observed strains of the two separate samples with the maximum observed differences less than 5%. Results of these tests are presented in Table 3.1 and Figures 3.2 and 3.3. The measured strains for the 4th and 5th load cycles of the first sample and the 2nd and 3rd load cycles of the second sample were averaged to obtain a representative rock strain curve for the fractured granodiorite sample. This representative curve was subsequently used to reduce all fracture deformation data.

3.1.3 Experimental Apparatus

3.1.3.1 General Description. The experimental apparatus constructed to perform the fracture volume and flow measurements consists of six basic components, namely a pressurized gas supply, a flow regulating and monitoring manifold, a sample girdle and flow control system, an air pycnometer and pressure monitoring manifold, a sample loading frame, and a data monitoring and recording system.

The pressurized gas supply consists of a compressed nitrogen tank equipped with a 0-1.4 MPa pressure regulator and gage. This provides a simple constant pressure source which may be varied as a coarse flow rate adjustment. The supply is connected to the flow regulating and monitoring manifold with flexible hosing equipped with quick-connect fittings.

The flow regulating and monitoring manifold is shown schematically in Figure 3.4. This simple manifold filters incoming air with a 0.6 micron

Table 3.1. Stress-Strain Measurements for Intact Granodiorite Samples

Uniaxial Stress (MPa)	Axial Strain (microstrain) Sample No. 1		Sample No. 2		
	#4	#5	#1	#2	#3
0	0	0	0	0	0
2.19	42	46	31	39	39
4.39	91	94	85	90	91
6.59	140	144	139	142	142
8.78	185	188	191	191	190
10.98	230	234	239	236	236
13.17	274	277	295	287	288
15.37	316	318	346	333	335
17.56	363	365	392	373	374
19.76	405	407	447	425	423
17.56	371	375	412	387	385
15.37	334	337	375	351	350
13.17	295	298	333	311	309
10.98	253	253	290	264	263
8.78	211	213	246	222	219
6.59	170	170	200	181	171
4.39	117	120	150	122	120
2.19	68	65	96	64	60
0	10	5	32	5	4

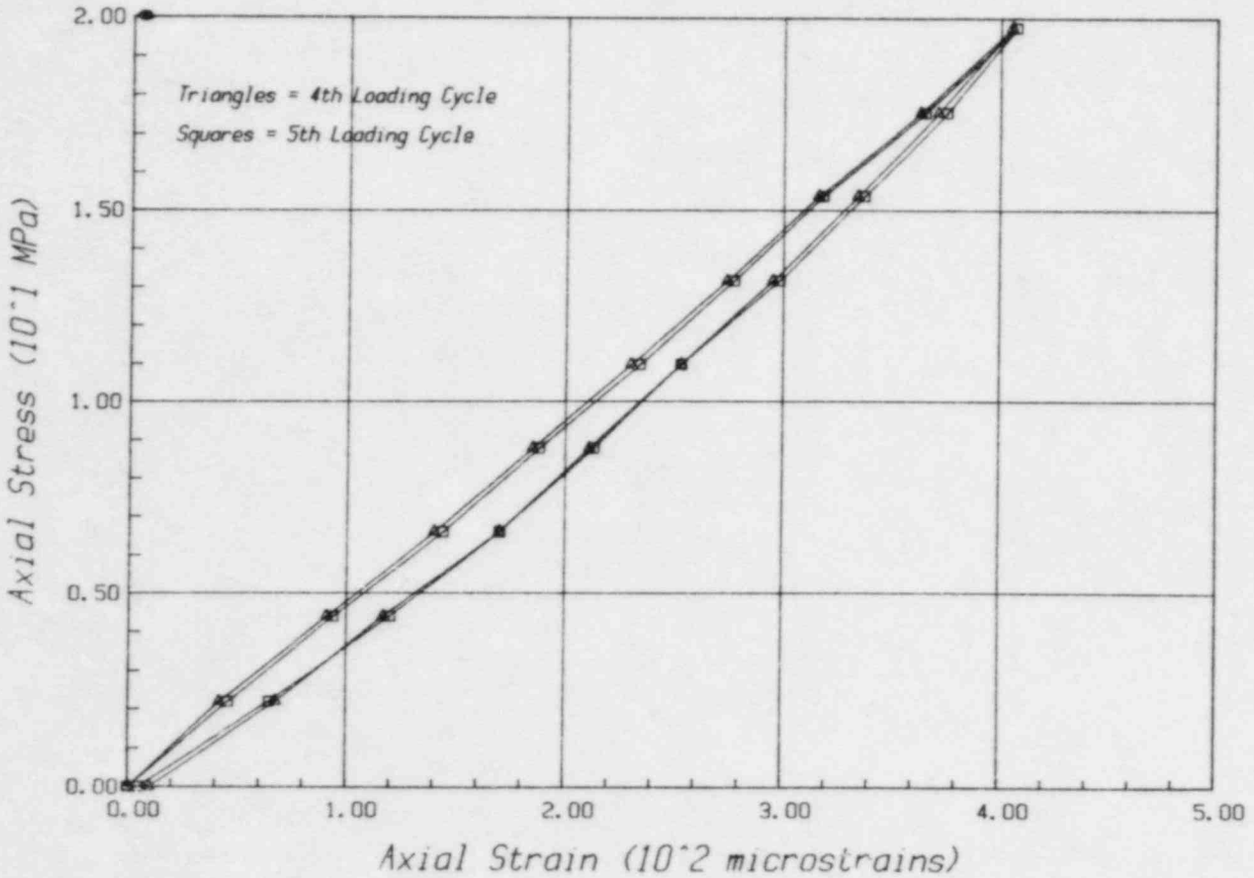

Figure 3.2. Stress-strain curve for sample no. 1, 4th and 5th load cycles.

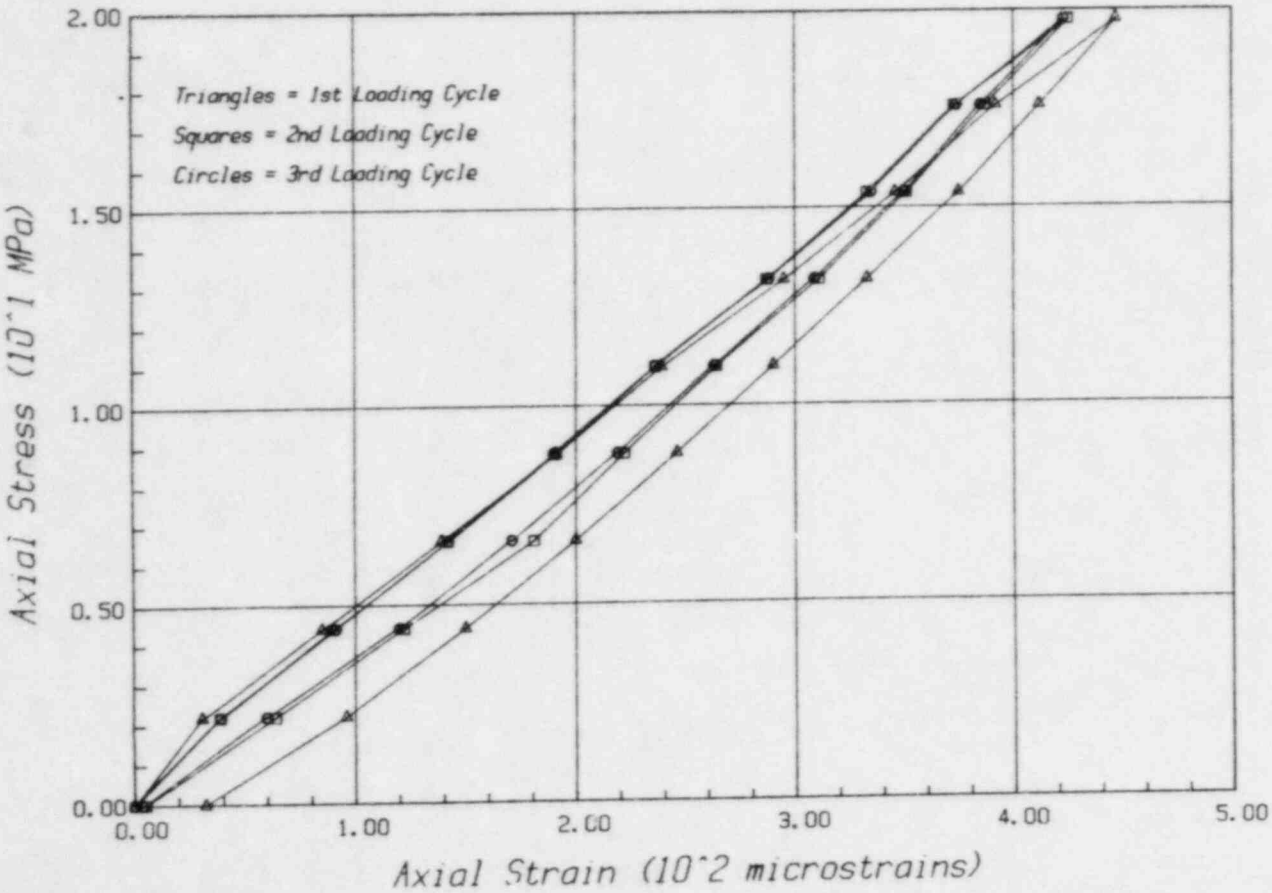

Figure 3.3. Stress-strain curves for sample no. 2, 1st, 2nd, and 3rd load cycles.

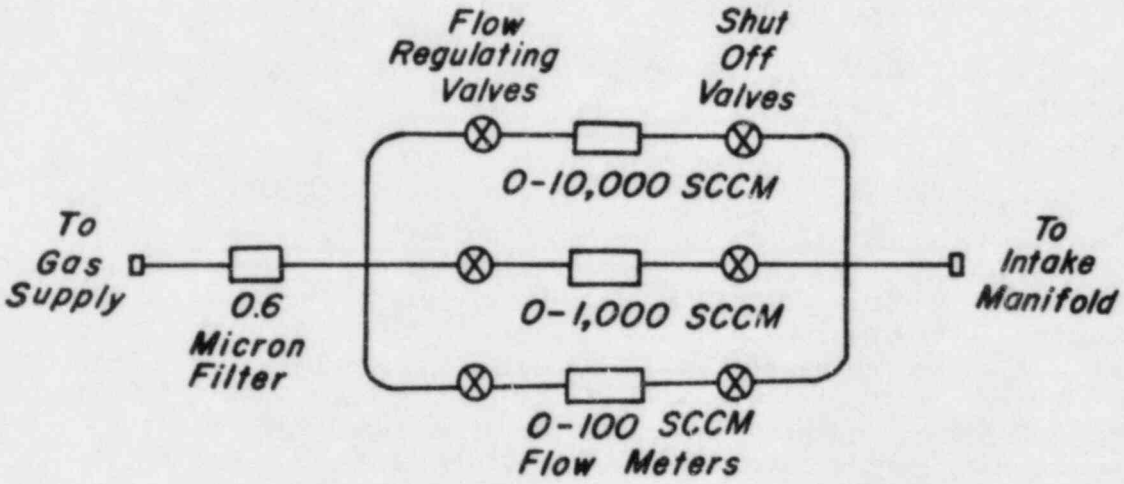

Figure 3.4. Schematic of flow regulating and monitoring manifold.

filter and directs output through one of three mass flow transducers, each designed for a different flow measurement range. Each flow transducer measures mass flow directly and, hence, is essentially insensitive to thermal or pressure fluctuations of the flow, eliminating the need for any pressure or temperature measurement within the manifold. Further details of the flowmeters are presented later in this section. Immediately upstream of each flowmeter is a flow regulating valve and downstream a positive shut-off value. The regulating valves are provided to vary flow rate precisely and enable a determination of the injection pressure versus flow rate curve. Flow rate is generally easier to regulate for this purpose than injection pressure. The shut-off valves are provided as a guard against leakage through unused branches of the manifold. Connection of the flow regulating manifold to the sample girdle and flow control system is made via flexible hosing equipped with quick-connect fittings.

The sample girdle and flow control system is designed to create the desired boundary conditions for both fracture volume and flow measurements.

For a rectangular fracture, the girdle assembly consists of an intake manifold, an exhaust manifold, and two side barriers as shown in Figure 3.5. In addition, two thin barrier strips can be attached to the facing of the intake and exhaust manifold to completely seal the outer fracture boundary. While the sample girdle is held in place by bolts connecting opposing members, an airtight seal is obtained by a 1/8-inch rubber gasket affixed to the inner edges of the girdle and sealed to the sample sides with RTV silicone rubber. The girdle assembly thus provides for three boundary conditions: all four fracture boundaries sealed; two opposing fracture boundaries sealed with the remaining two boundaries opened only to the intake and exhaust manifolds, respectively; and all four fracture boundaries open to the atmosphere. These conditions are imposed for air pycnometer volume measurements; linear flow and air pycnometer volume measurements; and radial flow measurements, respectively. The intake manifold is fitted with two connections, a valved air intake with quick-connect fitting for attachment to the flow regulating manifold, and an unvalved port to the air pycnometer and pressure monitoring manifold. This second connection allows for both air pycnometer and injection pressure measurements during linear flow testing. The exhaust manifold is equipped with a single port which can be plugged. Both manifolds are equipped with type T thermocouple sensors for monitoring temperature differentials between intake and exhaust gases.

The fractured sample block contains a single 25-mm center hole, perpendicular to the fracture plane for fracture volume (air pycnometer) and radial flow tests. This center hole, which is largely plugged with epoxy filler, contains a narrow 1/4-inch drilled hole connecting the fracture opening with a lower plate as shown in Figure 3.6. Epoxyed to

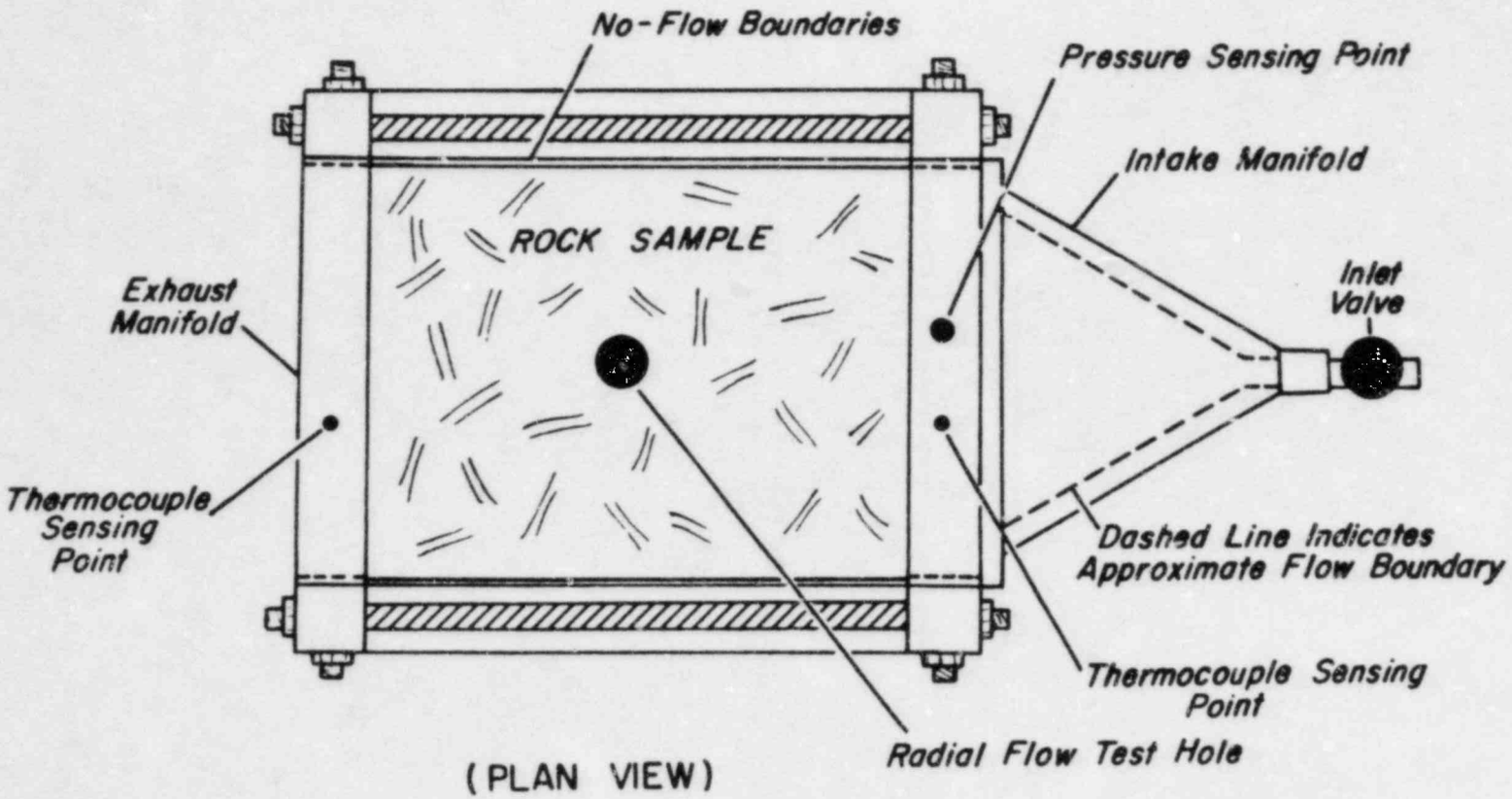

Figure 3.5. Detail of sample boundary girdle.

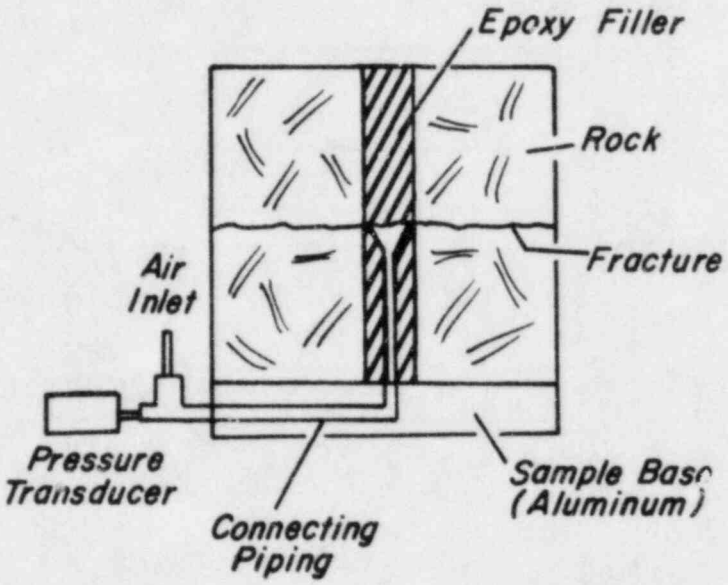

Figure 3.6. Detail of center hole piping.

the sample base to prevent leakage along the sample plate interface, this lower plate contains a second horizontal hole which connects the vertical hole to an outside port along the plate's edge. This piping system is connected in turn to the air pycnometer and pressure monitoring manifold. Additionally, a quick-connect fitting for connection to the flow regulating and monitoring manifold is provided.

The air pycnometer and pressure mounting manifold (Figure 3.7) provides the means for directly measuring the fracture volume and flow injection pressures. This simple manifold consists of a pressure transducer, a reference volume cylinder, and a few associated valves. The reference volume cylinder provides a known volume by which successively larger volumes, including the remainder of the pycnometer manifold, may be measured through a process of pressurization and equilibration. This procedure is discussed in greater detail later in this section. The cross valve connecting the reference volume to the remainder of the manifold permits isolation of this reference volume. A second positive shut-off valve is used to isolate the entire pycnometer manifold, which serves as a reference volume during actual fracture volume measurements. For the testing of rectangular fracture samples, a three-way switching valve is used to connect the pycnometer manifold to either the intake manifold or the center hole piping system.

The sample loading frame (Figure 3.8) is designed for uniaxial loading of large fractured rock samples and has a maximum design capacity of 270,000 kg, or a safe load capacity of about 180,000 kg. Samples up to 45 cm on a side can be accommodated as dictated by the column spacing, while the upper plates can be raised or lowered to accommodate total sample heights of 29 to 34 cm. Loads are applied with stainless steel hydraulic flatjacks using a hand pump with a 20 MPa maximum pressure capability. The maximum permissible load for the sample tested is about 20 MPa.

The data monitoring system (Figure 3.9) used to read and convert transducer voltages is an HP3497 data logger controlled by an HP85 minicomputer. This system can be programmed to read voltages with either a manual or internally timed trigger. Raw voltages and converted readings are recorded on 11-cm paper tape and magnetic tape cartridges.

3.1.3.2 Air Pycnometer. The air pycnometer provides a direct and accurate means of measuring unknown volumes and is used in these tests to measure fracture volumes. As such it provides an independent check on hydraulically measured apertures, which previously had not been performed.

Treating nitrogen as an ideal gas under isothermal conditions, the product PV, where P = the hydrostatic absolute pressure and V = the volume of the system under consideration, is a constant. To apply this principle to volume measurement, a system of known volume and initial

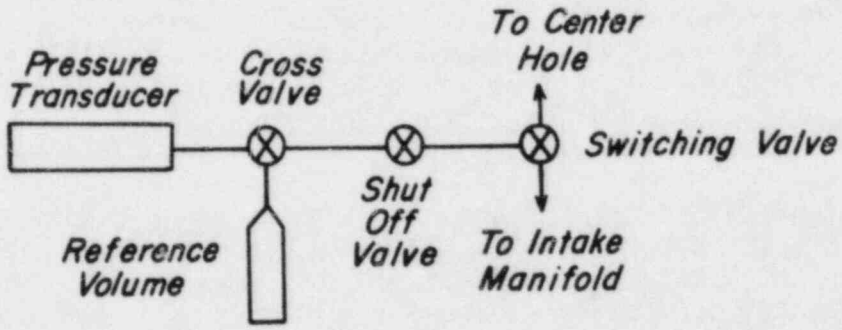

Figure 3.7. Schematic of air pycnometer and pressure monitoring manifold.

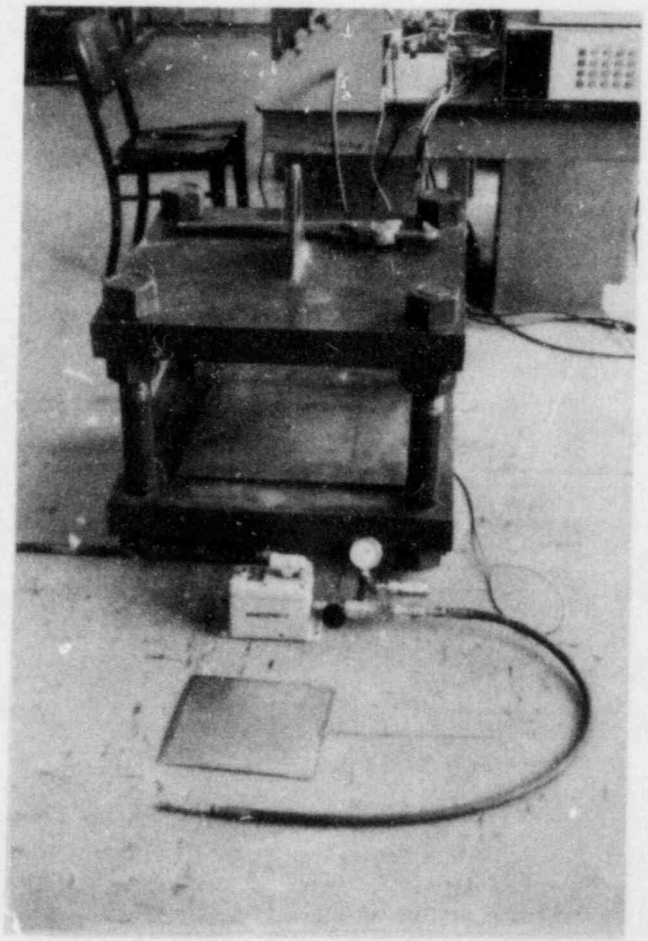

Figure 3.8. Photograph of sample loading frame.

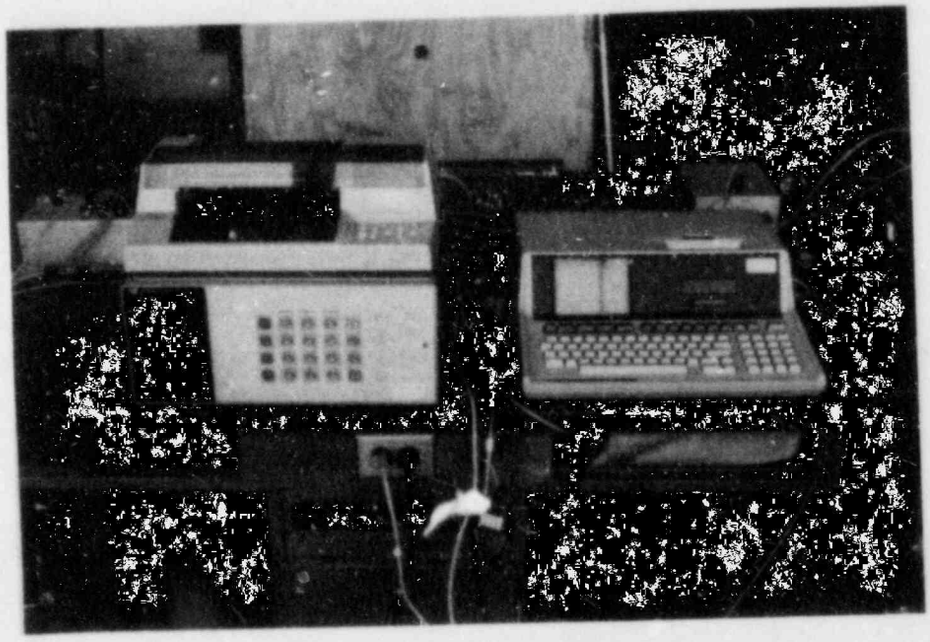

Figure 3.9. Photograph of data monitoring system.

pressure is connected to a system of unknown volume and known initial pressure (Figure 3.10). Measurement of the new equilibrium pressure of the combined system can then be utilized to determine the second system volume.

Analytically we have:

$$P_1V_1 = N_1RT \tag{3.1}$$

$$P_2V_2 = N_2RT \tag{3.2}$$

$$P_3(V_1+V_2) = (N_1+N_2)RT \tag{3.3}$$

Combination of equations (3.1), (3.2), and (3.3) yields:

$$\frac{(P_1-P_3)}{(P_3-P_2)} V_1 = V_2 \tag{3.4}$$

Hence the simple relationship expressed by equation (3.4) can be used to determine the unknown volume V_2. In these experiments, V_1 is initially the volume of the reference cylinder, whose volume is measured directly using distilled water and a balance. The reference cylinder is then pressurized and equilibrated to determine the volume of the remainder of the pycnometer manifold. The combined volume of the pycnometer manifold then becomes the new known volume V_1. The unknown measured volume V_2 then becomes the combined volume of the sample fracture and any connecting volume between the pycnometer manifold and the sample fracture. This latter volume can be measured separately, and since it does not vary during changes in the fracture volume, it may be subtracted from the measured volume V_2 to determine the true fracture volume.

3.1.3.3 Flow Measurement. Air flow measurements are made with Teledyne Hastings ST series mass flowmeters. These flowmeters utilize a heated conduit and measure heat transfer from the conduit to the gas flowing through the conduit, which is a function only of the mass flow rate and specific heat capacity of the gas. Hence the flowmeter calibration is relatively independent of temperature and pressure fluctuations within the recommended operating ranges of 0°-50°C and 0-1.7 MPa. Long-term drift measurements performed prior to testing suggested about a 1% of full scale zero drift due to daily temperature variation. Three

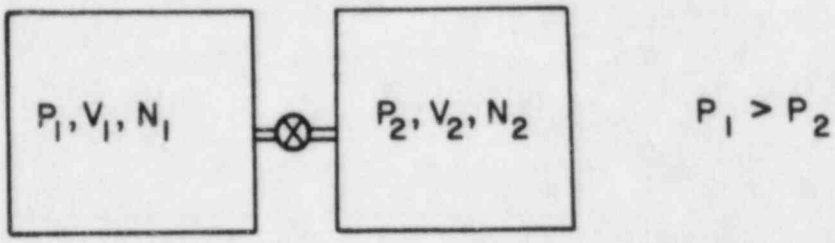

After connecting systems: P_3, V_3, N_3 *for combined system*

where: $P_1 > P_3 > P_2$

$$V_3 = V_1 + V_2$$

$$N_3 = N_1 + N_2$$

Figure 3.10. Air pycnometer diagram.

different flowmeters, with ranges of 0-0.1, 0-1.0, and 0-10.0 standard liters per minute, are used in these tests. As all three flowmeters are factory calibrated, accuracy of the flowmeters is uncertain although manufacturer's data indicate that nonlinearity is less than ±2% of the full scale reading and typically ±1% of the full scale reading.

3.1.3.4 Pressure Measurement. Presure measurements are made with Ametek 57M series pressure transducers. The sensing element for these transducers is a piezoresistive silicon chip with an integral Wheatstone bridge circuit and temperature compensation over the range of 0°-55°C. Long-term drift measurements indicate a zero drift of about 1% of full scale due to daily temperature variation. Manufacturer's data reports a transducer accuracy of ±1% full scale, including linearity, repeatability, and hysteresis. Three pressure gages were used in these tests, 0-200 kPa (0-30 psig), and 0-1330 kPa (0-200 psig) transducers for the air flow measurements and a 0-28 MPa (0-4000 psig) transducer for the hydraulic flatjack system. The 0-200 kPa and 0-1330 kPa transducers were calibrated against a standard 0-670 kPa (0-100 psia) transducer with an NBS traceable calibration, and an accuracy of better than 0.7 kPa (0.1 psi). Indicated agreement between both calibrated gages and the standard was better than 0.7 kPa (0.1 psi). The 0-28 MPa transducer was calibrated against a second standard (0-28 MPa Heise gage) with an NBS traceable calibration. Indicated agreement between the calibrated transducer and standard was better than 0.03 MPa (5 psi).

3.1.3.5 Displacement Measurement. Displacement measurements of fracture deformation were made with Trans Tek Series 240 direct current differential transformers (DCDTs) with a measurement range of ±0.64 cm (0.25 inches) and a linearity of ±0.5% full scale (50 microns or .002 in.) according to manufacturer's specifications. Long-term drift measurements (Figure 3.11) with the transducers mounted in place on the unloaded sample indicated a zero drift of about 25 microns due to daily thermal variation. The DCDTs were calibrated using a micrometer with a precision of 1 micron and a specially designed calibration jig. Indicated accuracy of the DCDTs is better than 20 microns over a 10 mm-range including linearity, hysteresis, and repeatability. As actual relative measurements are over a far smaller range, about 1 mm, considerably greater accuracy is expected.

3.1.4 Test Procedures

The test procedure can be broken down into three consecutive test series: measurement of fracture deformation versus volume, measurement of fracture deformation and volume versus linear conductivity, and measurement of fracture deformation versus radial conductivity.

In the first test series, the sample girdle was placed as shown in Figure 3.12a, and the sample was load cycled twice to 20 MPa (3000 psi). Fracture volume and deformation were measured at successive stress

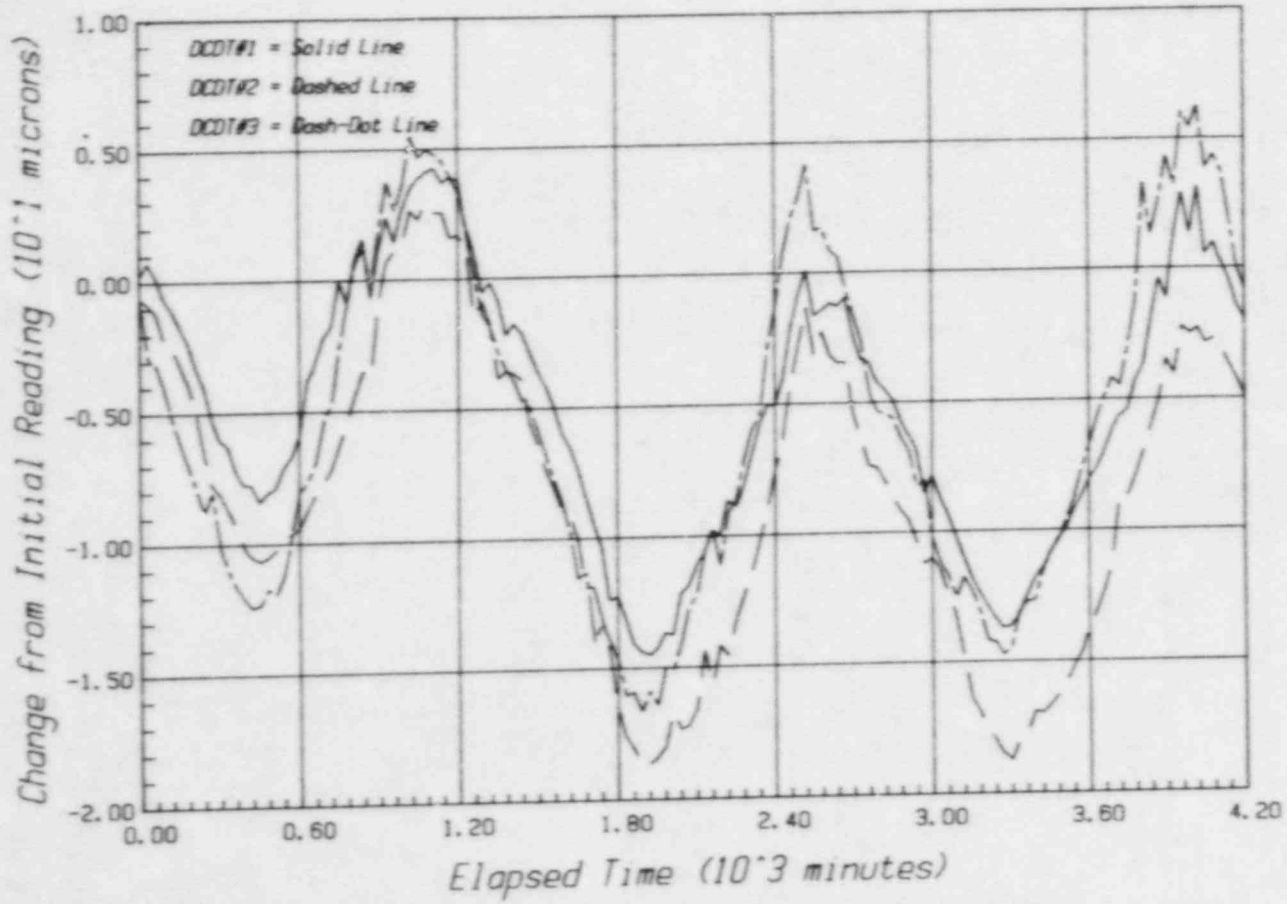

Figure 3.11. DCDT drift measurements.

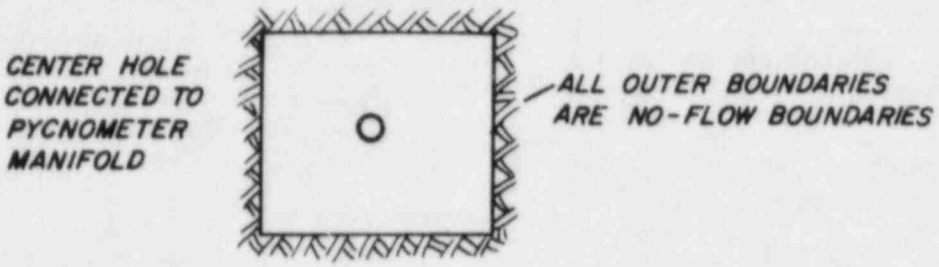

a) BOUNDARY CONDITIONS FOR 1st TEST SERIES.

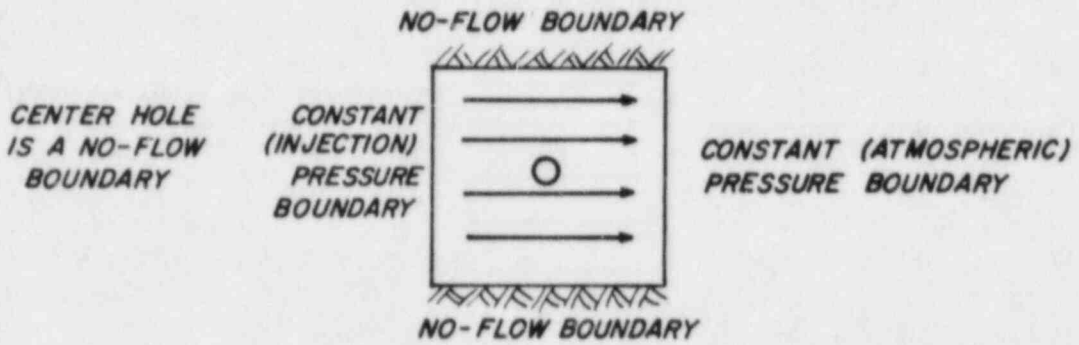

b) BOUNDARY CONDITIONS FOR 2nd TEST SERIES.

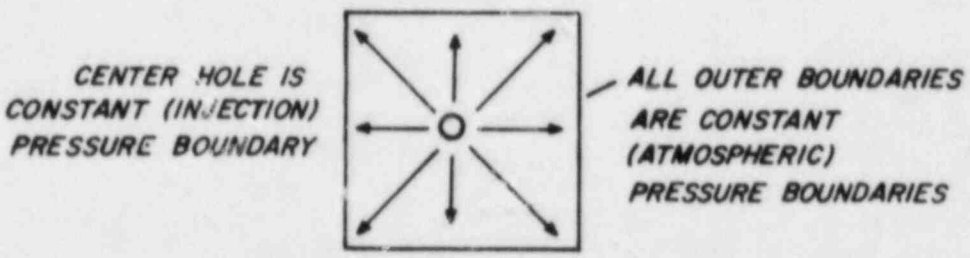

c) BOUNDARY CONDITIONS FOR 3rd TEST SERIES.

Figure 3.12. Sample boundary conditions during testing.

increments using the air pycnometer as coupled through the center hole. Air leaks plagued the pycnometer during the initial test, and a second test was performed using an improved method. The sample base was epoxyed to the sample, and dead space in the center hole was reduced with epoxy filler. Equilibration time between initial and final pressure readings was set at one second, which was found to be sufficient to allow thermodynamic cooling to subside while eliminating any significant influence of minute leaks.

The next test series was begun by remeasuring the fracture volume using the girdle arrangement of the first test series for a reference. The girdle ends were then shifted to open to the intake and exhaust manifold as shown in Figure 3.12b. Following initial fracture volume and flow measurements, the sample was load cycled to 20 MPa with fracture volume, fracture deformation and flow measurements repeated at each stress increment. When unloaded, the sample was jacked open by pressurizing the fracture to extend the measurement range to apertures larger than that of the initial contact.

Fracture volume measurements were made in an identical manner to that of the first test series although connections to the pycnometer manifold assembly were made via the intake manifold while the center hole and exhaust manifold outlets were closed. This increased the total volume measured, sample plus dead space, considerably, and hence the equilibration time was increased to 2 seconds to accommodate the larger pressure drops.

Flow measurements were made by varying flow rate and measuring the associated injection pressure following flow stabilization. At each aperture tested flow rate was varied from 10,000 sccm to 1,000 sccm in increments of 1,000 sccm. Additional measurements at flow rates between 1,000 sccm and 250 sccm were made for several tests. A minimum of 5 readings at intervals of 1 minute were taken at each flow rate to maximize the accuracy of pressure readings.

The final test series was begun by measuring the initial (unloaded) fracture volume using the girdle arrangement of the previous test series. The sample girdle was then removed to achieve the boundary conditions shown in Figure 3.12c, and the sample load cycled to 20 MPa. Fracture deformation and flow measurements were taken at each stress increment in the same manner as for the previous test series. Upon completion of the final test series, the upper sample half was removed and the pressure drop between the injection pressure measurement point and the actual injection point was measured over the range of 1,000 to 10,000 sccm.

3.2 Experimental Results

This subsection presents the results obtained from the tests outlined at the beginning of this section. Included are separate presentations of the fracture aperture and fracture flow measurements. Complete data listings are presented in Appendices B and C. Discussion and interpretation of the experimental results is deferred to Chapter 4.

3.2.1 Fracture Aperture Measurements

Fracture volume and deformation measurements were made during the first and second test series and at the start of the third test series to determine the relationship between true average fracture aperture and deformation aperture and/or to provide a reference aperture. A complete listing of volume and deformation data obtained during these tests is presented in Appendix B.

The first test series was devoted entirely to measurements of fracture deformation and average aperture. Consequently dead space volume contributions from connecting lines could be greatly reduced and accuracy of average aperture measurements increased. Average volumetric aperture, E_v, was computed as the fracture volume divided by its area (see Glossary). Thus E_v is a measurement of the arithmetic average aperture. Fracture deformation aperture, E_d, was computed as the initial volumetric aperture minus the measured fracture deformation as corrected for rock strain (see Glossary).

The apertures E_v and E_d are shown as functions of applied normal stress in Figures 3.13, 3.14, and 3.15, using the data of the first test series. Figures 3.13 and 3.14 represent measurements taken during the first load cycle with the latter representing the loading portion only. During the first load cycle, the measurement procedure was still being perfected and consequently more scatter in the E_v values is observed, particularly for the initial measurements at 0.8 and 1.6 MPa. The scatter is largely attributed to thermodynamic cooling effects resulting in lower E_v values. It is noted that the average E_v values generally correspond well with the E_d values but indicate a divergence during the unloading cycle possibly as a result of permanent strain.

Figure 3.15 represents measurements taken during a second load cycle to 17 MPa at which point the flatjack failed. The sample assembly was completely disassembled and reassembled prior to the second load cycle resulting in a different initial aperture (about 1,000 μm versus 600). Far greater repeatability was obtained for the E_v measurements of the second cycle due to improvement of the measurement technique.

The loading curves of both cycles are identical, indicate an initial contact aperture of about 450 μm, asymptotically approach a minimum aperture of 300 μm with increasing normal stress, and return to an

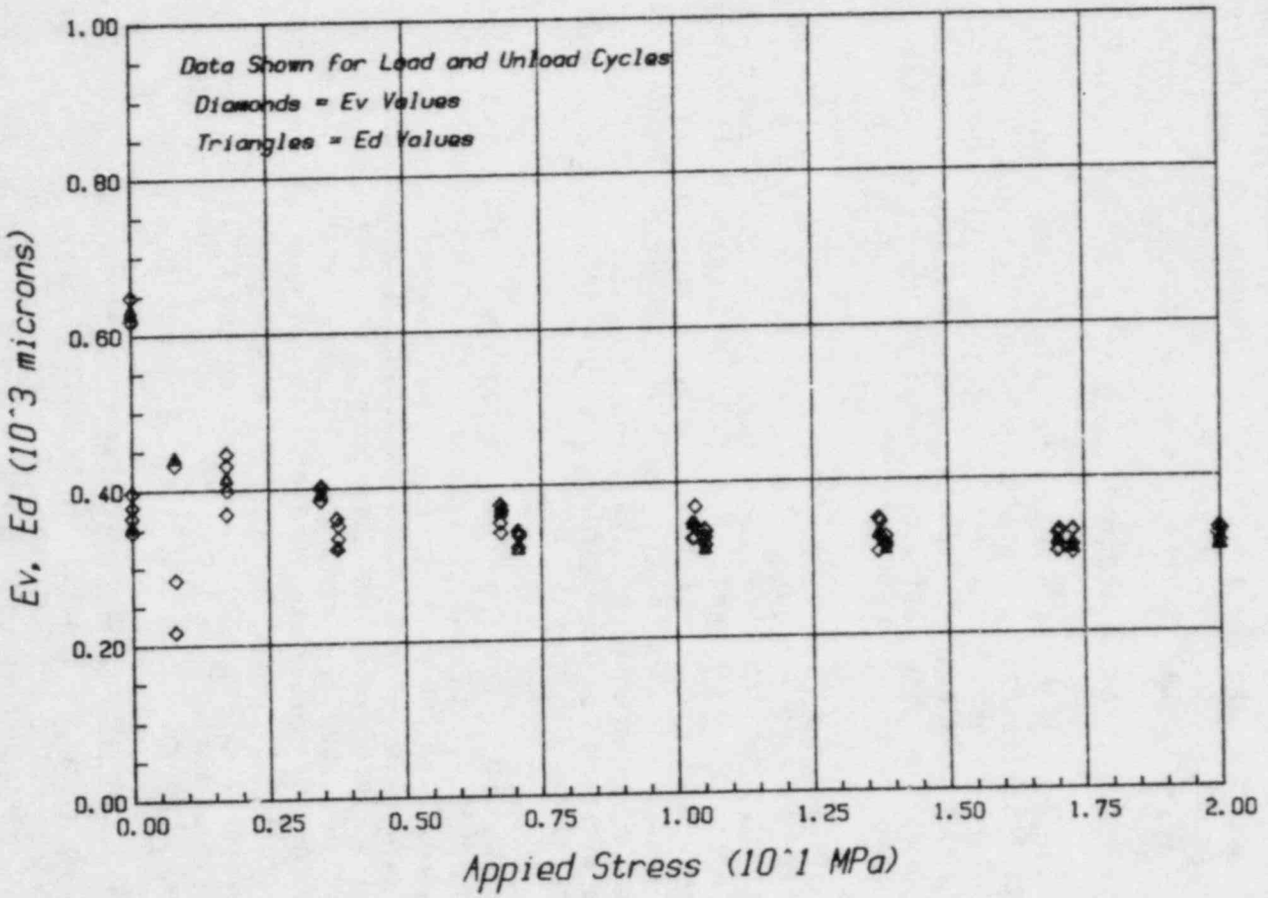

Figure 3.13. E_v and E_d versus applied normal stress for porosity test no. 1.

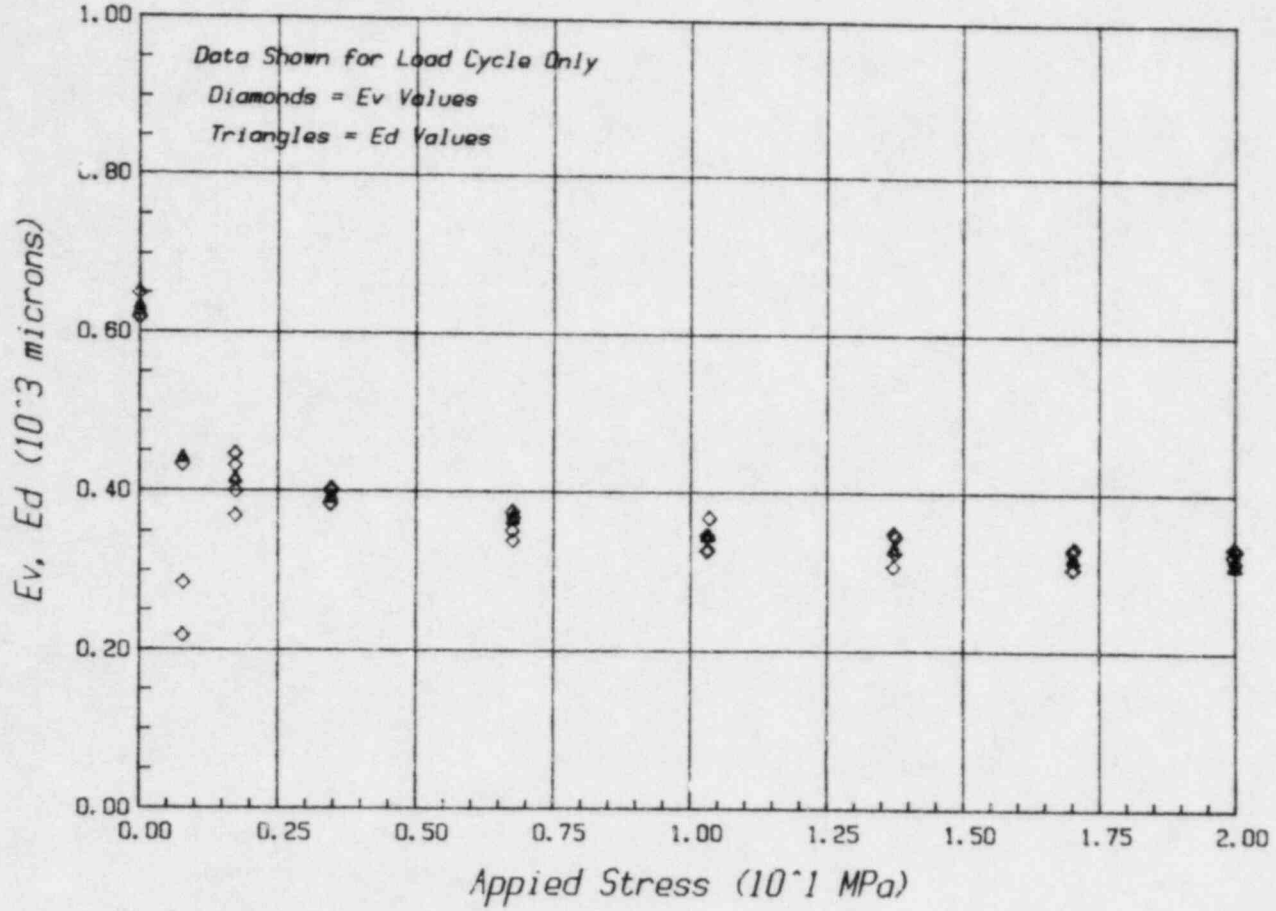

Figure 3.14. E_v and E_d versus applied normal stress for porosity test no. 1 (loading cycle only).

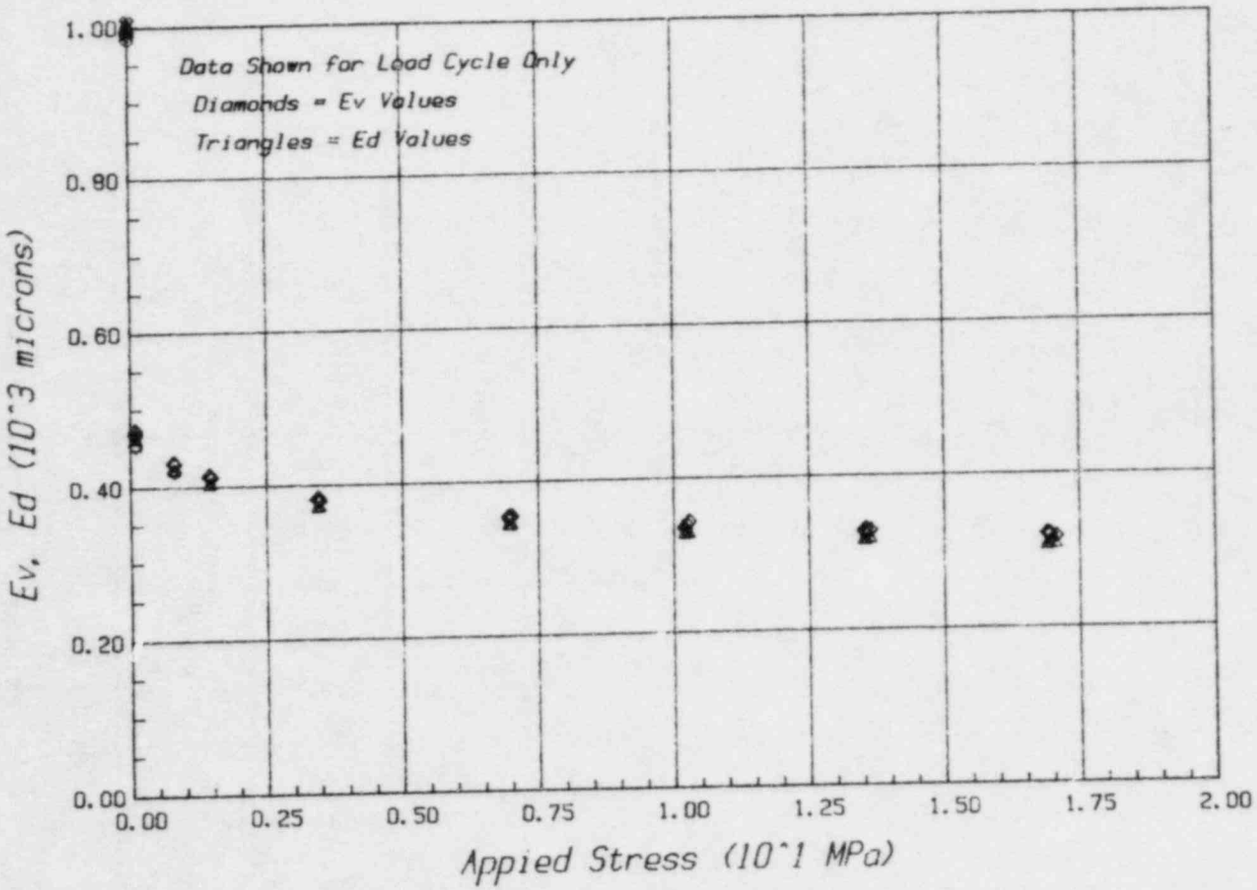

Figure 3.15. E_v and E_d versus applied normal stress for porosity test no. 2 (loading cycle only).

aperture of between 350 and 400 μm upon jack depressurization. Differences between initial and final contact apertures are likely due in part to permanent fracture deformation but are enhanced by a residual stress resulting from flatjack strain. Permanent strains are also a result of improved mating of the fracture surfaces following load cycling.

During the girdle changeover between the first and second test series, an effort was made to compare fracture volume measurements made with both test configurations. Pycnometer measurements were made for each test configuration, while fracture deformation measurements were made during the changeover to correct for fracture movement associated with the changeover. These results, presented in Table 3.2, agree to within 1 cm^3, or in terms of fracture aperture about 15 μm, suggesting an absolute accuracy of this order for the method.

Table 3.2. Comparison of Fracture Volume Measurements for Different Test Configurations*

Test Configuration	Measured Volume	Fracture Volume	Volume Correction	Reference Volume	Average Volume
Porosity	71.96	42.3	3.26	39.0	39.0±0.1
	72.07	42.4	3.45	38.9	
	72.13	42.4	3.47	39.0	
Linear Flow	304.08	31.8	-5.67	37.5	
Field	304.78	32.5	-5.71	38.2	38.0±0.4
	304.78	32.5	-5.65	38.2	

* All volumes expressed in cm^3.

During the second test series, flow measurements were made at each consecutive stress increment, hence the loading cycle was conducted over a period of several days. As a result, some degradation in deformation measurements would be expected due to temperature changes and instrument drift. Furthermore, the dead space volume associated with the fracture

volume measurement increased from 29.7 cm^3 to 272.3 cm^3 reducing measurement accuracy.

The apertures E_v and E_d measured during the second test series are shown in Figure 3.16 as functions of applied normal stress. From this figure it is apparent that both aperture values are somewhat erratic. The E_v values are irregular, particularly in the lower stress range, although the average values are close to the corresponding E_d values as for the first test series. The E_d measurements twice exhibited gradual overnight upward shifts of about 20 μm between stress levels of 1.5 and 2.0 MPa and 7 and 1.3 MPa. These drifts are attributed primarily to overnight cooling effects. Although opposite shifts were not noted during daytime testing, the successive load incrementation for tests run during the same day could mask such changes. For this reason, no effort was made to correct for these shifts.

The loading curve for the second test series indicates smaller apertures at lower stress levels than for the previous test series. This may be a result of better initial mating of the fracture surfaces, as the fracture surfaces were not separated following the previous load cycle. A second possibility is that due to the longer time intervals between successive stress increments, sample creep may be more of a factor. It is of note that the initial contact aperture is approximately the same as the initial contact aperture for the first test series as is the asymptotic aperture.

Near the end of the second test series (tests #9 and 10), the fracture was opened beyond the initial contact aperture by raising the upper platen slightly and pressurizing the fracture. This was done to extend the flow test range to larger apertures. Referring to Figure 3.17 where the E_v and E_d values are presented in their order of measurement, it is seen that for tests #9 and 10 large differences exist between the volumetric and deformation apertures, and between the deformation apertures measured during fracture volume readings and during the flow test. These differences are attributable to the effects of pressurization during pycnometer measurements.

With the upper platen raised slightly and the fracture aperture extended beyond the initial contact aperture, the upper sample half is held in position only by contact with the sample girdle. Furthermore, this contact surface consists of a 3 mm-rubber gasket which allows for relative movement of the sample halves via shear deformation of the gasket. Hence during a pycnometer measurement the fracture aperture increases due to the force exerted by the equilibration pressure against the fracture surfaces resulting in high E_v values. The corresponding E_d values are lower since they are read some 15 seconds later following partial bleed-off of the equilibration pressure. E_d values taken during the flow test are even lower since the flow test pressures are considerably lower than the pycnometer equilibration pressures. It is

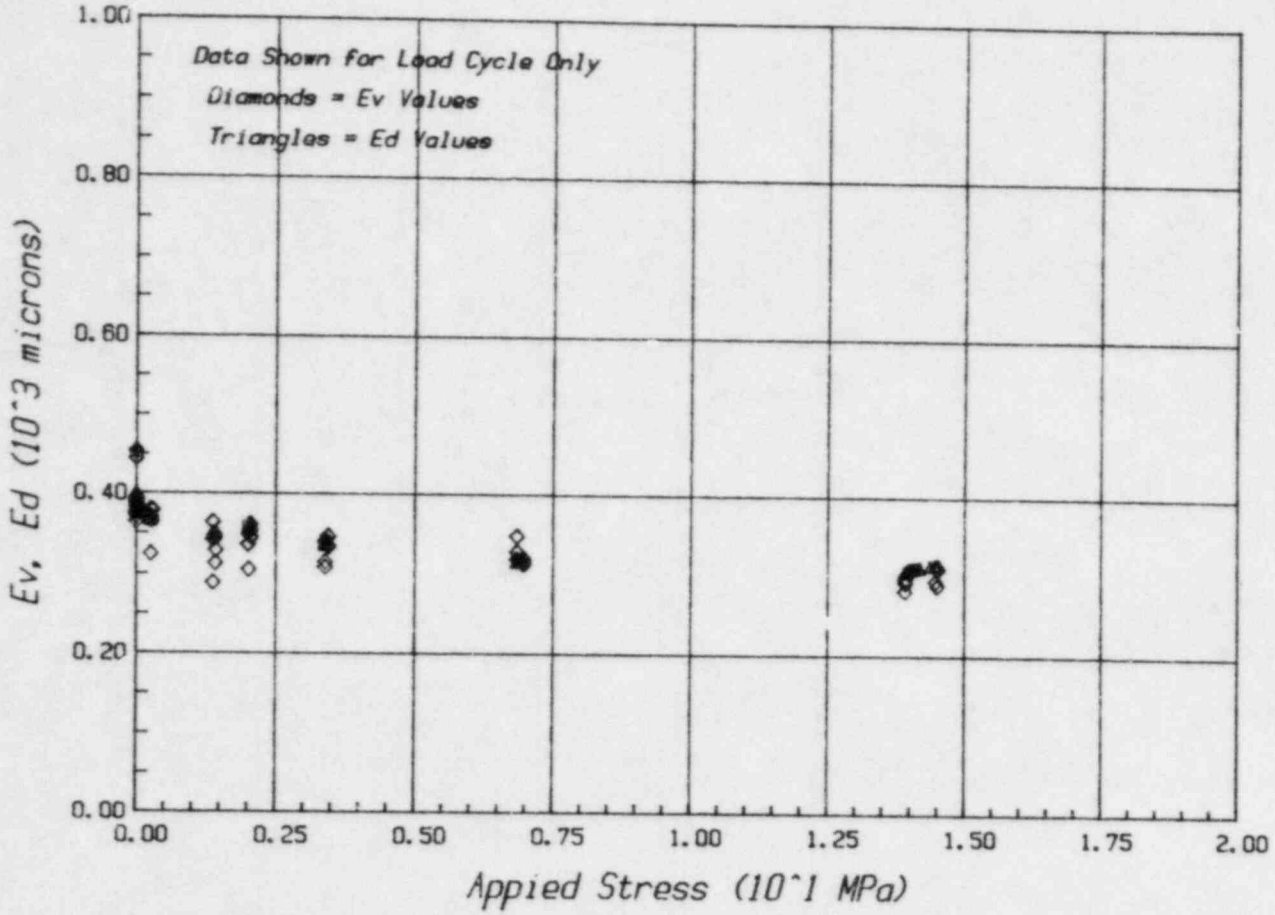

Figure 3.16. E_v and E_d versus applied normal stress for linear flow field tests.

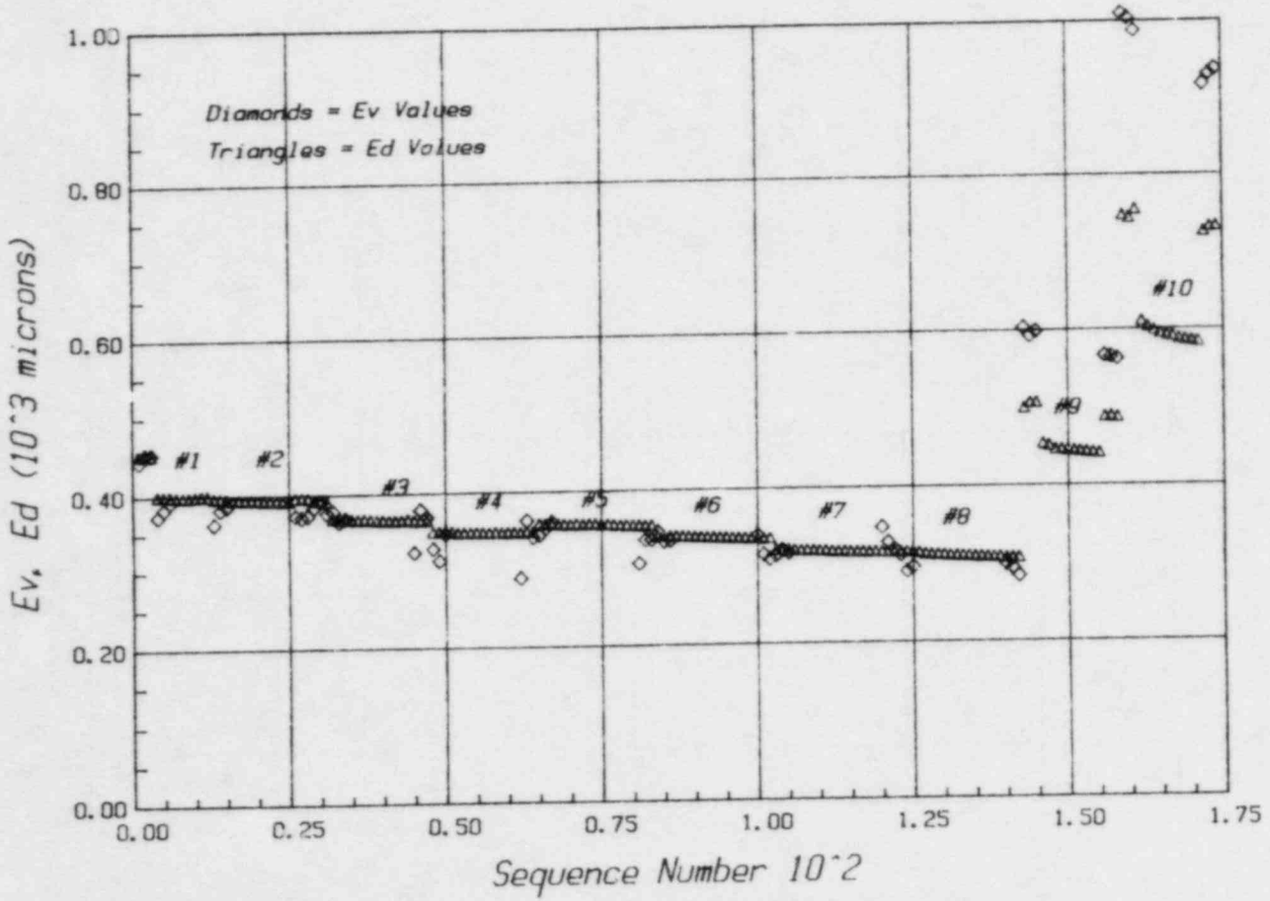

Figure 3.17. Summary of aperture measurements for linear flow field tests.

apparent from the sight decline in the E_d flow test values that even the lower flow test pressures cause slight increases in fracture aperture. It is of note that the E_d flow test values for test #9 are equal to the assumed initial contact aperture of the previous test series. With the above considerations in mind, the E_v and E_d values of the pycnometer measurements for tests #9 and 10 are hereafter ignored, and the E_d flow test values are considered representative.

Measured apertures versus stress for the third test series are shown in Figure 3.18. As for the second test series, an initial fracture volume measurement was made using the girdle configuration of the previous test. At the end of the second test series the fracture was pushed open by pressurizing the fracture, hence the initial aperture was greater than for the second test series. The initial contact aperture is again found to be close to that of the first two test series, however the minimum aperture is about 100 μm less. This is attributable to removal of the sample girdle permitting greater shear displacement and hence better mating of the fracture halves. Although the third test series was conducted over a period of three days, no displacement shifts as noted for the previous test series occurred.

3.2.2 Fracture Flow Measurements

Fracture flow measurements were made during the second and third test series to determine the relationship between fracture aperture and conductivity. A complete listing of flow data obtained during these tests is presented in Appendix C.

Flow measurement results were interpreted using equations (2.31) and (2.35) which can be linearized to the form:

$$\frac{\Delta p^2}{Q_m} = a + cbQ_m^{n-1} \tag{3.5}$$

Hence, the results are presented in plots of $\Delta p^2/Q_m$ as a function of Q_m^{n-1}. Data thus presented should plot as a straight line with intercept a and slope cb, assuming that equation (3.5) is valid and the exponent n is chosen correctly. The coefficients a and cb can then be determined from simple linear regression.

The second test series utilized the test configuration of Figure 3.12b to obtain a linear flow field. This provides a constant pressure squared gradient and a constant mass flow rate along the flow path simplifying interpretation of test results by reducing the number of variables to be considered. A total of ten flow tests were conducted each at a different aperture (Figure 3.17) ranging from 300 to 600 μm.

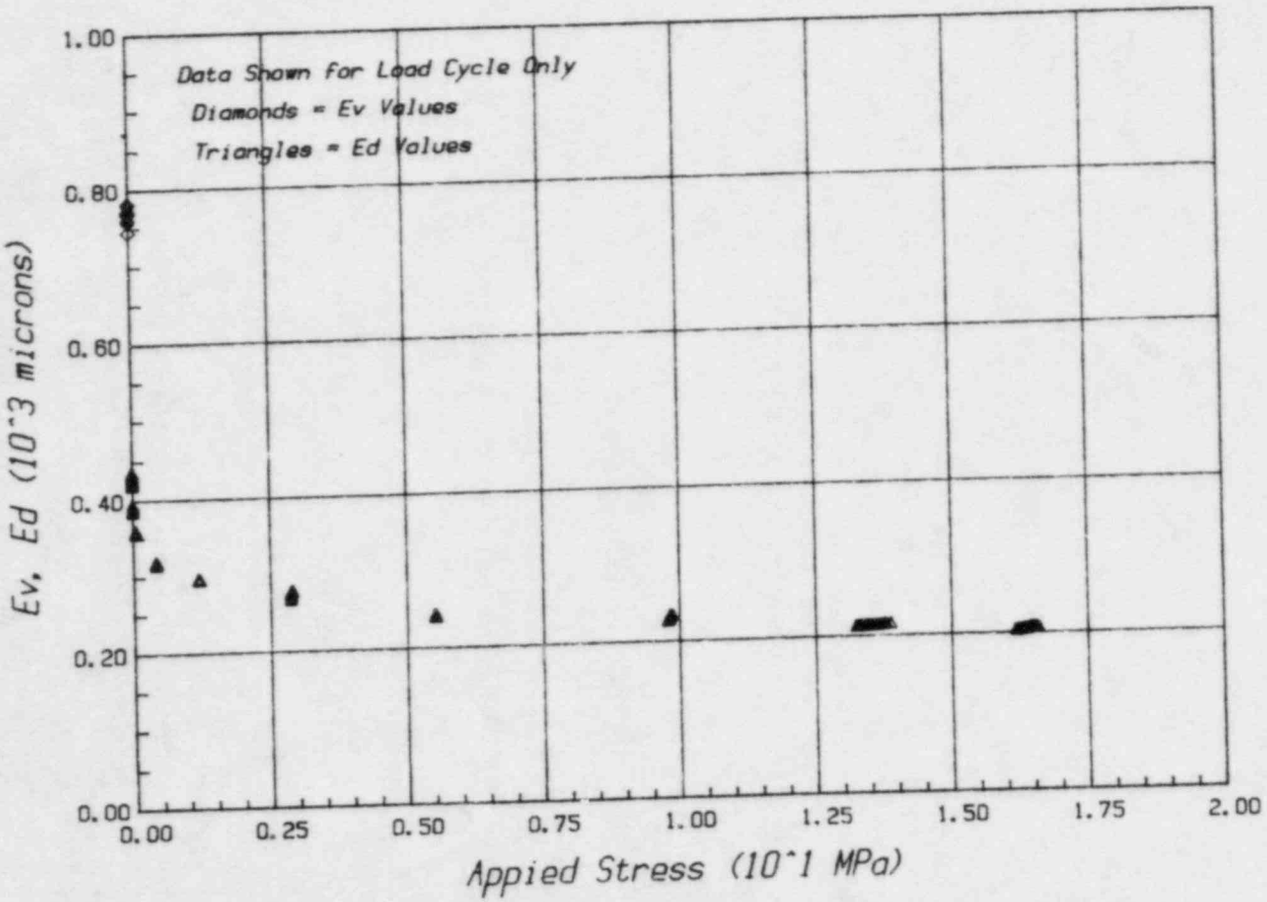

Figure 3.18. E_v and E_d versus applied normal stress for radial flow field tests.

Results of the second test series are presented in Figures 3.19 and 3.20 using the variables of equation (3.5) with n = 2. From these figures it is apparent that the data lie on a straight line as indicated by the plotted linear regression fits. Scatter of the data for Q_m less than 3 x 10^{-5} kg/sec is attributed chiefly to errors in pressure measurement since gage injection pressures are less than 1 kPa (.01 atm) at such low flow rates. These errors are magnified in computing the value $\nabla p^2/Q_m$.

The numbers used for plotting symbols in Figures 3.19 and 3.20 represent the test number. Tests #1 and 2 were conducted at essentially identical apertures and indicate the relative repeatability of the measurement. Also of note is the increase in slope or magnitude of the nonlinear term with decreasing aperture. Indeed this monotonic increase in both coefficients a and b, which are inversely related to fracture conductivity, suggest that the overnight deformation shifts previously noted between tests #4 and 5, and #7 and 8, are not related to actual fracture deformation. For test #10, which was conducted with the fracture surfaces completely separated, the coefficient b is nearly zero indicating that the nonlinear term is related to fracture mating.

The third test series utilized the test configuration of Figure 3.12b to obtain a nearly radial flow field. This creates a steep pressure squared gradient near the injection boundary and a mass flow rate which varies inversely with distance from the injection boundary. The nonlinear term of equation (3.5) further increases the steepness of the pressure squared gradient near the injection boundary. Consequently the flow characteristics of the fracture surface near the injection boundary bias the test results. Eleven radial flow field tests were conducted (Figure 3.21) at apertures ranging from about 425 to 200 μm.

Limited access to the central injection hole during the third test series required that the injection pressure be measured at the connecting line entrance near the base of the sample (Figure 3.6). To account for pressure losses between the measurement and injection points, the pressure drop as a function of mass flow rate was measured with the pressure at the injection point equal to atmospheric pressure (upper sample half removed) following completion of the test series. Two such tests were performed to assure repeatability of results and the data fit to equation (3.5) with n = 1.9 (Figure 3.22). Although this equation does not accurately represent the low pressure points, it was found to be the most accurate overall pressure correction of various correction equations tried. In light of observed measurement errors in the low pressure range, it is believed that a separate pressure correction formula for the low pressure range was unwarranted.

Results of the third tests series, using the corrected injection pressure, are presented in Figures 3.23 and 3.24 in the same manner as for the previous test series. As before, the data lie close to a straight line as indicated by the plotted linear regression fits; however, there

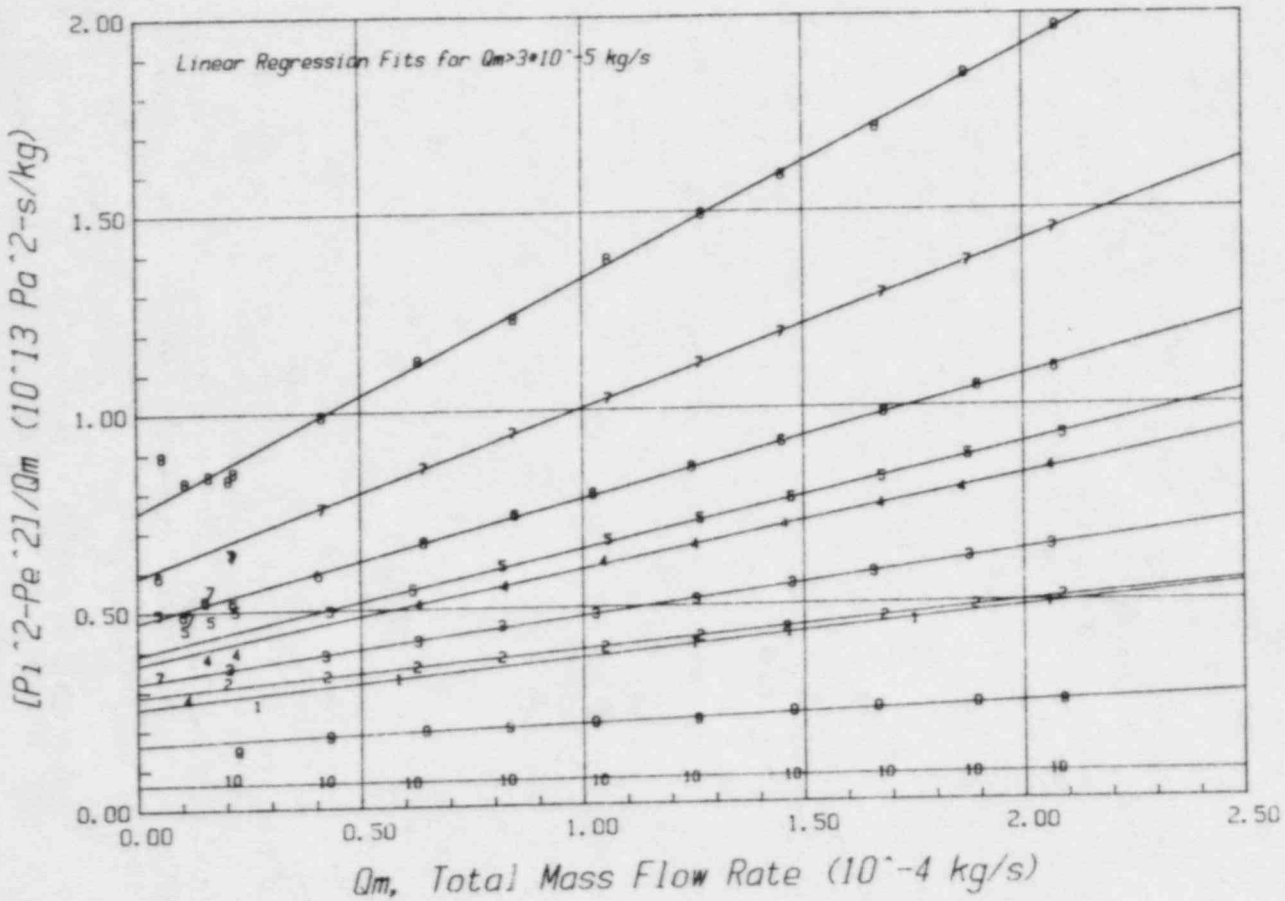

Figure 3.19. Pressure-flow rate data for all linear flow field tests with n = 2.

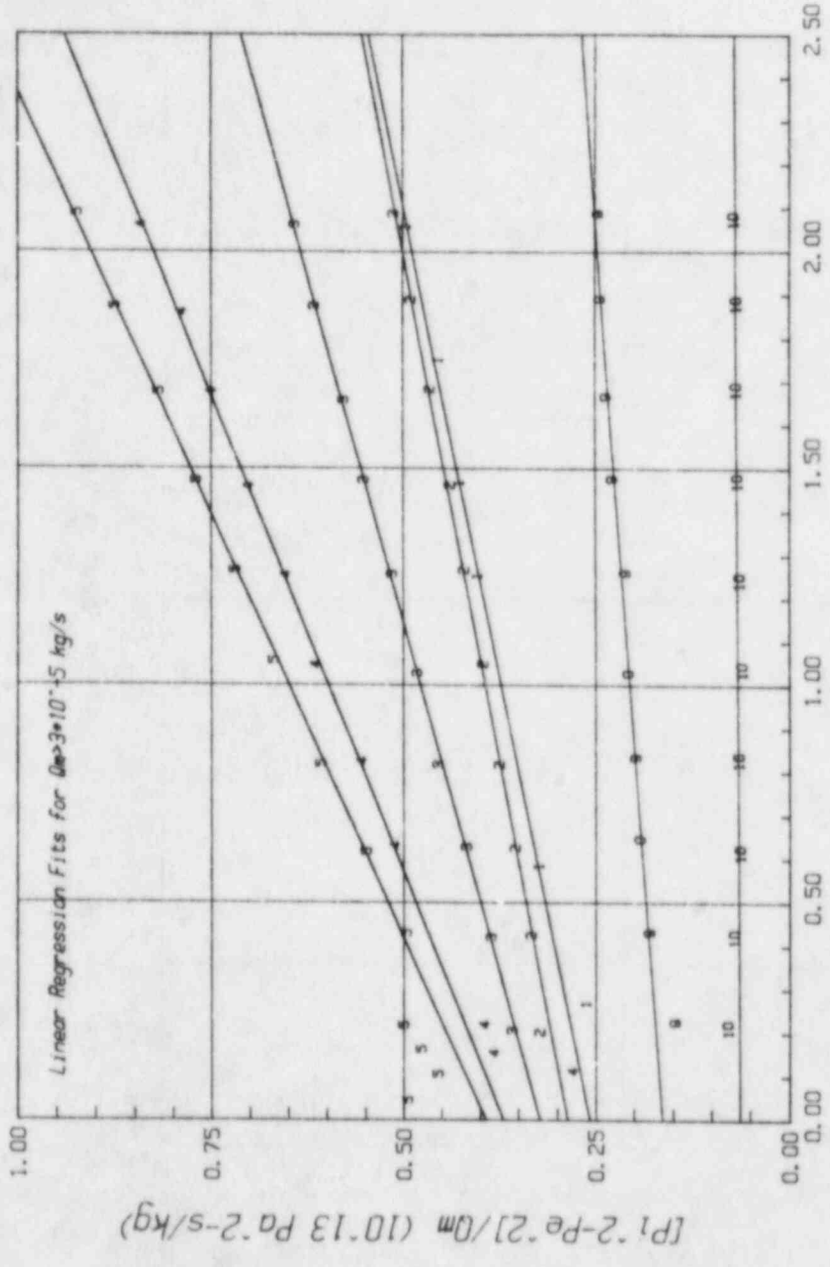

Figure 3.20. Pressure-flow rate data for linear flow field tests no. 1-5, 9, and 10 with n = 2.

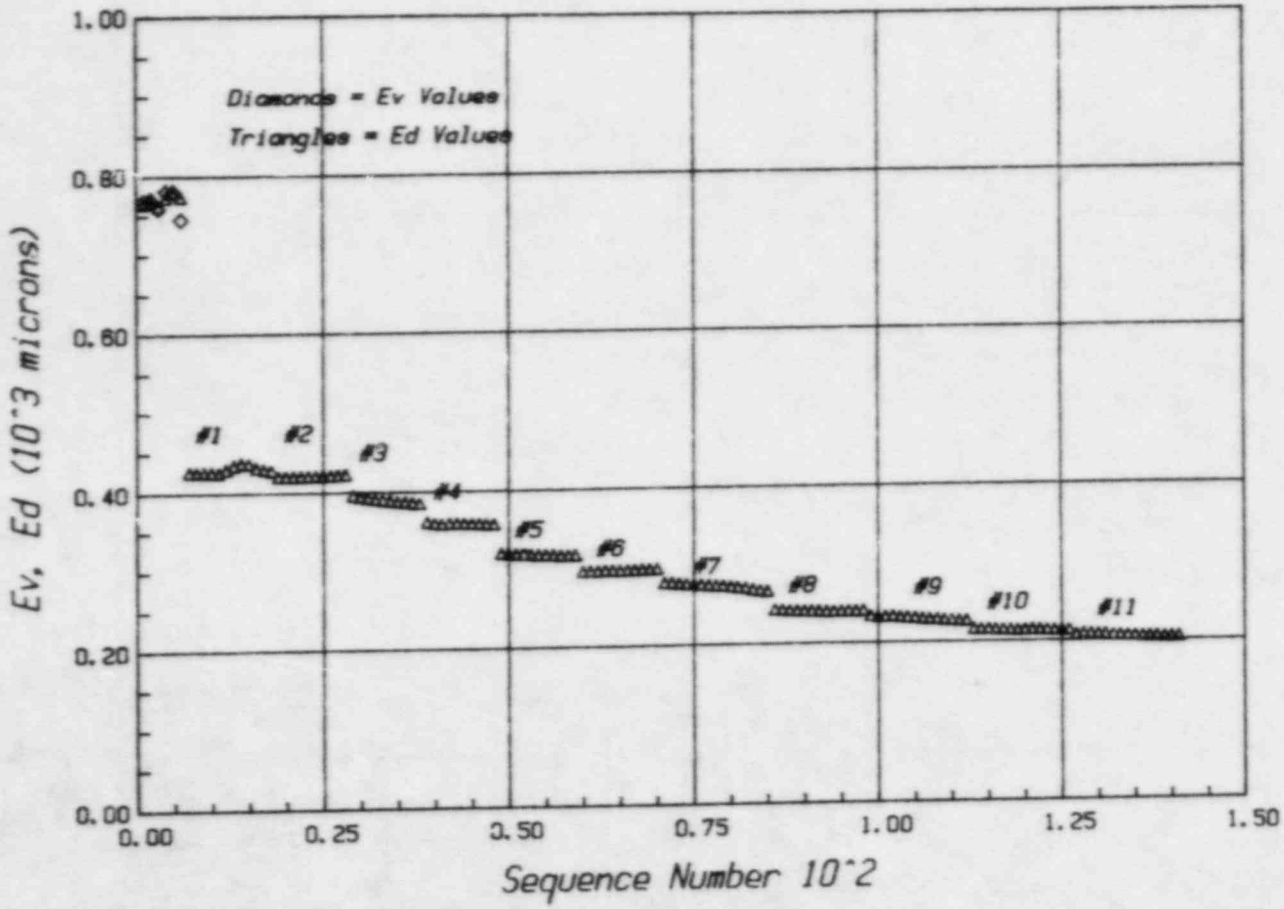

Figure 3.21. Summary of aperture measurements for radial flow field tests.

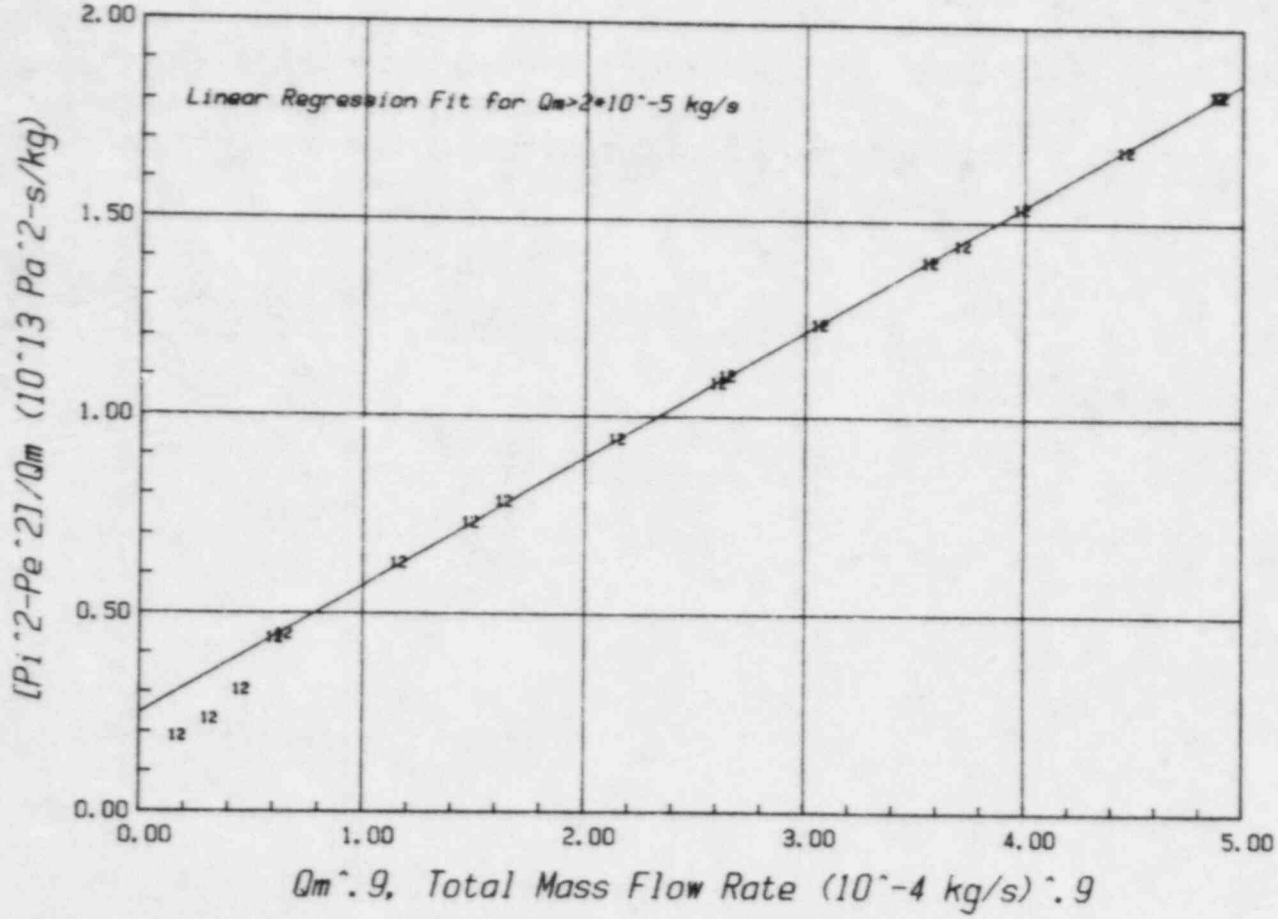

Figure 3.22. Injection pressure correction for radial flow field tests.

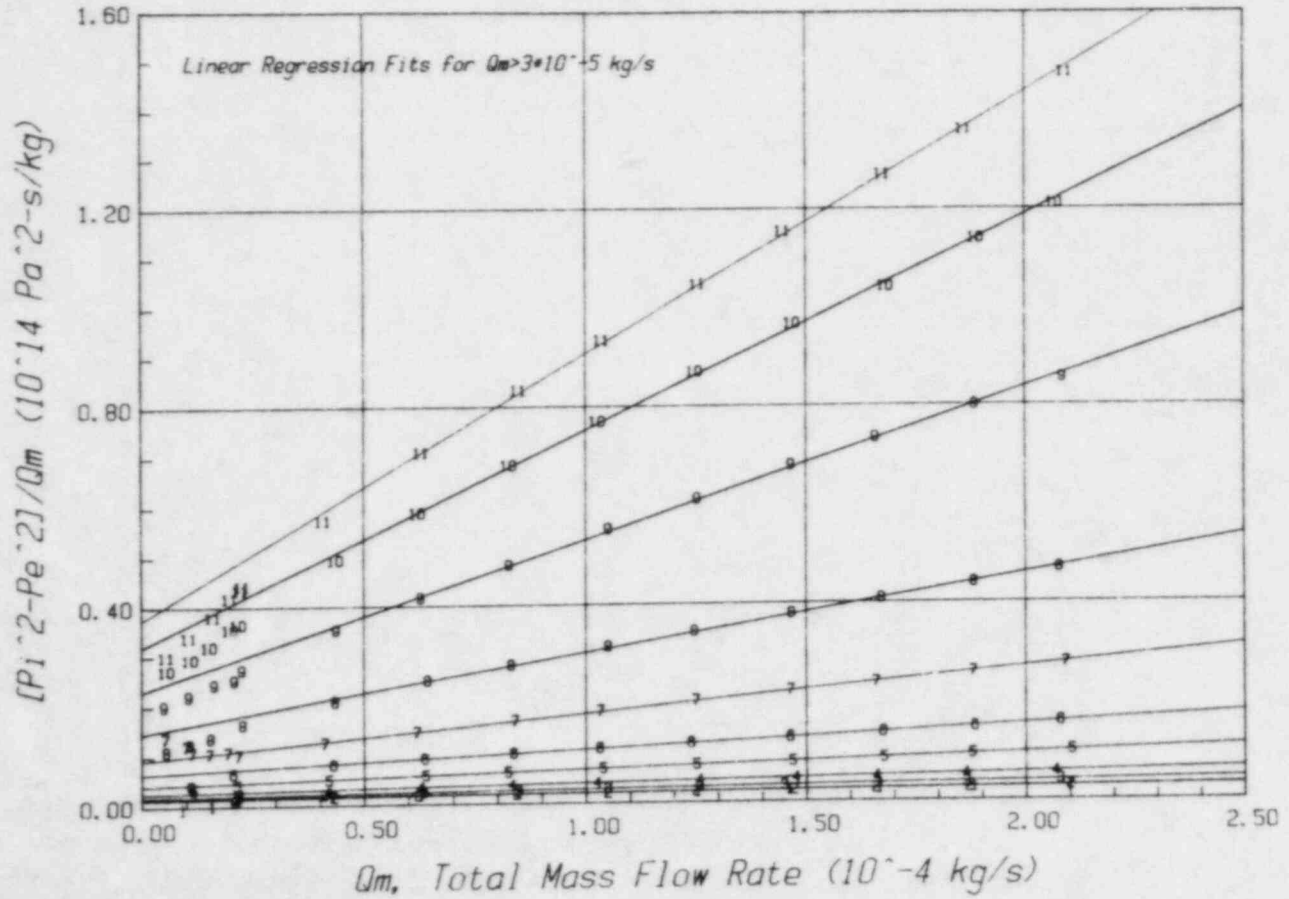

Figure 3.23. Pressure-flow rate data for all radial flow field tests with n = 2.

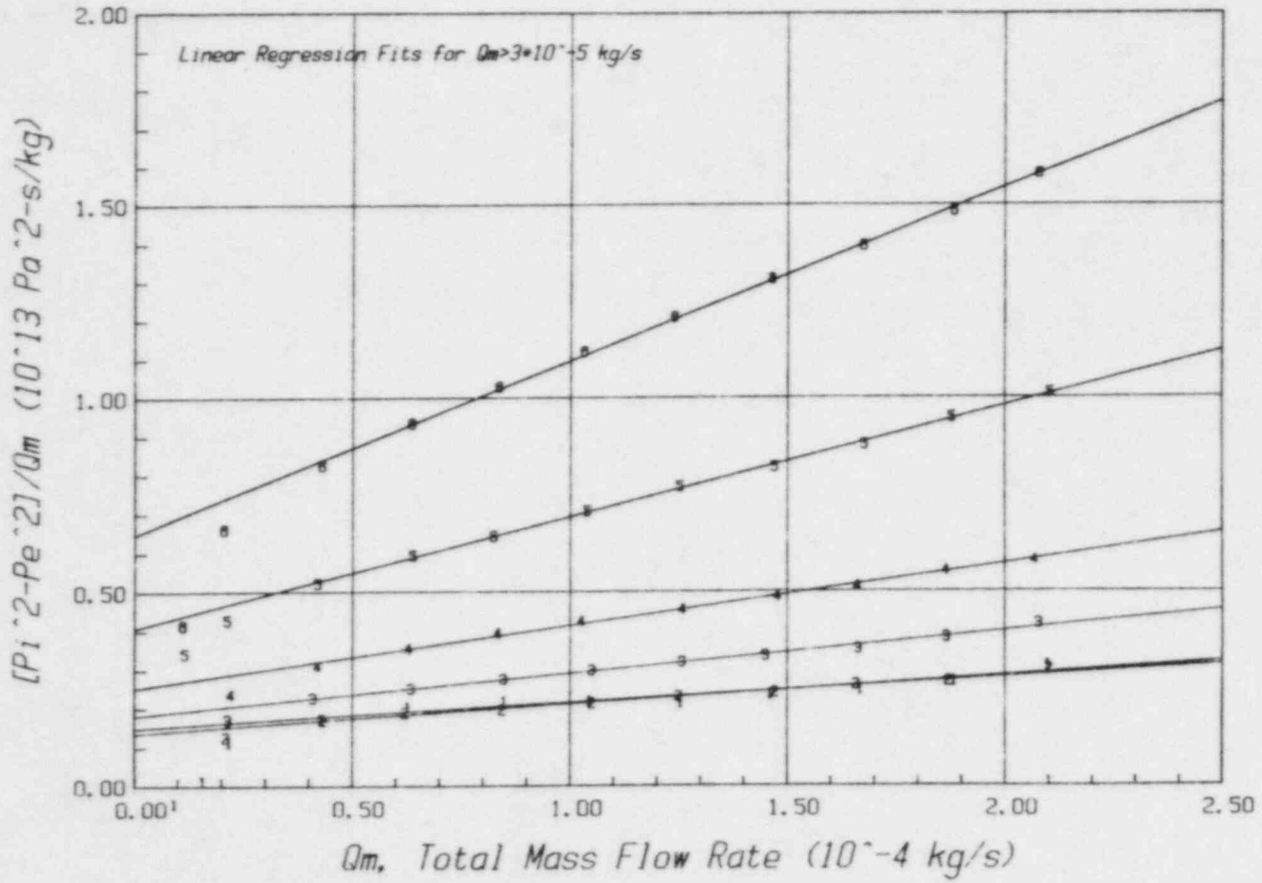

Figure 3.24. Pressure-flow rate data for radial flow field tests no. 1-6 with n = 2.

is a slight downward curvature, particularly for the higher injection pressure tests #8 through 11. This curvature may be partly due to errors in the injection pressure correction, particularly for low Q_m values. Another possibility is that the use of a radial flow approximation is less suitable at higher injection pressures where the outer rectangular boundary shape has a greater influence on the pressure squared gradient.

A third possibility is that necking of the flow, due to the abrupt change in flow cross section at the injection boundary, delays the onset of turbulent flow. Such an effect is of far greater influence in radial flow as a consequence of the larger velocities and associated pressure losses near the injection boundary. Studies of parallel plate flow have indicated the length of the laminar zone varies inversely with the Reynold's number for fully turbulent flow (Rissler, 1978). Since the mass flow rate is directly proportional to the Reynold's number, this effect is only significant for lower flow rates. This phenomenon may explain the initial nonlinearity of the radial flow data of Figures 3.23 and 3.24.

An improved fit to equation (3.5) is obtained if the exponent n is set equal to 1.82. Results of this substitution are plotted in Figures 3.25 and 3.26. In this case the fits of the higher injection pressure tests are significantly improved while those of the remaining tests are not. Since the lower pressure injection tests fall in the same pressure range as the linear flow tests, the exponent n may be a function of the pressure squared gradient. Alternatively the fit of equation (3.5) may be less sensitive to the choice of the exponent n at lower pressure squared gradients.

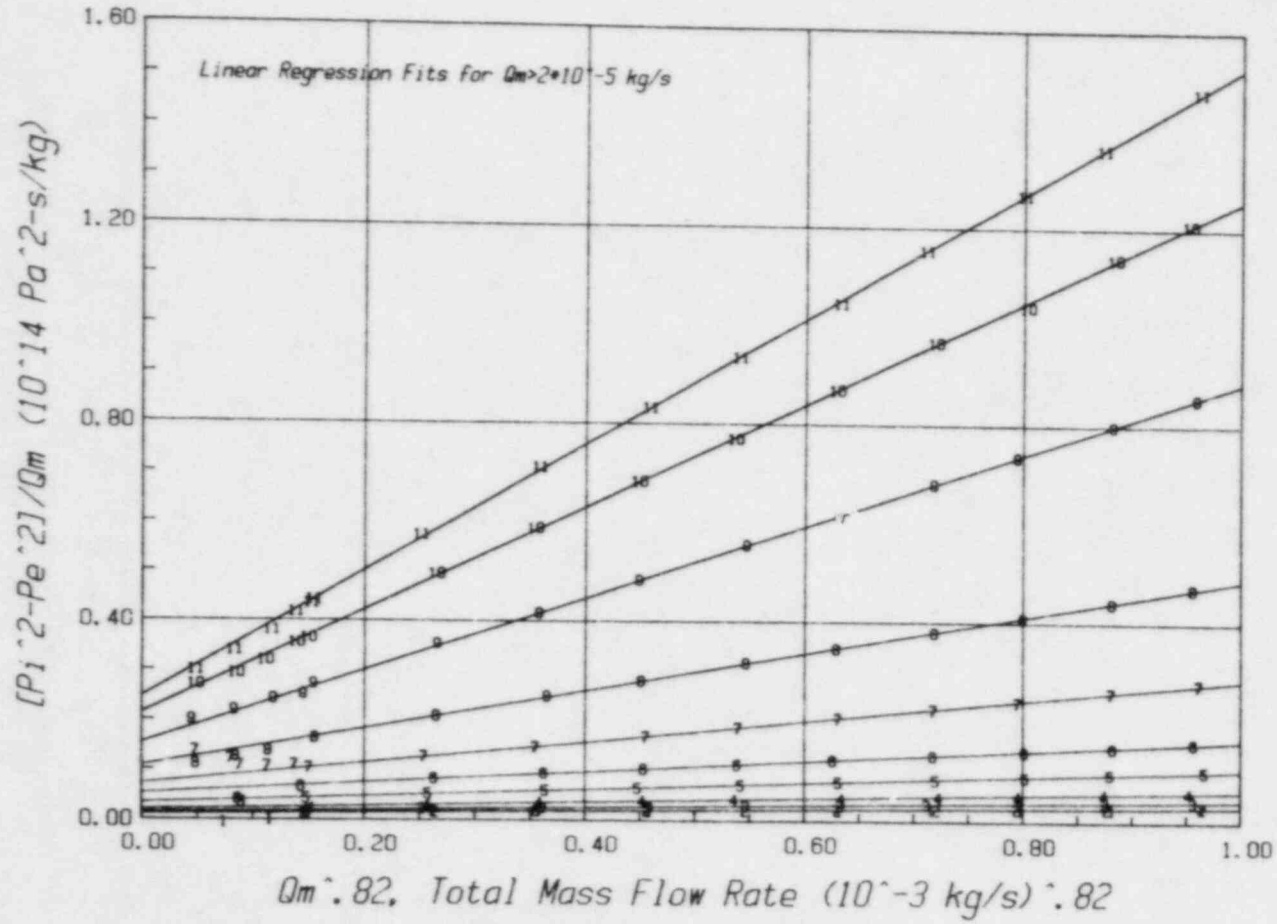

Figure 3.25. Pressure-flow rate data for all radial flow field tests with n = 1.82.

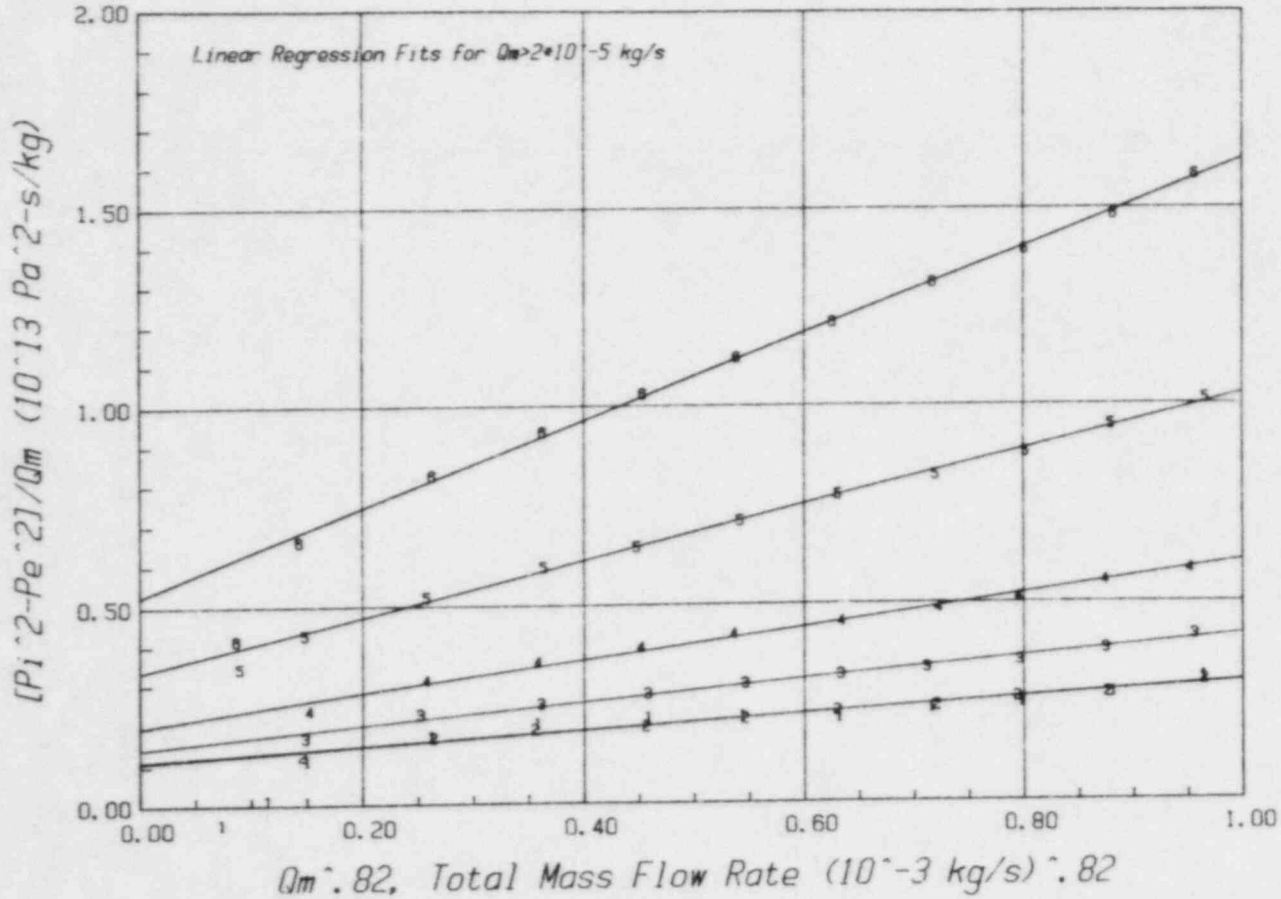

Figure 3.26. Pressure-flow rate data for all radial flow field tests no. 1-6 with n = 1.82.

4. DISCUSSION OF RESULTS

The experimental results presented in the previous chapter are evaluated in this section in an effort to provide a unified interpretation of all test results. As before, the fracture aperture and flow measurements are considered separately.

4.1 Comparison of Average and Deformation Apertures

Previously, it was noted that the average and deformation apertures were nearly identical for all tests conducted. The relationship between E_v and E_d is examined directly in Figures 4.1, 4.2, and 4.3. From these figures it is seen that for the greater part the data lie along the line $E_v = E_d$. The few data points which lie considerably above this line are associated with aperture measurements made during extension of the fracture and are therefore believed in error for reasons previously discussed.

Three fracture closure models were examined in Section 2.4 to determine the relationship between E_v and E_d. On the basis of these models, it is found that fracture deformation must be largely a result of shear displacement which allows for better mating of the fracture surfaces. This hypothesis is confirmed by the greater observed fracture closure of the third test series in which removal of the sample girdle reduced lateral sample confinement.

Also of interest is the fact that initial fracture contact, following fracture extension beyond initial contact, was found to be the same for all tests run (about 450 μm). This result indicates that crushing of asperities or permanent deformation of the fracture surface does not occur. Indeed, no evidence of damage to the fracture surface was observed upon examination at the conclusion of all testing. Although considerable permanent fracture strain occurred following initial load cycling, this is attributed to improved mating of the fracture surfaces via either overall shear displacement of the fracture surface or localized shear deformation of asperities. Permanent normal deformation of asperities would be of insufficient magnitude to fully account for the observed permanent strain.

4.2 Evaluation of Flow Equation Constants

The constants a and b of the flow equations (2.31) and (2.35) are determined from the intercept and slope, respectively, of $(P_1^2 - P_2^2)/Q_m$ as a function of Q_m^{n-1}. In the analysis of this data, the intrinsic permeability is assumed to be given by $k = e^2/12$. By virtue of this substitution, the coefficients a and b of equations (2.31) and (2.35) are seen to be inversely proportional to e^3, and hence the ratio of b to a is theoretically a constant. The substitution $k = e^3$ is considered preferable for the analyses considered here to the definitions ke and

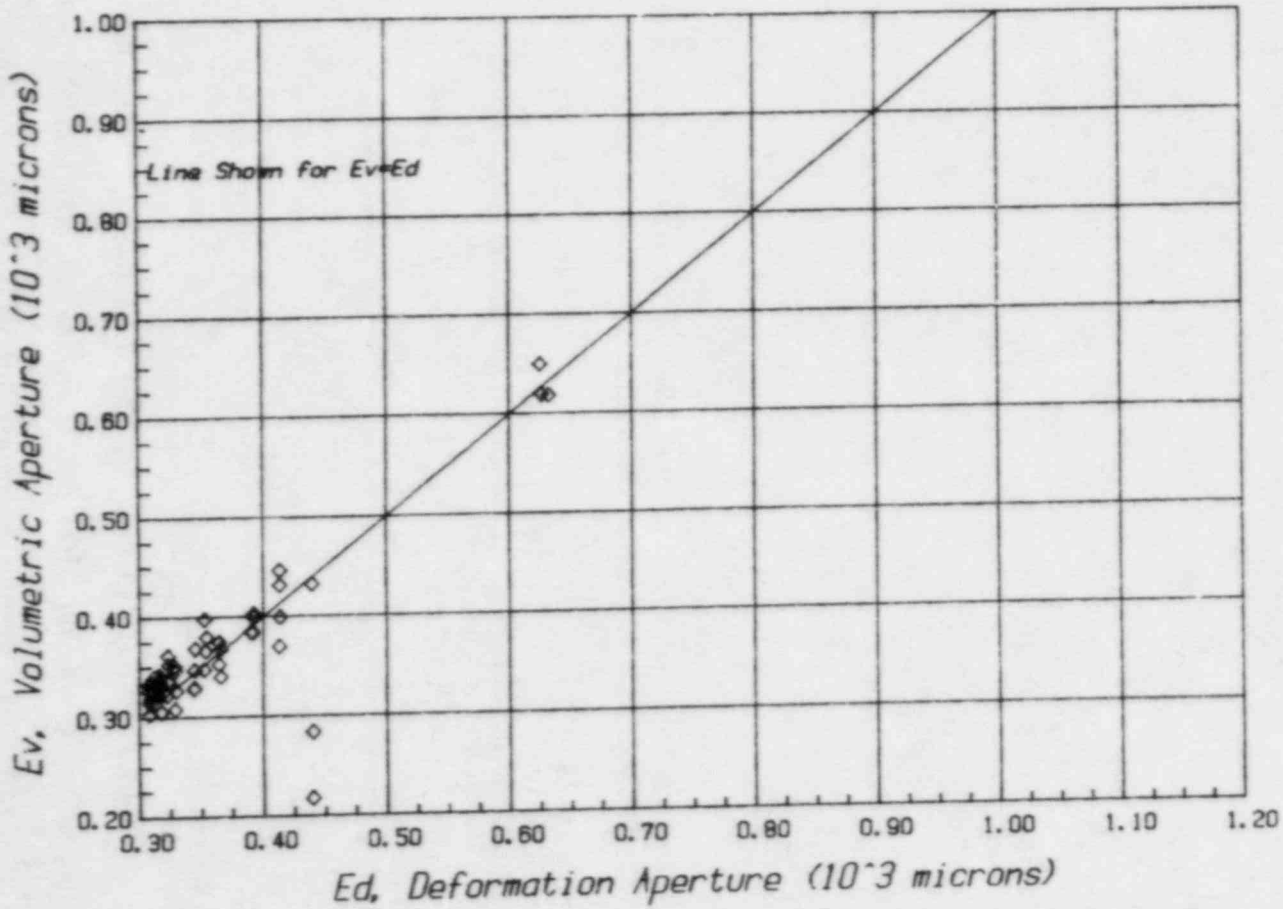

Figure 4.1. E_v versus E_d for porosity test no. 1.

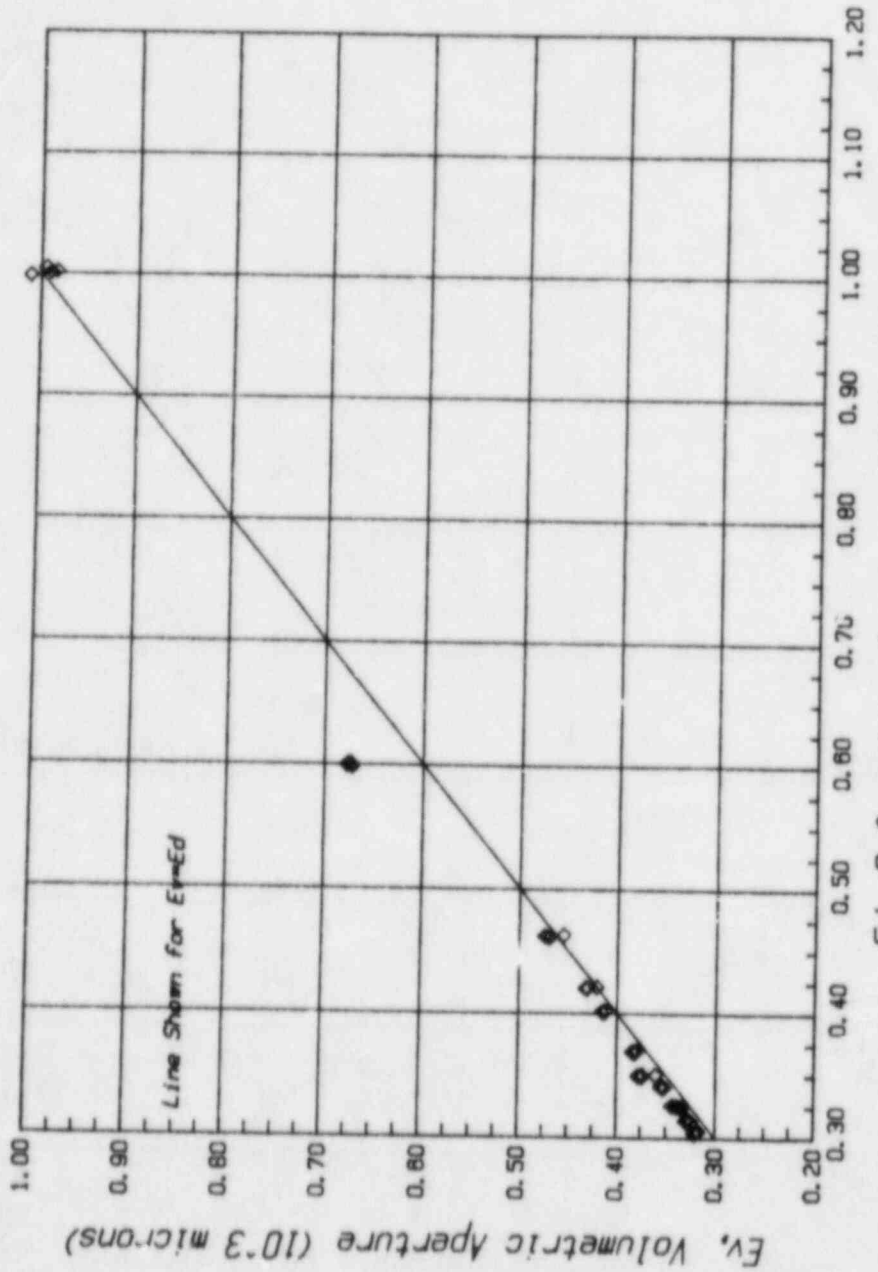

Figure 4.2. E_v versus E_d for porosity test no. 2.

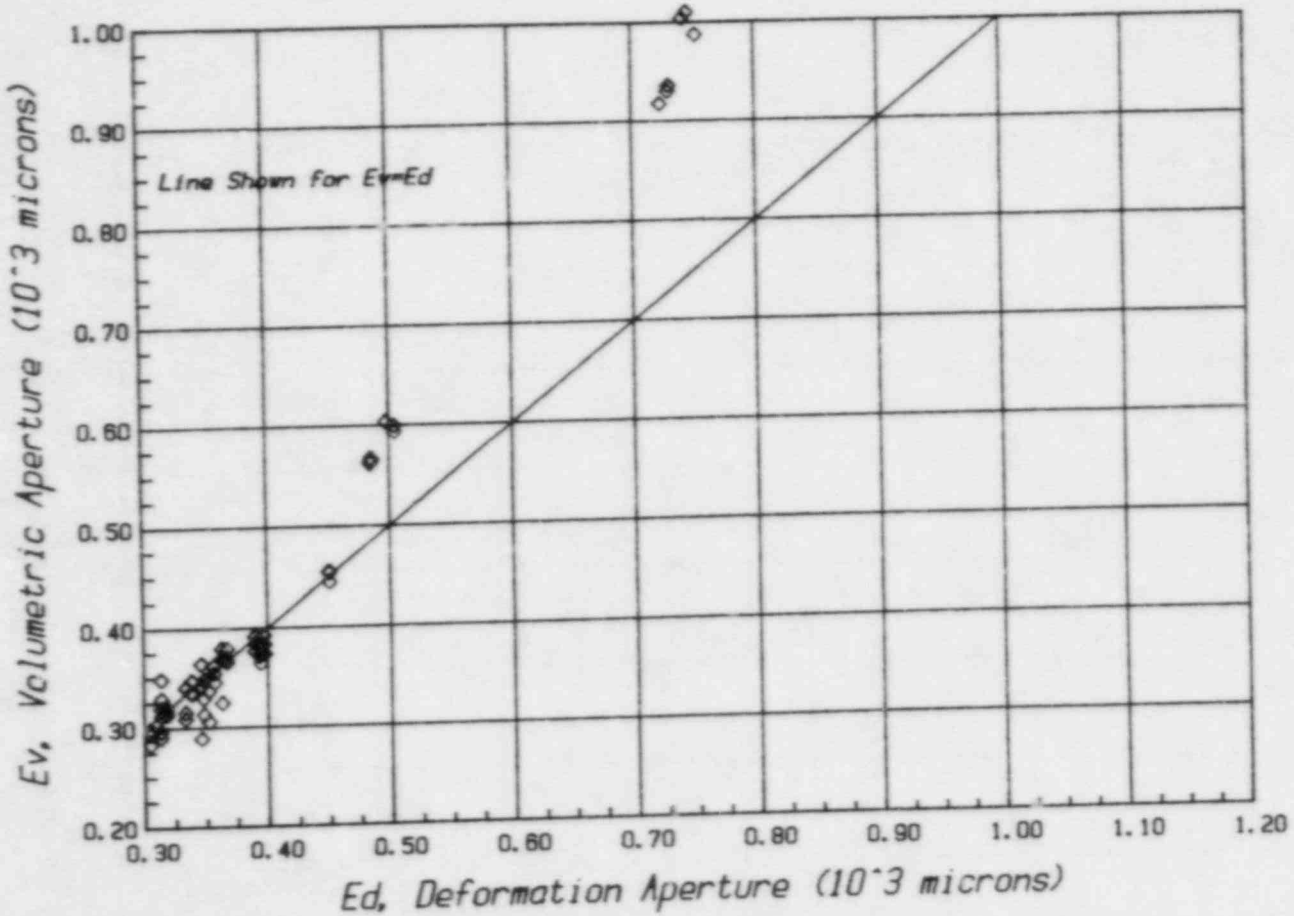

Figure 4.3. E_v versus E_d for linear flow field tests.

$k^{1/2}e^2$ since it eliminates the need to consider two separate parameters. The value of e is easily determined from the measured coefficient a using the known fluid properties and sample geometry. This value of e is hereafter referred to as the hydraulic aperture, e_h, to distinguish it from the mean aperture, $\bar{e}$ (see Glossary). The coefficient c is then calculated from the measured slope using the hydraulic aperture e_h. On the basis of the previous section the average aperture is assumed equal to the deformation aperture e_d and is referred to as $\bar{e}$.

Results of the calculations of e_h and c are presented in Tables 4.1 and 4.2 for the linear and radial flow cases, respectively. Good agreement is found between the linear and radial flow field constants at similar apertures although the assumed dimensionless constant, c, is seen to vary with both aperture and the exponent of the nonlinear term.

From these data it is evident that the computed hydraulic aperture is considerably smaller than the corresponding mean aperture in all cases. The relationship between e_h and $\bar{e}$ is shown in Figure 4.4 and suggests that $e_h = c_1\bar{e} + c_2$. The fact that $c_1 < 1$ can be interpreted to mean that the permeability k is reduced by a factor $c^* = (e_h/\bar{e})^3 < 1$, although c^* must be a function of $\bar{e}$ since c_2 does not equal 0. The cube of the ratio is used here since in the initial calculations ke was assumed equal to ke_h and not $k\bar{e}$.

As discussed in detail in Section 2.1.1, reduction of a rough natural fracture's conductivity over that of an equivalent parallel plate model is attributable to surface roughness, waviness of the fracture surface, and contact area.

Louis (1969) derived an empirical equation to account for surface roughness based on parallel plate flow studies. Using a surface roughness index S, defined as the mean asperity height, λ, divided by the hydraulic diameter, $2\bar{e}$, he found:

$$c^* = \frac{1}{1+8.8(S)^{1.5}} \qquad (S>0.033) \qquad (4.1)$$

Values of c^* as computed from the ratio $(e_h/\bar{e})^3$ were used to determine the parameters S and λ, as shown in Table 4.3. The values of the parameter λ are found to be nearly constant and reasonable in light of the observed asperity height. Further, λ is close to the assumed initial contact aperture of 450 μm, which would be expected for a well mated fracture.

The relationship between e_h and $\bar{e}$ as predicted by equation (4.1) with λ = 500 microns is shown in Figure 4.5. Although the observed fit is excellent, it is cautioned that this may simply be fortuitous as equation (4.1) is based on water flow measurements for $0.033 < S < 0.4$.

Table 4.1. Linear Flow Field Test Results

Test No.	Coeff a ($10^{12}Pa^2/kg/s$)	Coeff b ($10^{16}Pa^2/kg^2/s^2$)	$\bar{e}$ (μm)	e_h (μm)	C
1	2.580	1.149	396.7	233.4	0.0759
2	2.875	1.066	391.4	225.1	0.0632
3	3.225	1.556	364.5	217.5	0.0832
4	3.698	2.282	346.6	207.9	0.1065
5	3.933	2.564	354.9	203.1	0.1116
6	4.747	3.028	336.3	190.9	0.1095
7	5.899	4.158	315.6	177.7	0.1213
8	7.522	5.836	308.3	163.6	0.1328
9	1.640	0.415	442.7	272.2	0.0435
10	0.631	0.0257	590.1	374.4	0.0070

Table 4.2. Radial Flow Field Test Results

Test No.	Coeff a (10^{12} Pa^2/kg/s)	Coeff b (10^{16} Pa^2/kg^n/s^n)	$\bar{e}$ (μm)	e_h (μm)	C
With exponent n = 2					
1	1.288	0.7845	427.5	211.2	0.0583
2	1.255	0.8082	418.6	217.9	0.0720
3	1.671	1.178	387.5	197.2	0.0785
4	2.322	1.738	356.1	176.6	0.0828
5	3.912	2.967	315.2	151.0	0.0927
6	6.158	4.701	294.1	129.4	0.0915
7	8.990	9.046	272.2	114.5	0.1246
8	13.92	16.21	238.8	98.8	0.1426
9	20.94	31.70	227.8	85.0	0.1759
10	30.02	44.71	211.7	76.1	0.1802
11	34.25	55.40	203.3	72.2	0.1888
With exponent n = 1.82					
1	1.133	0.1839	427.5	231.1	0.1666
2	1.099	0.1887	418.6	233.8	0.1774
3	1.446	0.2747	387.5	212.4	0.1931
4	1.983	0.4063	356.1	191.5	0.2097
5	3.344	0.6921	315.2	161.3	0.2133
6	5.258	1.096	294.1	138.7	0.2147
7	7.266	2.109	272.2	124.4	0.2988
8	10.78	3.787	238.8	109.4	0.3649
9	15.48	7.310	227.8	96.9	0.4884
10	21.44	10.43	211.7	86.9	0.5042
11	24.69	12.78	203.3	83.0	0.5372

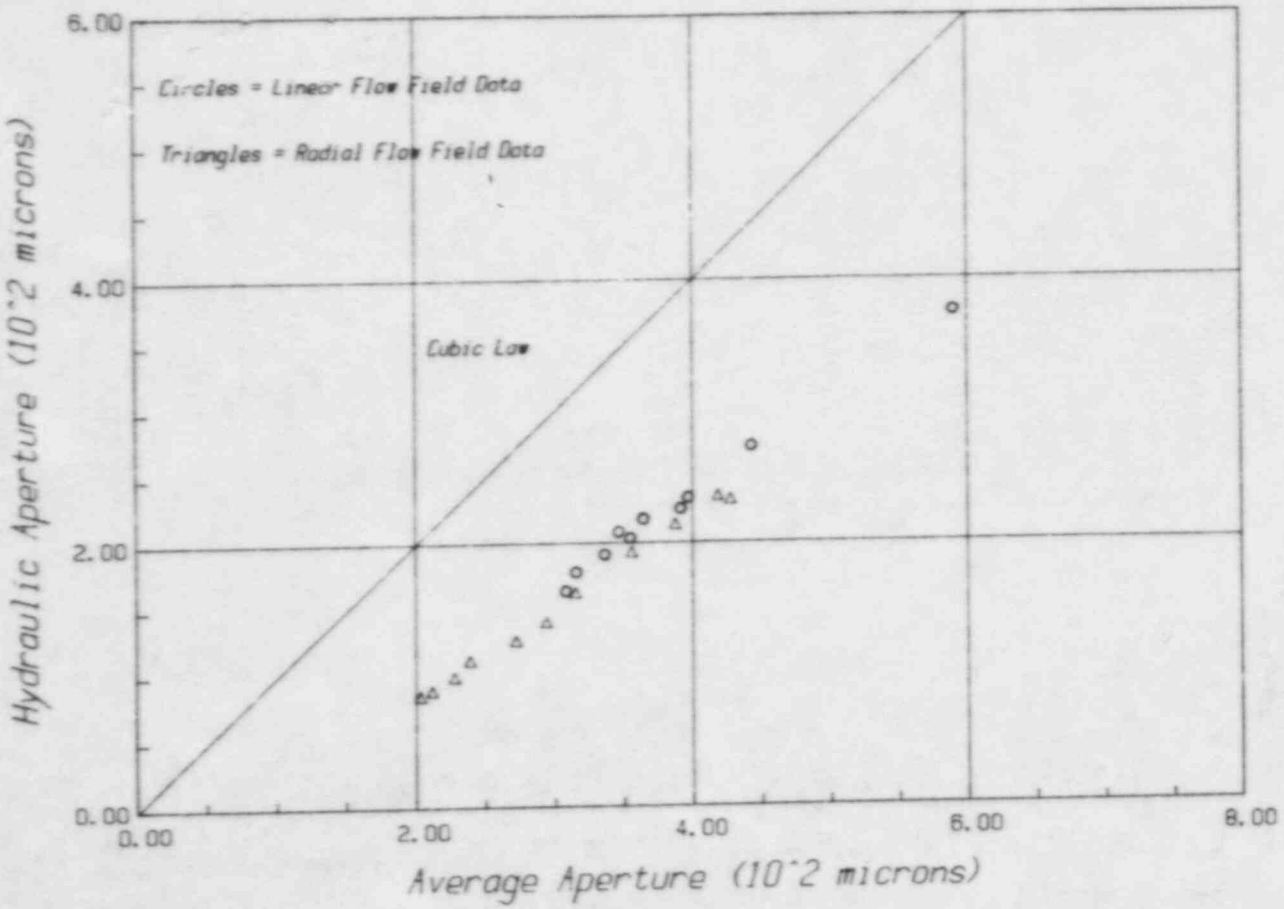

Figure 4.4. Relationship between average and hydraulic apertures.

Table 4.3. Surface Roughness Permeability Reduction Factors

Test	c*	S	λ(μm)	JRC†
Linear				
1	0.204	0.582	462	13.5
2	0.190	0.616	483	13.6
3	0.212	0.562	410	13.0
4	0.216	0.554	384	12.7
5	0.188	0.624	443	13.1
6	0.183	0.636	428	12.9
7	0.179	0.649	410	12.6
8	0.149	0.748	461	12.7
9	0.233	0.520	460	13.9
10	0.255	0.479	565	15.4
Radial*				
1	0.158	0.716	612	14.4
2	0.174	0.662	554	11.2
3	0.165	0.693	537	13.8
4	0.155	0.725	515	13.4
5	0.134	0.814	513	13.1
6	0.105	0.980	576	13.1
7	0.095	1.051	572	12.9
8	0.096	1.045	499	12.2
9	0.077	1.229	560	12.3
10	0.069	1.327	562	12.2
11	0.068	1.343	546	12.0

*Radial flow test results based on nonlinear exponent of 1.82.
†Joint roughness coefficient.

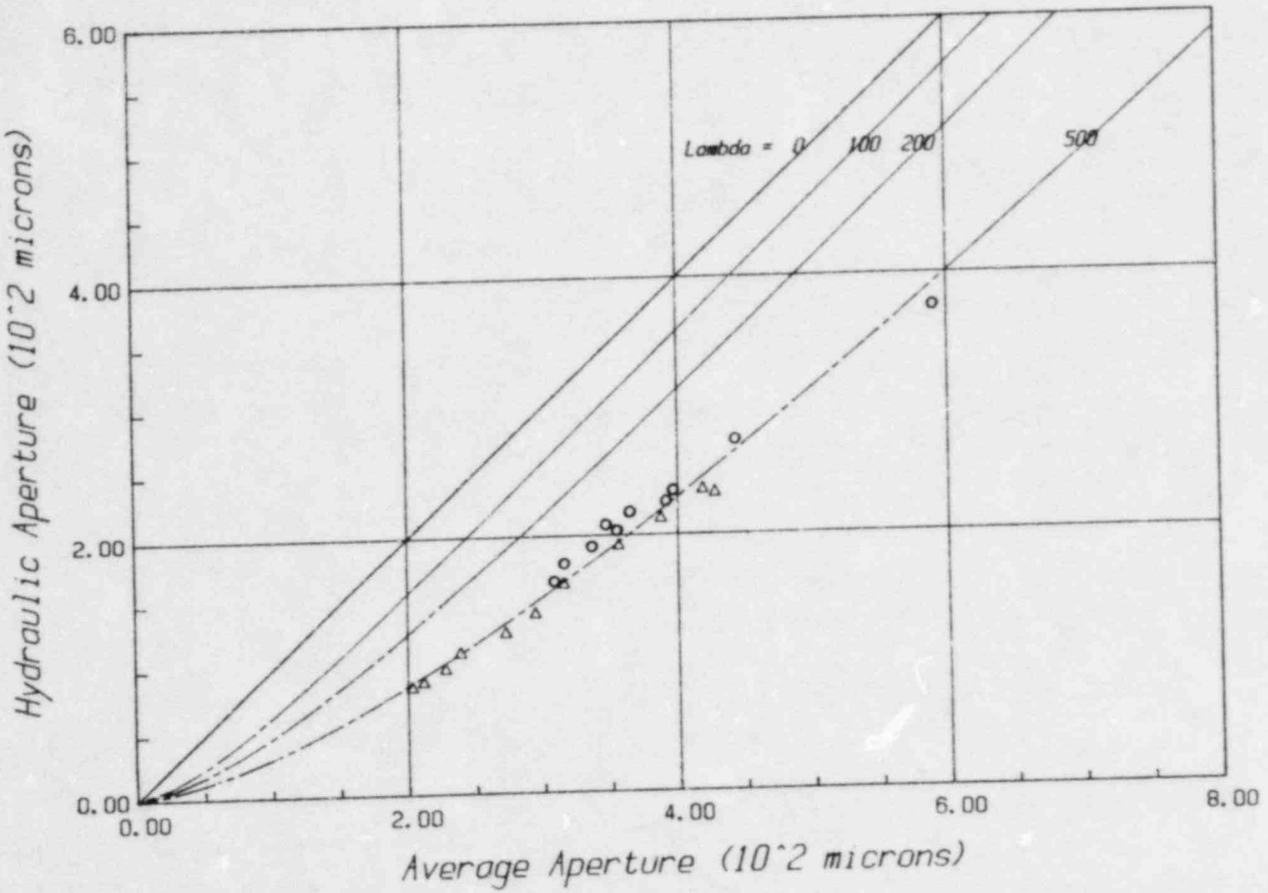

Figure 4.5. Curve fits for differing values of the parameter λ.

This corresponds to a fracture surface in which the asperities do not cross the aperture midplane. Asperities first cross the midplane at S = 0.5, which roughly corresponds to the initial contact aperture.

Equation (4.1) defines a family of curves in terms of the parameter λ for fixed $\bar{e}$. In the range of $S < 0.4$, the predicted curve parallels the cubic law such that $e_h = \bar{e}$ - a constant. Hence, for fractures in extension $\Delta e_h = \Delta \bar{e}$ and changes in flow rate can be expressed by the cubic law. This explains why the data of Sharp (1969) presented earlier appears to follow a cubic law when the initial flow rate is used as a reference. Iwai's data incorporated a similar correction term although the majority of his data was based on a fracture under compression. Based on Iwai's initial contact apertures of 50 to 100 microns, λ can be assumed to be considerably less for his tests and hence more closely aligned with the cubic law. The predicted curve for λ = 100 microns is shown in Figure 4.5 and indicates close agreement with the cubic law, particularly where a minimum flow correction term is used.

Barton (1982) has suggested that reduction of the hydraulic aperture over that of the average aperture could be estimated on the basis of the joint roughness coefficient, JRC. He proposed the empirical formula:

$$e_h = \bar{e}^2/JRC^{2.5} \qquad (4.2)$$

where e is expressed in microns.

Values of JRC as calculated from the measured values of e_h and $\bar{e}$ are also presented in Table 4.3. The computed values of JRC are seen to be reasonably constant, although a slight reduction in JRC values is noted with decreasing aperture.

The predicted relationships of e_h versus e_d as determined from equation (4.2) is shown in Figure 4.6. As seen from this figure, equation (4.2) provides a poor fit and is overly sensitive to the choice of JRC.

The λ and JRC values can be estimated independently from measurements of the surface roughness profile of the tested sample. Measurements made along a 150 mm sampling line in increments of 1.3 mm are shown in Figure 4.7. The consistent downward trend of the profile is a result of the 3° slope, as measured from the horizontal of the fracture surface. Both the λ and JRC values appear to be well predicted from the observed profile. The mean asperity height is seen to average about 500 μm, which is close to the computed λ values of 400-600 μm. Comparison of the roughness profile with the typical roughness profiles given for various values of JRC (Barton and Choubey, 1977) indicates that a JRC value of 12 to 14 yields a reasonable match. Note that the relative

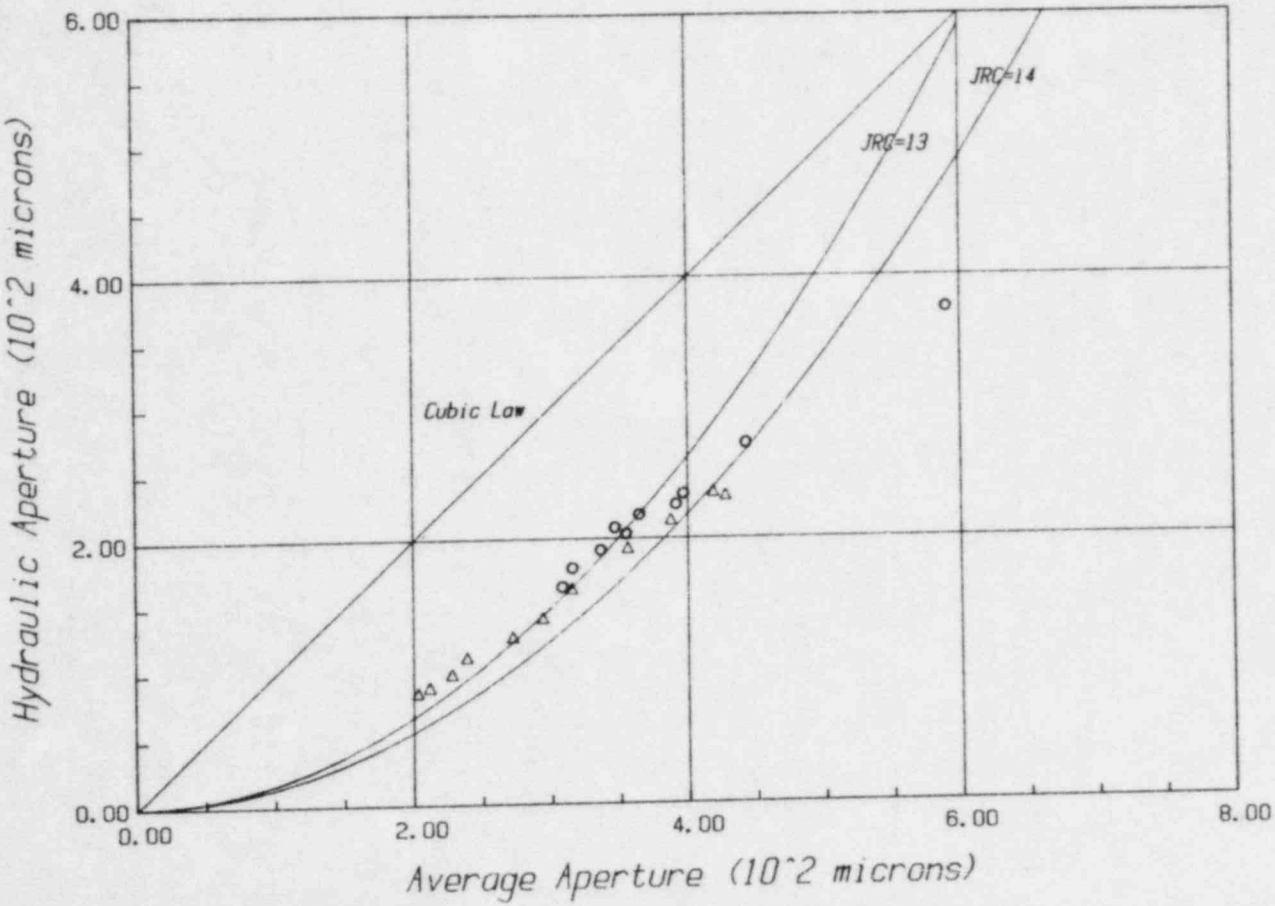

Figure 4.6. Curve fits for differing values of JRC.

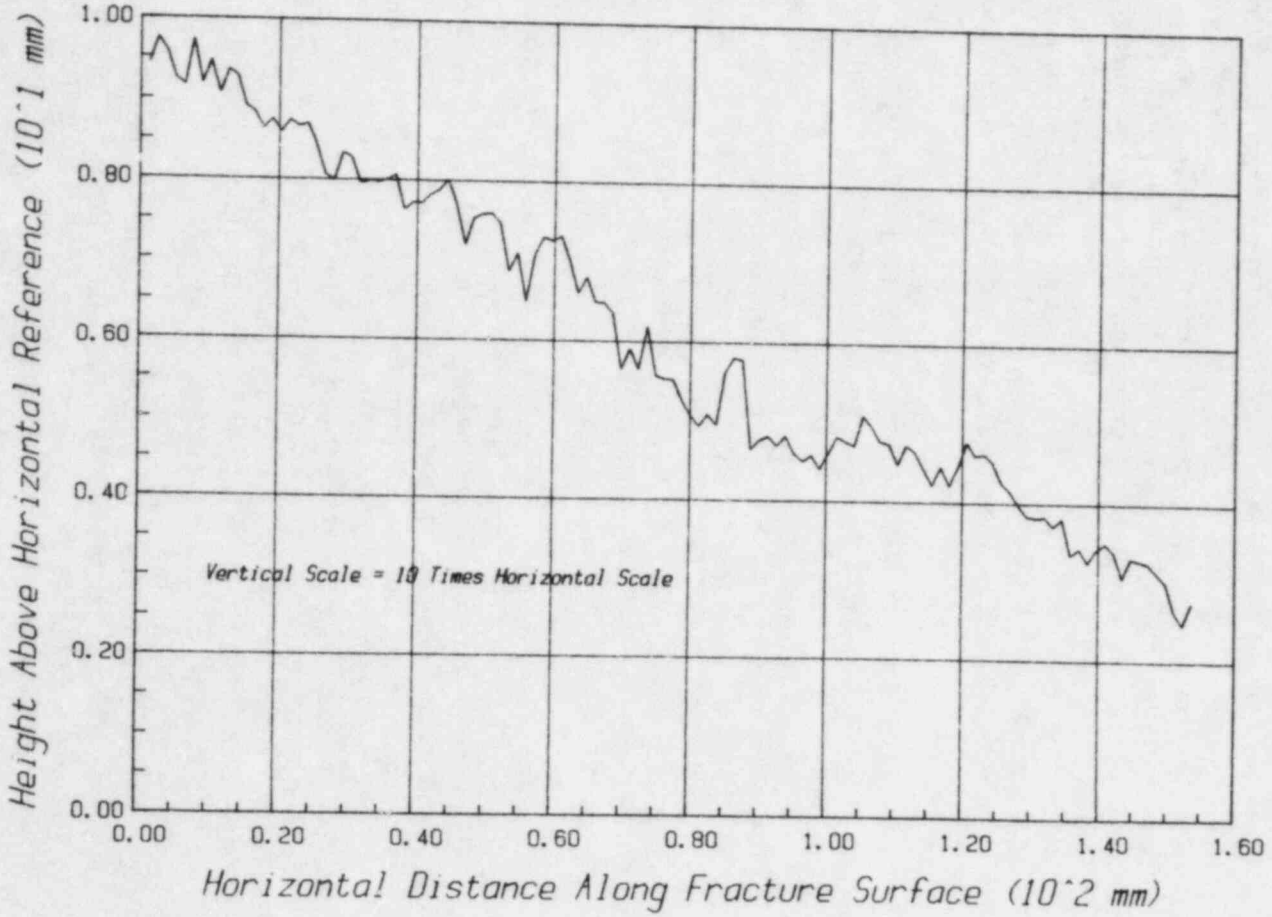

Figure 4.7. Fracture surface roughness profile.

size of the asperities when compared to the hydraulic aperture indicate that indeed the fracture is well mated.

Iwai (1971) used one-dimensional numerical simulations to examine the influence of random waviness and variability of fracture aperture along the flow path. With regards to fracture waviness where the fracture aperture is held constant, Iwai found that the permeability reduction factor varied with the maximum angularity of the flow path. Comparing his flow rate reduction with the values of c* in Table 4.2, it is found that a maximum angularity of about 60°, as measured from the horizontal, is required to produce a ç* value of 0.25. While direct comparison of Iwai's results with the test results presented here is not possible, since actual flow path deviations are two dimensional, it is noted that increases in flow path length do substantially reduce fracture permeability.

As suggested by Sharp and Maini (1972), fracture waviness may explain the discrepancy between the average and hydraulic apertures due to the effect of angularity of the fracture surface on the measurement of $\bar{e}$. Recalling the definition of average aperture as the fracture volume divided by its planar area, it is seen that $\bar{e}$ is a measure of the vertical fracture height, whereas e_h is a measure of the normal separation of the fracture surfaces. Therefore, $e_h = \cos \theta_a \bar{e}$ as shown in Figure 4.8. While the factor $\cos \theta_a$ varies over the entire fracture surface, certainly some representative angle θ_a exists which is representative of the summation.

To seek such a value, $\cos \theta_a$ and θ_a were computed from the ratio $e_h/\bar{e}$ as shown in Table 4.4. Relatively consistent values of θ_a are noted although the values show a small shift between the radial and linear flow field data and with increasing normal stress. The shift between the radial and linear values are a consequence of the slightly lower hydraulic apertures of the radial data. The shifts are within the range of experimental error but may be attributed to the effects of shear movements, as the higher values correspond to larger shear displacements. As shear improves the mating of the fracture surfaces so it increases contact area, flow constrictions, and angularity of the flow path, all of which act to reduce fracture permeability.

The angle θ_a can be computed from the surface roughness profile as the slopes between successive measurement pairs. The frequency histogram of θ_a is given in Figure 4.9. The mean value of θ_a is 9.1°, which is considerably lower than the previously computed θ_a values. Based on this average value of θ_a, no significant correction of the average aperture would be expected. Estimation of the angle θ_a is biased, however, towards lower values since the line of measurement is not generally in the direction of maximum slope. For this reason the maximum observed values of θ_a may be more representative of the true value of θ_a. Use of the maximum value of θ_a has also been suggested (Sharp

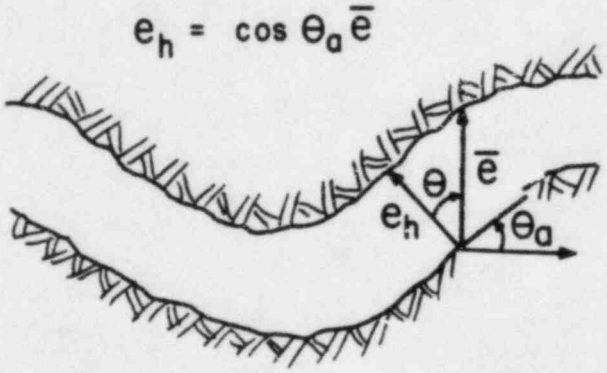

Figure 4.8. Relationship between e_h and $\bar{e}$.

Table 4.4. Surface Angularity Permeability Reduction Factors

Test	e_h (μm)	$\bar{e}$ (μm)	cos θ_a	θ_a
Linear				
1	233.4	396.7	0.588	54°
2	225.1	391.4	0.575	55°
3	217.5	364.5	0.597	53°
4	207.9	346.6	0.600	53°
5	203.1	354.9	0.572	55°
6	190.9	336.3	0.568	55°
7	177.7	315.6	0.563	56°
8	163.6	308.3	0.531	58°
9	272.2	442.7	0.616	52°
10	374.4	590.1	0.634	51°
Radial				
1	211.2	427.5	0.494	60°
2	217.9	418.6	0.521	59°
3	197.2	387.5	0.509	59°
4	176.6	356.1	0.496	60°
5	151.0	315.2	0.479	61°
6	129.4	294.1	0.440	64°
7	114.5	272.2	0.421	65°
8	98.8	238.8	0.414	66°
9	85.0	227.8	0.373	68°
10	76.1	211.7	0.359	69°
11	72.2	203.3	0.355	69°

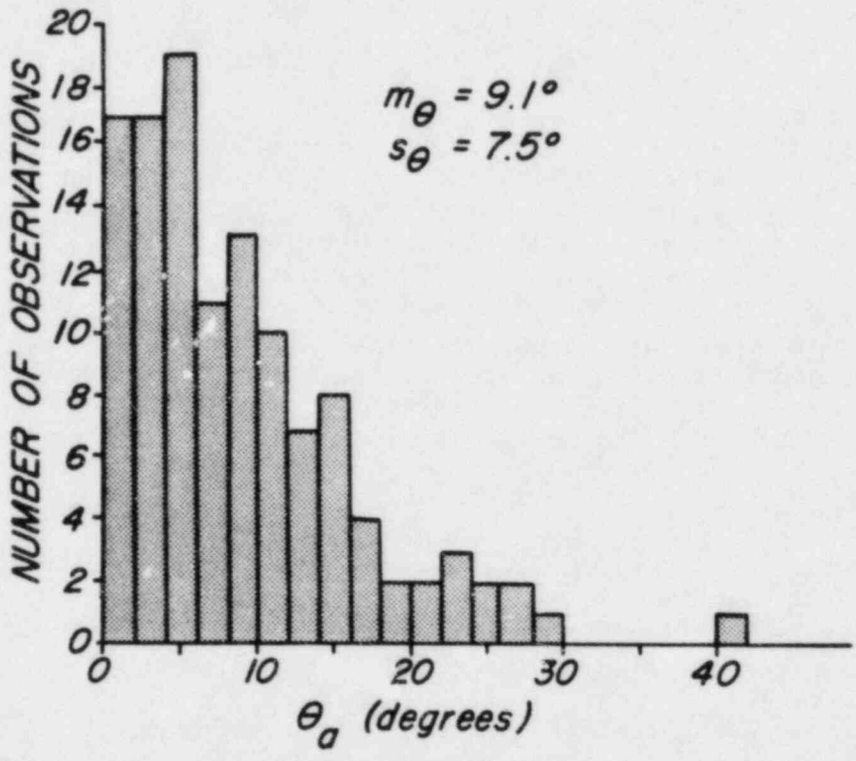

Figure 4.9. Frequency histogram of surface angularity.

and Maini, 1972) as more characteristic for a different reason, that flow is dominated by the minimum apertures encountered along the flow path.

Increase in flow path length is also seen to vary as cos θ_a, suggesting $c^* = \cos^2 \theta_a$, although here the value of cos θ_a varies with the tortuosity of the flow path which is truly three dimensional and, hence, a different value of θ_a needs to be defined. The effect is also self-cancelling to a certain degree since for certain orientations of the local surfaces the flow path width is increased. The effect of flow tortuosity is perhaps better explained by consideration of the variability of the fracture aperture.

Variability of fracture aperture may also significantly reduce flow rate as a consequence of the dominance of flow path constrictions on overall flow rate. Iwai found the permeability reduction was a function of the ratio of minimum to maximum apertures, although significant reductions (greater than 15%) were only noted for ratios of less than 0.5. Iwai's one-dimensional model probably overestimates flow restriction, however, in that two-dimensional flow permits diversion of the flow around points of constriction. Neuzil and Tracy (1981) analyzed the effect of variable fracture aperture across the flow cross section and concluded the cubic law should be modified such that:

$$e_h^3 = \int_0^\infty e^3 f(e)\, de \tag{4.3}$$

where f(e) = the normalized density distribution of e.

Equation (4.3) predicts that $e_h > \bar{e}$, for any arbitrary f(e) because the third moment about zero, e_h^3 is always greater than the cube of the first moment $\bar{e}^3$. It is readily seen that the effect of aperture variability is dependent on direction. This is analogous to comparing the equivalent conductivity of layered strata. When considering flow perpendicular to the layering, the low permeability strata dominate the equivalent conductivity. However, when considering parallel flow, the high permeability strata dominate. For this reason one-dimensional analysis is insufficient to characterize the effect of aperture variability.

The effect of contact area has also been examined by Iwai using two-dimensional numerical and laboratory studies. On the basis of these results, Iwai developed the following expression:

$$\frac{k_c}{k_o} = \frac{5}{16(A_c/A_f)+4} - \frac{1}{4} \tag{4.4}$$

where A_c = fracture contact area, A_f = total fracture area, k_c = fracture permeability with contact area, and k_o = the fracture permeability with zero contact area. Implicit in equation (4.4) is the assumption that contact area consists of small, randomly distributed areas.

Although equation (4.4) predicts large reduction in fracture perema-bility, the ratio k_c/k_o is uncorrected for the associated reduction in average aperture and hence:

$$c^*(\text{contact area}) = (1-(A_c/A_f))^{-3}\ k_c/k_o \qquad (4.5)$$

With this correction c* is found to be considerably larger than k_c/k_o and may even be greater than unity if contact area is larger than 50%.

In view of the numerous factors acting to reduce fracture conductivity, it is hardly surprising that $e_h < \bar{e}$. Of the factors considered it would appear that surface roughness and angularity are most influential. Supporting this hypothesis is the observation that significant reduction in permeability occurs even when the fracture surfaces are not in contact. Due to the complexity of the problem, analytical evaluation of the reduction factor c* is not possible in more than a qualitative sense. Of the measured fracture parameters considered, it would appear that roughness of the fracture surface, as related by a dimensionless index such as relative roughness, provides the most satisfactory means of predicting the observed reductions in fracture permeability by means of empirical equations.

The nonlinear coefficient c varies with both the mean aperture e and the nonlinear exponent n, as seen from the values listed in Tables 4.1 and 4.2. Variation with the exponent n, while not expected theoretically, can be attributed in part to differences in the curve fit of the data from which c is determined. Another possibility is that c contains geometric factors which lend it a dimensionality not accounted for. Values between test series for n = 2 do correlate well with each other as shown in Figure 4.10.

Variation of the coefficient c with aperture is attributed to increasing tortuosity of the flow path as the aperture is reduced and the fracture surfaces are better mated. Indeed the nonlinear term essentially disappears as the fracture surfaces are separated. This observation supports the previous assumption that nonlinear pressure losses occur along the flow path and are not associated with entrance and exit losses.

Louis (1969) examined fully turbulent flow as a function of surface roughness and proposed the following empirical equation:

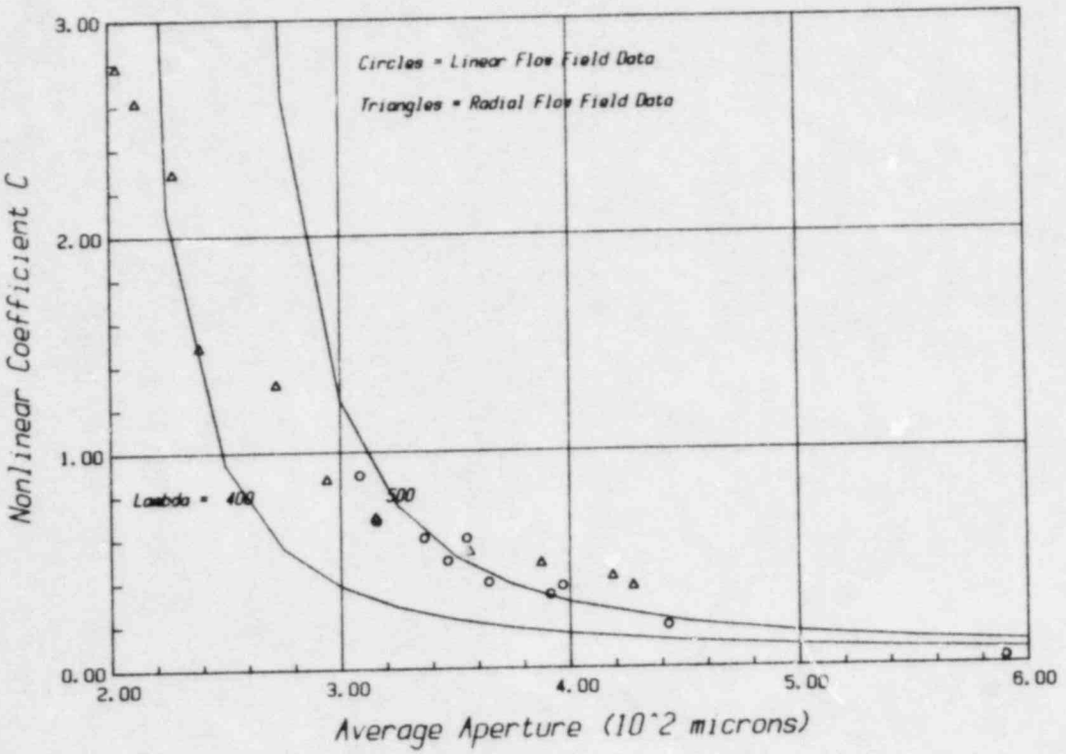

Figure 4.10. Measured and predicted values of the nonlinear coefficient C.

$$F_D = (-2 \log(S/d))^{-2} = \frac{-4e\nabla p}{\gamma v^2} \qquad (S > 0.033) \qquad (4.6)$$

where F_D = dimensionless friction factor for the characteristic length $2\bar{e}$, S = relative roughness ($\lambda/2\bar{e}$), and d = a coefficient dependent on the range of S.

The relationship between F_k, as defined by equation (2.33) or (2.37), and F_D is:

$$c = F_k = F_D/4\sqrt{12} \qquad (4.7)$$

As with equation (4.2), equation (4.6) is based on experimental data for $0.033 < S < 0.40$

To compare the measured values of the nonlinear coefficient c to those of equation (4.7) a correction must be employed to account for the use of e_h versus $\bar{e}$ in the original calculation of c. The corrected c values, computed by dividing the values in Tables 4.1 and 4.2 by c*, are listed in Table 4.5. Also shown are the values of the coefficient d, computed from equations (4.6) and (4.7) using the values of λ = 500 μm as determined from the linear coefficients. The computed values of d are seen to be reasonably constant particularly for the linear flow tests and the lower pressure gradient radial flow tests. The higher d values computed for radial flow tests number 7 through 11 are likely a consequence of the inexactness of the n = 2 fit for these tests as discussed previously. Louis (1969) gave values of the coefficient d as d = 3.7 for $S < 0.033$ and d = 1.9 for $0.033 < S < 0.4$. Hence the value of d determined here, d = 1.1 for $S > 0.4$ is reasonable.

The c values predicted by equations (4.6) and (4.7) are compared to the observed values in Figure 4.10 using d = 1.1. Despite the scatter in the measured c values, they are reasonably described by equation (4.6) for λ values of between 400 and 500. The sensitivity of the computed c values to the parameter λ is found to be far greater than for the linear coefficient 1/c*, particularly for larger values of relative roughness, and hence estimates of c from λ are less accurate.

Equations (4.2) and (4.6) are based on the same experimental data of Louis. The fact that both equations indicate good agreement with the experimental data obtained here for the same parameter suggests that extrapolation of these equations to values of S considerably greater than 0.4 is valid.

Table 4.5. Nonlinear Flow Factors

Test No.	c	d
Linear		
1	0.372	1.05
2	0.333	1.09
3	0.393	1.12
4	0.493	1.12
5	0.594	1.05
6	0.598	1.10
7	0.678	1.15
8	0.891	1.13
9	0.187	1.16
10	0.027	2.78
Radial (n = 2)		
1	0.369	0.97
2	0.414	0.97
3	0.476	1.01
4	0.534	1.07
5	0.692	1.15
6	0.871	1.18
7	1.312	1.20
8	1.485	1.35
9	2.284	1.35
10	2.612	1.43
11	2.776	1.48

Equations of identical form were developed independently by Lomize (1951), although he defined the relative roughness, Reynold's number and friction factor in a slightly different fashion. Converting Lomize's results by use of the appropriate scaling factors for comparison with equations (4.2) and (4.6) yields:

$$c^* = \frac{1}{1+17.0(S)^{1.5}} \tag{4.8}$$

$$F_D = (-0.95 - 2.56 \log(S/1.9))^{-2} \tag{4.9}$$

Differences between Lomize and Louis' results may be attributed to differences in the experimental methods used. While Lomize's results are based on roughness as created by uniform sand grains glued to a wood surface, Louis' results are obtained from measurements of flow between concrete slabs. The latter is considered a better simulation of natural fracture roughness and hence was used in this study.

Equation (4.6) is also of identical form to Nikuradse's (1930) formula for fully turbulent flow through rough pipes:

$$F_D = (-2 \log(S/d))^{-2} \tag{4.10}$$

where d = 3.7. Indeed, the form of equation (4.10) is the motivation for equation (4.6). This motivation may be misguided since nonlinear losses in fractures are only slightly comparable to turbulent losses in pipes due to differences in the scale of roughness. This may in part explain why d is not independent of S.

The results can now be summarized in terms of the dimensionless friction factor F_k and Reynold's number R_k. Using the definitions of F_k and R_k as given by (2.33) or (2.37), a universal flow law of the form of equation (2.34a) is obtained although the equation must be rewritten in the form:

$$F_k = \frac{c_1}{R_k} + c_2 \tag{4.11}$$

where c_1 and c_2 are dimensionless functions of the relative roughness, $S = \lambda/2\bar{e}$:

$$c_1 = 1 + 8.8(S)^{1.5}$$

$$c_2 = \frac{1}{4\sqrt{12}(-2 \log(S/d))^2}$$

the permeability $k = \bar{e}^2/12$

$$\text{and } d = \begin{cases} 3.7 & S < 0.33 \\ 1.9 & 0.33 < S < 0.4 \\ 1.1 & S > 0.4 \end{cases}$$

5. CONCLUSIONS AND SUMMARY

The relationship between deformation, average, and hydraulic apertures for a natural fracture has been examined experimentally in this study. Theoretical evaluations were also performed to determine the suitability of the cubic law as applied to compressible fluid flow and evaluate the effect of certain boundary conditions on observed flow rates. On the basis of these results, the following conclusions are drawn:

1. The cubic law was found to be theoretically valid for parallel plate compressible fluid flow provided the dimensionless factor $\gamma v^2/p^m$, where γ = density, v = velocity, p = absolute pressure, m = the thermodynamic coefficient = 1 for isothermal flow, is less than the desired fractional error. For nitrogen at room temperature this places an upper velocity limit of 30 m/s for a 1% error.

2. Elliptical fracture boundaries, caused by nonperpendicular intersections of test boreholes with fracture planes, increase flow rate over that of a circular boundary. The increase in flow rate, over that of a circular boundary, is equivalent to increasing the borehole radius by the factor $(1 + \cos \alpha)/2 \cos \alpha$, where α is the angular deviation of the borehole axis from the normal to the fracture plane.

3. When considering Darcian radial flow through a single principal fracture from a borehole, no significant disturbance of the steady state flow rate occurs as a result of intersecting fractures when the ratio of the intersecting to principal fracture apertures is less than 1/2. Thereafter, flow rate is increased appreciably. For ratios greater than 2, the intersecting fracture may be treated as a constant ambient pressure boundary. As radial distance to the fracture from the borehole increases, disturbance of the flow rate decreases hyperbolically. However, even at radial distances of 20 borehole radii, increases in flow rate of up to 30% were noted.

4. The mean or average fracture aperture decreases at a lesser rate than the observed fracture deformation upon normal loading of a fracture unless the observed deformation is accommodated by improved mating of the fracture surfaces via shear displacement. For the sample tested the average and deformation apertures were found to be nearly identical even when shear movement was restricted, although considerably greater fracture deformation occurred at similar stress levels when shear movement was unrestricted.

5. Following separation of the fracture surfaces, the initial contact aperture, as measured at the smallest applied stress of 0.03 MPa, was found to be nearly constant and close to the mean asperity height. After load cycling, however, considerable residual fracture

deformation was noted indicating improved mating of the fracture surfaces.

6. Nonlinear flow conditions were observed for all flow tests conducted and found to be well described by an equation of the form $-dp/dx = av + bv^n$ with $n \cong 2$. This indicates a smooth transition from linear laminar to fully turbulent flow regimes.

7. The linear conductivity of the fracture tested was found to be well below that predicted by the cubic law using the average fracture aperture. The observed difference was attributable to surface roughness and was well described by empirical equations in terms of the relative roughness, defined as the mean asperity height divided by the mean aperture. These equations were found to be valid even when applied to relative roughness as large as 1.4, despite the fact that the empirical equations were based on relative roughnesses of less than 0.4.

8. The nonlinear coefficient cb was also found to be reasonably described by similar empirical equations, although here again the relative roughness values were greater than the assumed range of validity. The magnitude of the nonlinear term was found to increase with decreasing aperture and may be related to the degree of fracture mating in addition to the magnitude of surface roughness.

Although the cubic law was found not to be strictly valid for fluid flow through a rough fracture, it is of note that as the relative roughness decreases the difference between the hydraulic and deformation aperture approaches a constant; hence, the cubic law may be approximately valid for predicting changes in fracture conductivity if the range of apertures considered is reasonably moderate. Considering the relative dominance of the nonlinear term as relative roughness increases, the cubic law may be inconsequential in terms of predicting flow rate for very rough fractures.

The ability to predict both the nonlinear and linear coefficients provides a means of determining both the mean aperture and the relative roughness in test situations where neither can be measured directly. This results from the fact that two independent equations exist in the linear and nonlinear coefficients respectively, and these are a function of only two unknowns. Implicit in this approach, however, is the assumption that sufficient nonlinearity exists such that the nonlinear coefficient equation is sensitive to the relative roughness parameter. It is believed, however, that this will almost always be the case.

6. LIST OF SYMBOLS

6.1 English Letters

a, b	linear and nonlinear coefficients, respectively, of nonlinear pressure-mass flow rate equations described by fluid properties and flow geometry
a_ℓ, b_ℓ	a and b coefficients for linear flow field
a_r, b_r	a and b coefficients for radial flow field
A_f	fracture area (planar extent of surface)
c	dimensionless nonlinear coefficient of nonlinear pressure-mass flow rate equations
c*	intrinsic fracture permeability reduction coefficient
d	coefficient in nonlinear friction factor equation
e	parallel plate aperture
$\bar{e}$	arithmetic average fracture aperture (see Glossary)
e_d	fracture deformation aperture (see Glossary
e_h	hydraulic fracture aperture (see Glossary)
E_v	average volumetric aperture (experimental measure of e)
E_d	fracture deformation aperture (experimental measure of e_d)
F_D	dimensionless friction factor for characteristic length of 2e
F_k	dimensionless friction factor for characteristic length of $k_f^{1/2}$
g	gravitational acceleration
h	hydraulic head
i	hydraulic gradient, ∇h
JRC	joint roughness coefficient
k	intrinsic permeability

k_c	intrinsic fracture permeability with contact area between fracture surfaces
k_f	intrinsic fracture permeability
k_o	intrinsic fracture permeability with zero contact area between fracture surfaces
K	bulk fluid viscosity
L	linear flow field flow path length
m	thermodynamic exponent relating density to pressure ($\gamma = \gamma_o p^m$)
M	molecular weight of gas
n	nonlinear exponent of nonlinear pressure-mass flow rate equations
N	number of moles of gas
p_e	gage pressure
Pa	atmospheric pressure
Pe	absolute exhaust pressure
Pi	absolute injection pressure
Pm	measured absolute pressure
q	volumetric flow rate per unit width of flow cross-section
q_a	adiabatic mass flow rate per unit width of flow cross-section
q_i	isothermal mass flow rate per unit width of flow cross-section
q_m	mass flow rate per unit width of flow cross-section
Q_1	downstream nodal outflow
Q_2	nodal flow withdrawal
Q_i	upstream nodal inflow
Q_m	total mass flow rate
r_1	inner radius of radial flow field

r_2	outer radius of radial flow field
R	universal ideal gas constant
R_e	Reynold's number with characteristic length 2e
R_k	Reynold's number with characteristic length $k^{1/2}$
S	surface roughness index
T	absolute temperature
v, v_{avg}	average fluid velocity between fracture walls
v_m	mass flux
v_x	local fluid velocity in x-direction
v_y	local fluid velocity in y-direction
V_f	fracture volume

6.2 Greek Letters

α, β	substitution constants used to simplify pressure distribution expressions for liner and radial flow fields
γ	fluid density
γ_a	γ_o for adiabatic flow
γ_i	γ_o for isothermal flow
γ_o	constant of proportionality between density and pressure ($\gamma = \gamma_o p^m$)
λ	mean asperity height
μ	fluid viscosity
θ	angle between normal to fracture plane and borehole axis
θ_a	angular deviation of fracture surface from planar trend

7. GLOSSARY OF SELECTED TERMS

average aperture	the arithmetic mean separation of opposing fracture surfaces as measured normal to the planar trend of the fracture surface
aperture deformation	relative closure of opposing fracture surfaces under normal stress measured as the portion of total sample strain not attributable to intact rock strain
deformation aperture	a fracture's aperture as computed from the observed aperture deformation relative to some initial reference aperture
fracture conductivity	ratio of pressure gradient to fluid velocity. Under nonlinear flow conditions this refers to the linear component of flow (coefficient of linear term) or linear conductivity.
hydraulic aperture	the equivalent parallel plate aperture as computed from the fracture conductivity assuming validity of the cubic law
initial contact aperture	the average fracture aperture at some initial small applied normal stress sufficient to seat the opposing fracture surfaces. In the tests conducted here the initial normal stress was 0.03 MPa.
intrinsic permeability	the portion of the fracture conductivity which is independent of the fluid properties and flow boundary conditions. In flow between parallel plates, the intrinsic permeability is $e^2/12$.
linear (or Darcian) flow	flow in which the pressure gradient is linearly porportional to velocity.
linear flow field	flow between parallel and straight constant pressure boundaries where the flow paths are parallel lines. The flow may be linear, nonlinear, or fully turbulent.
radial flow field	flow between concentric circular constant pressure boundaries where the flow paths are radial straight lines perpendicular to the circular boundaries.

8. REFERENCES CITED

Arbhabhirama, A. and Dinoy, A. A., "Friction Factor and Reynolds Number in Porous Media Flow." Journal of the Hydraulics Division, Proceedings of A.S.C.E., Vol. 99, No. HY6, June, 1973.

Baker, W. J., "Flow in Fissured Formations." 4th World Petroleum Congress, Section II, Paper 7, Rome, 1955.

Barton, N., Modelling Rock Joint Behavior from In Situ Block Tests: Implications for Nuclear Waste Repository Design. ONWI Technical Report ONWI-308, September, 1982.

Barton, N. and Choubey, V., "The Shear Strength of Rock and Rock Joints in Theory and Practice." Rock Mechanics, Vol. 10, 1977.

Bourke, P. J., Bromley, A., Rae, J., and Sincock, K., "A Multi-Packer Technique for Investigating Resistance to Flow through Fractured Rock and Illustrative Results." NEA Workshop on Siting of Radioactive Waste Repositores, Paper for Session 3, Paris, May, 1980.

Engelder, T. and Scholz, C. H., "Fluid Flow Along Very Smooth Joints at Effective Pressures up to 200 Megapascals." In Mechanical Behavior of Crustal Rocks, edited by N. L. Carter, Geophysics Monograph 24, American Geophysical Union, 1981.

Hardin, E., Barton, N., Lingle, D., Board, M., and Voegele, M., A Heated, Flatjack Test Series to Measure the Thermomechanical and Transport Properties of In Situ Rock Masses (Heated Block Test), ONWI Technical Report ONWI-260, September, 1982.

Huitt, J. L., "Fluid Flow in Simulated Fractures." American Institute of Chemical Engineers Journal, Vol. 2, No. 2,

Iawi, K., Fundamental Studies of Fluid Flow through a Single Fracture. Ph.D. Dissertation, University of California, Berkeley, 1976.

Kirkham, D., "Field Method for Determination of Air Permeability of Soil in Its Undisturbed State." Proc. Soil Sci. Soc. America, Vol. 11, 1946.

Kranz, R. L., Frankel, A. D., Engelder, T., and Scholz, C. H., "The Permeability of Whole and Jointed Barre Granite." Int. J. Rock Mech. Min. Sci. and Geomech. Abstr., Vol. 16, 1979.

Lomize, G. M., "Filtratsiia v Treshehinovatykh Porod" (Water Flow in Jointed Rock), Gosenergoizdat, Moscow, 1951.

Louis, C., A Study of Groundwater Flow in Jointed Rock and Its Influence on the Stability of Rock Masses. Rock Mechanics Research Report No. 10, Imperial College, London, England, 1969.

Louis, C. and Maini, Y. N., "Determination of In Situ Hydraulic Parameters in Jointed Rock." Proc. 2nd Cong. Int. Soc. Rock Mech., Belgrade, Vol. 1, 1970.

Maini, Y. N. T., In Situ Hydraulic Parameters in Jointed Rock; Their Measurement and Interpretation. Ph.D. Dissertation, Imperial College, London, England, 1971.

Muskat, M., The Flow of Homogeneous Fluids through Porous Media. J. W. Edwards Inc., Ann Arbor, Michigan, 1946.

Neuzil, C. E. and Tracy, J. V., "Flow through Fractures." Water Resources Research, Vol. 17, No. 1, February, 1981.

Nikuradse, J., "Stromungsgesetze in ranhen Rohren." VOI-Forschungsheft, 361, 1933.

Pratt, H. R., Swolfs, H. S., Brace W. F., Black, A. D. and Handin, J. W., "Elastic and Transport Properties of an In Situ Jointed Granite". Int. J. Rock Mech. Min. Sci. and Geomech. Abstr., Vol. 14, 1977.

Prickett, T. A. and Lonnquist, C. G., Selected Digital Computer Techniques for Groundwater Resource Evaluation. Bulletin 55, Illinois State Water Survey, Urbana, 1971.

Rissler, P., "Determination of the Water Permeability of Jointed Rock." English Edition of Vol. 5, Publication for the Institute for Foundation Engineering Mechanics, Rock Mechanics and Water Ways Construction, RWU Aachen, Federal Republic of Germany, 1978.

Romm, E. S., Fluid Flow in Fractured Rocks. Nedra Publishing Company, Moscow, 1966.

Sharp, J. C., Fluid Flow through Fissured Media, Ph.D. Dissertation, Imperial College, London, England, 1970.

Sharp, J. C. and Maini, Y. N. T., "Fundamental Considerations on the Hydraulic Characteristics of Joints in Rock." Proc. Symp. on Percolation through Fissured Rock, Int. Soc. Rock Mech., Stuttgart, 1972.

Wang, J. S. Y., Narasimhan, T. N., Tsang, C. F. and Witherspoon, P. A., "Transient Flow in Tight Fractures." Proc. Int. Well Testing Symposium, Berkeley, CA, October, 1977.

Ward, J. C., "Turbulent Flow in Porous Media". Journal of the Hydraulics Division, Proceedings of the American Society of Civil Engineers, Vol. 90, No. HY5, September, 1964.

Wilson, C. R. and Witherspoon, P. A., An Investigation of Laminar Flow in Fractured Porous Rocks. University of California Rept. No. 70-6, Berkeley, CA, November, 1970.

APPENDIX A

SUMMARY OF FINITE DIFFERENCE MODEL RESULTS

Table A.1. Determination of the Effect of Single Intersecting Fracture*

Principal Aperture (μm)	Intersecting Aperture (μm)	Distance to Fracture Divided by Well Radius	Steady State Flow Rate 10^4(sccm)†	Equivalent Radius Ratio (r_2/r_1)
200	0	no intersecting fracture	1.610	111
200	200	2	2.544	19.7
200	200	5	2.197	31.5
200	200	10	2.006	43.7
200	200	20	1.849	60.3
200	200	50	1.694	87.7
200	100	2	1.774	71.7
200	100	5	1.737	78.5
200	100	10	1.706	85.0
200	100	20	1.665	94.8
200	400	2	4.488	5.4
200	400	5	2.981	12.7
200	400	10	2.414	23.1
200	400	20	2.044	40.8
200	10^6	2	5.747	3.7
200	10^6	5	3.322	9.8
200	10^6	10	2.560	19.3
200	10^6	20	2.104	36.7
200	10^6	50	1.750	76.0

* Injection Pressure = 110 kPa for all runs.
† Model Flow Rate = 1/2 total well flow rate.

APPENDIX B

FRACTURE POROSITY TEST DATA

Table B.1. Porosity Test No. 1*

Fracture Volume (cm^3)	Average Aperture (μm)	Deformation Aperture (μm)	Normal Stress (MPa)
46.5	648.9	625.5	0
44.2	617.6	632.5	0
44.3	618.6	626.9	0
20.3	284.1	440.2	0.8
15.6	217.3	439.8	0.8
30.9	432.0	439.6	0.8
28.6	399.2	413.6	1.7
30.9	431.3	413.5	1.7
31.9	446.1	413.5	1.7
26.5	369.5	413.0	1.7
28.8	402.3	392.5	3.5
28.6	399.8	392.4	3.5
27.5	384.3	392.0	3.5
27.5	384.8	390.1	3.5
26.3	368.0	366.0	6.8
24.3	339.5	365.7	6.8
26.8	374.9	364.3	6.8
25.2	352.1	364.3	6.8
26.4	368.3	345.3	10.3
23.5	328.4	344.7	10.3
24.8	346.4	344.6	10.3
23.4	327.4	344.4	10.3
24.8	346.4	328.7	13.8
23.3	325.8	330.0	13.7
25.1	350.3	328.4	13.7
22.0	307.7	329.1	13.7
23.8	332.4	317.1	17.0
21.9	306.0	317.8	17.0
23.5	328.6	316.8	17.0
21.8	304.9	318.1	17.0
23.8	331.9	309.5	20.0
22.6	316.3	309.2	20.0
23.9	333.5	310.6	20.0
23.2	324.6	308.9	20.0
23.8	332.4	307.7	17.3

Table B.1--continued

Fracture Volume (cm^3)	Average Aperture (μm)	Deformation Aperture (μm)	Normal Stress (MPa)
21.7	303.0	308.5	17.3
23.8	331.9	308.4	17.3
22.5	313.6	310.1	17.3
23.4	327.5	309.1	13.9
22.5	314.5	309.2	13.9
22.8	318.7	309.2	13.9
24.3	339.1	312.0	10.5
23.6	329.3	311.7	10.5
24.2	337.4	311.9	10.5
22.8	318.9	312.5	10.5
24.4	341.4	316.6	7.1
22.9	320.0	316.1	7.1
24.0	335.2	316.4	7.1
24.3	339.0	316.8	7.1
25.9	361.2	323.3	3.8
23.0	321.6	322.6	3.8
25.2	352.1	323.6	3.8
24.0	335.5	323.6	3.8
28.5	397.7	352.7	0
24.9	347.1	352.6	0
27.2	379.9	354.5	0
26.2	365.8	353.8	0

* Pycnometer Volume = 53.7 cm^3, Dead Space Volume = 29.7 cm^3, Fracture Area = 716 cm^2

Table B.2. Porosity Test No. 2*

Fracture Volume (cm^3)	Average Aperture (μm)	Deformation Aperture (μm)	Normal Stress (MPa)
70.9	989.9	1000.8	0
71.2	994.8	1004.5	0
70.5	984.1	1001.7	0
72.3	1010.3	998.3	0
32.6	455.1	463.3	0.1
33.9	474.0	462.5	0.1
33.5	468.3	462.3	0.1
33.6	469.8	461.3	0.1
30.1	421.0	421.5	0.8
30.9	431.0	420.8	0.8
30.9	432.0	420.6	0.8
30.9	431.0	420.4	0.8
29.5	412.4	402.5	1.5
29.7	414.3	401.8	1.5
29.7	415.3	401.5	1.5
29.6	412.8	401.3	1.5
27.2	379.3	370.4	3.5
27.5	383.7	369.6	3.5
27.3	381.6	369.3	3.4
27.3	381.6	369.0	3.4
25.4	354.3	342.2	7.0
25.4	354.4	341.2	7.0
25.3	353.6	341.1	7.0
25.2	351.3	340.9	7.0
24.6	343.3	326.3	10.3
24.3	338.9	325.7	10.3
23.9	333.8	325.3	10.2
24.0	334.5	325.3	10.2
23.5	328.0	315.7	13.6
23.6	329.5	314.2	13.6
23.2	324.5	313.8	13.5
23.4	326.6	313.8	13.5
22.7	316.7	305.9	17.1
22.9	319.5	304.8	17.0

Table B.2--continued

Fracture Volume (cm^3)	Average Aperture (μm)	Deformation Aperture (μm)	Normal Stress (MPa)
22.9	319.5	304.6	16.9
23.0	320.9	304.3	16.9
26.8	374.0	349.5	0.1
27.0	377.7	350.1	0.1
25.8	360.3	350.9	0.1
26.8	373.8	350.9	0.1
48.5	677.0	599.7	0
48.3	674.0	601.1	0
48.1	671.6	598.4	0
48.2	673.6	599.9	0

* Pycnometer Volume = 53.6 cm^3, Dead Space Volume = 29.7 cm^3, Fracture Area = 716 cm^2.

Table B.3. Linear Flow Field Test-Fracture Porosity Data*

Test No.	Fracture Volume (cm^3)	Average Aperture (μm)	Deformation Aperture (μm)	Normal Stress (MPa)
1-initial	31.8	443.9	450.7	0
	32.5	453.7	450.2	0
	32.5	453.7	451.0	0
1-final	26.7	373.4	398.0	0
	27.4	383.0	397.5	0
	28.1	392.4	397.2	0
2-initial	26.0	363.6	394.7	0
	27.4	382.0	394.2	0
	27.7	386.4	394.1	0
	26.7	373.2	393.8	0
	26.6	371.0	393.8	0
	26.7	373.2	393.6	0
2-final	27.5	384.4	390.2	0
	28.0	391.4	389.9	0
	26.9	376.3	389.8	0
3-initial	27.1	378.6	367.1	0.3
	26.1	365.0	367.0	0.3
	26.4	369.0	366.3	0.3
3-final	23.2	324.1	363.2	0.3
	27.2	379.3	362.8	0.3
	26.5	369.7	363.4	0.3
4-initial	23.6	329.1	348.2	1.4
	22.4	313.0	348.5	1.4
	24.9	347.4	348.5	1.4
4-final	20.7	289.0	346.4	1.4
	26.0	363.7	346.4	1.4
	24.5	341.9	346.3	1.4
5-initial	24.7	345.0	357.2	2.1
	25.3	353.8	356.7	2.1
	25.9	361.3	356.5	2.1
5-final	21.9	305.5	352.5	2.0
	24.1	336.4	352.3	2.0
	24.1	336.4	352.3	2.0

Table B.3--continued

Test No.	Fracture Volume (cm^3)	Average Aperture (μm)	Deformation Aperture (μm)	Normal Stress (MPa)
6-initial	24.8	346.4	338.8	3.5
	23.9	333.8	338.6	3.5
	24.0	335.0	338.4	3.4
6-final	24.3	340.0	333.6	3.4
	22.5	314.9	333.6	3.4
	22.1	308.6	333.3	3.4
7-initial	22.4	312.9	318.4	7.0
	22.9	320.2	318.0	7.0
	22.6	316.2	318.0	7.0
7-final	24.9	348.0	314.0	6.9
	23.5	328.6	314.0	6.9
	22.9	319.2	313.9	6.9
8-initial	22.3	311.7	314.1	14.5
	20.8	290.4	313.8	14.5
	21.2	296.2	313.5	14.5
8-final	21.4	298.4	305.2	13.9
	21.0	293.8	305.2	13.9
	20.3	283.4	305.2	13.9
9-initial	43.2	603.6	496.9	0
	42.4	592.8	503.7	0
	42.9	598.9	503.5	0
9-final	40.5	566..	484.6	0
	40.4	564.7	485.4	0
	40.2	562.0	483.9	0
10-initial	72.3	1010.1	744.8	0
	71.9	1004.0	741.3	0
	70.7	987.3	751.8	0
10-final	65.7	917.4	722.5	0
	66.6	930.2	728.8	0
	67.0	936.1	729.6	0

Table B.3--continued

Test No.	Fracture Volume (cm^3)	Average Aperture (μm)	Deformation Aperture (μm)	Normal Stress (MPa)
Prior to	54.4	760.4	762.6	0
Radial	54.6	762.5	765.7	0
Changeover	53.8	751.0	759.6	0
	55.3	773.0	770.5	0
	55.3	772.5	777.3	0
	52.7	735.3	771.1	0

* Pycnometer Volume = 53.6 cm^3, Dead Space Volume = 272.3 cm^3, Fracture Area = 716 cm^2

APPENDIX C

FRACTURE FLOW TEST DATA

Table C.1. Linear Flow Field Test*

Test No.	Atmospheric Pressure (kPa)	$p_i^2-p_e^2$ (10^8 Pa^2)†	Mass Flow Rate (10^{-4} kg/s)	Deformation Aperture (μm)	Normal Stress (MPa)
1	92.36	6.262	1.466	396.3	0
		10.23	2.058	396.1	0
		7.954	1.750	396.0	0
		5.060	1.251	396.8	0
		1.895	0.5838	397.5	0
		0.7034	0.2670	397.6	0
2	92.68	10.71	2.087	392.3	0
		9.264	1.889	392.4	0
		7.826	1.682	392.1	0
		6.418	1.460	392.2	0
		5.326	1.264	391.7	0
		4.164	1.049	391.0	0
		3.067	0.8162	391.0	0
		2.220	0.6251	391.0	0
		1.415	0.4231	390.3	0
		0.6500	0.2013	390.2	0
3	91.82	13.25	2.062	365.4	0.3
		11.55	1.875	365.0	0.3
		9.587	1.657	365.5	0.3
		8.139	1.473	365.2	0.3
		6.474	1.256	364.3	0.3
		4.956	1.028	364.0	0.3
		3.713	0.8162	363.9	0.3
		2.628	0.6280	363.3	0.3
		1.624	0.4202	363.5	0.3
		0.7362	0.2053	364.6	0.3
4	91.80	17.37	2.061	348.0	1.4
		14.69	1.859	346.7	1.4
		12.57	1.675	346.9	1.4
		10.23	1.456	346.6	1.4
		8.195	1.252	346.7	1.4
		6.434	1.046	346.2	1.4
		4.577	0.8235	346.2	1.4
		3.225	0.6297	346.7	1.4
		0.8651	0.2189	346.1	1.4
		0.5885	0.1538	346.7	1.4
		0.3124	0.1113	346.4	1.4

Table C.1--continued

Test No.	Atmospheric Pressure (kPa)	$P_i^2-P_e^2$ (10^8 Pa^2)†	Mass Flow Rate (10^{-4} kg/s)	Deformation Aperture (μm)	Normal Stress (MPa)
5	92.18	19.31	2.089	356.4	2.1
		16.41	1.874	355.5	2.0
		13.75	1.677	355.3	2.0
		11.34	1.472	355.8	2.0
		9.099	1.264	355.7	2.0
		7.073	1.056	355.5	2.0
		4.975	8.183	355.5	2.0
		3.388	6.165	355.3	2.0
		2.133	4.294	355.1	2.0
		1.091	2.180	354.0	2.0
		0.7761	1.627	353.5	2.0
		0.4800	1.054	353.2	2.0
		0.2214	0.4471	353.0	2.0
6	92.07	22.71	2.072	338.2	3.4
		19.90	1.895	338.0	3.4
		16.58	1.682	337.7	3.4
		13.26	1.450	337.5	3.4
		10.63	1.246	336.8	3.4
		8.064	1.023	336.5	3.4
		6.224	0.8460	336.4	3.4
		4.288	0.6411	336.1	3.4
		2.392	0.4052	335.9	3.4
		1.108	0.2126	335.3	3.4
		0.7937	0.1507	334.8	3.4
		0.4979	0.1016	334.6	3.4
		0.2764	0.0469	334.0	3.4
7	92.02	30.01	2.070	317.9	7.0
		25.68	1.875	317.2	6.9
		21.66	1.681	317.0	6.9
		17.29	1.451	316.7	6.9
		14.13	1.264	316.4	6.9
		10.89	1.058	316.2	6.9
		7.945	0.8429	315.4	6.9

Table C.1--continued

Test No.	Atmospheric Pressure (kPa)	$p_i^2-p_e^2$ (10^8 Pa^2)	Mass Flow Rate (10^{-4} kg/s)	Deformation Aperture (μm)	Normal Stress (MPa)
		5.516	0.6420	315.2	6.9
		3.139	0.4139	315.3	6.9
		1.367	0.2136	314.7	6.9
		1.349	0.2086	314.5	6.9
		0.9042	0.1631	314.5	6.9
		0.5715	0.1177	314.0	6.9
		0.1657	0.04856	314.1	6.9
8	92.48	40.86	2.076	312.5	14.4
		34.55	1.869	310.3	14.2
		28.56	1.667	309.9	14.1
		23.11	1.452	309.4	14.1
		18.98	1.270	309.2	14.0
		14.61	1.057	308.5	14.0
		10.42	0.8446	308.2	14.0
		7.115	0.6299	308.0	14.0
		4.099	0.4139	307.6	14.0
		1.841	0.2159	307.2	14.0
		1.710	0.2049	306.9	14.0
		1.356	0.1606	306.5	14.0
		0.8901	0.1075	306.2	14.0
		0.5001	0.05590	305.9	13.9
9	92.30	5.152	2.089	450.8	0
		4.621	1.892	448.4	0
		3.940	1.666	443.3	0
		3.374	1.476	443.0	0
		2.660	1.259	442.2	0
		2.136	1.027	441.5	0
		1.651	0.8333	440.6	0
		1.241	0.6453	439.9	0
		0.7771	0.4310	439.0	0
		0.3326	0.2249	438.4	0
10	92.21	1.482	2.073	607.6	0
		1.277	1.880	600.2	0
		1.147	1.682	595.7	0
		0.9802	1.470	591.7	0
		0.7949	1.242	588.8	0

Table C.1--continued

Test No.	Atmospheric Pressure (kPa)	$P_i^2-P_e^2$ (10^8 Pa^2)†	Mass Flow Rate (10^{-4} kg/s)	Deformation Aperture (μm)	Normal Stress (MPa)
		0.6282	1.036	587.4	0
		0.5357	0.8273	584.3	0
		0.3877	0.6140	583.1	0
		0.2953	0.4200	581.9	0
		0.1661	0.2105	580.6	0

* Flow Path Width = 0.282 m, Flow Path Length = 0.254 m
† P_i = injection pressure; P_e = exhaust pressure (absolute pressures)

Table C.2. Radial Flow Field Test*

Test No.	Atmospheric Pressure (kPa)	$P_i^2-P_e^2$ (10^8 Pa^2)†	Mass Flow Rate (10^{-4} kg/s)	Deformation Aperture (μm)	Normal Stress (MPa)
1	92.21	6.469	2.100	424.1	0
		5.059	1.882	423.8	0
		4.110	1.667	424.1	0
		3.425	1.460	423.8	0
		2.665	1.253	423.3	0
		2.267	1.044	427.6	0
		1.832	0.8478	432.3	0
		1.270	0.6269	434.9	0
		0.7383	0.4286	434.5	0
		0.2475	0.2169	429.3	0
		0.02041	0.1566	427.3	0
		-0.414	0.09073	425.5	0
2	92.21	6.292	2.100	417.9	0
		5.016	1.869	417.9	0
		4.305	1.657	418.1	0
		3.522	1.471	418.1	0
		2.861	1.249	418.4	0
		2.216	1.049	418.6	0
		1.638	0.8432	419.0	0
		1.167	0.6207	419.1	0
		0.7273	0.4311	419.5	0
		0.2631	0.2093	419.8	0
3	92.44	8.658	2.077	393.6	0
		7.117	1.865	392.0	0
		5.852	1.662	390.1	0
		4.857	1.449	389.0	0
		4.000	1.257	387.7	0
		3.119	1.049	386.3	0
		2.318	0.8464	385.4	0
		1.585	0.6333	384.9	0
		0.9250	0.4087	383.7	0
		0.3645	0.2140	382.6	0
4	92.38	12.02	2.076	358.4	0.1
		10.32	1.863	356.5	0.1
		8.519	1.660	355.6	0.1
		7.198	1.476	356.4	0.1
		5.726	1.258	356.6	0.1

Table C.2--continued

Test No.	Atmospheric Pressure (kPa)	$P_i^2-P_e^2$ (10^8 Pa^2)†	Mass Flow Rate (10^{-4} kg/s)	Deformation Aperture (μm)	Normal Stress (MPa)
		4.358	1.025	356.5	0.1
		3.271	0.8324	356.0	0.1
		2.228	0.6273	355.6	0.1
		1.298	0.4189	355.0	0.1
		0.5203	0.2202	354.6	0.1
5	92.11	21.31	2.105	317.4	0.4
		17.80	1.877	317.0	0.4
		14.73	1.676	316.3	0.4
		12.06	1.469	315.1	0.4
		9.646	1.251	315.3	0.4
		7.343	1.039	314.9	0.4
		5.296	0.8234	314.5	0.4
		3.793	0.6379	314.3	0.4
		2.189	0.4191	313.8	0.4
		0.907	0.2122	314.0	0.4
		0.3937	0.1149	313.9	0.4
6	92.14	32.90	2.079	293.3	1.2
		27.95	1.883	293.2	1.2
		23.36	1.674	293.4	1.2
		19.17	1.463	294.3	1.2
		14.98	1.239	294.0	1.2
		11.55	1.031	293.8	1.2
		8.600	0.8358	294.1	1.2
		3.549	0.4297	294.2	1.2
		5.946	0.6359	294.7	1.2
		1.351	0.2045	294.8	1.2
		0.4556	0.1100	294.9	1.2
7	92.14	57.85	2.092	277.2	2.9
		48.67	1.881	276.8	2.9
		39.62	1.659	275.9	2.9
		32.78	1.465	275.4	2.9
		25.66	1.251	275.1	2.9

Table C.2--continued

Test No.	Atmospheric Pressure (kPa)	$p_i^2-p_e^2$ (10^8 Pa^2)[+]	Mass Flow Rate (10^{-4} kg/s)	Deformation Aperture (μm)	Normal Stress (MPa)
		19.24	1.033	274.2	2.9
		14.17	0.8397	273.4	2.9
		9.132	0.6196	273.1	2.9
		5.223	0.4114	272.3	2.9
		2.252	0.2166	271.5	2.9
		2.118	0.1933	270.4	2.9
		1.632	0.1524	269.5	2.9
		1.222	0.1127	267.4	2.9
		1.224	0.1001	265.6	2.9
		0.7372	0.05324	264.6	2.9
8	91.94	97.74	2.077	240.8	5.5
		82.91	1.882	240.6	5.5
		68.32	1.671	239.6	5.5
		55.76	1.467	239.5	5.5
		43.01	1.246	239.1	5.5
		33.13	1.050	238.8	5.5
		23.18	0.8305	238.5	5.5
		9.022	0.4333	237.6	5.5
		15.95	0.6422	237.6	5.5
		3.703	0.2258	237.8	5.5
		2.117	0.1538	237.9	5.5
		1.349	0.1073	237.8	5.5
		0.6052	0.05417	238.2	5.5
9	92.24	178.3	2.085	231.1	9.9
		150.7	1.884	230.1	9.8
		121.9	1.658	230.3	9.8
		99.67	1.465	231.1	9.8
		76.80	1.252	229.7	9.8
		58.22	1.050	229.2	9.8
		39.84	0.8260	228.4	9.8
		15.41	0.4357	227.3	9.8
		26.12	0.6263	226.5	9.8
		5.210	0.2073	226.4	9.8
		6.098	0.2237	225.4	9.8
		3.917	0.1616	224.9	9.8
		2.297	0.1045	224.4	9.8
		0.9851	0.04906	223.9	9.8

Table C.2--continued

Test No.	Atmospheric Pressure (kPa)	$P_i^2-P_e^2$ (10^8 Pa^2)†	Mass Flow Rate (10^{-4} kg/s)	Deformation Aperture (μm)	Normal Stress (MPa)
10	92.02	250.3	2.068	213.0	13.9
		215.1	1.887	212.7	13.8
		175.1	1.681	213.1	13.8
		142.0	1.468	212.2	13.7
		108.4	1.247	212.4	13.7
		79.04	1.026	211.8	13.6
		56.36	0.8255	211.2	13.6
		36.45	0.6191	211.6	13.5
		21.53	0.4348	211.7	13.5
		7.013	0.1973	211.3	13.4
		7.894	0.2161	211.1	13.4
		4.803	0.1500	210.9	13.3
		3.161	0.1076	210.8	13.3
		1.474	0.05433	210.5	13.2
11	91.87	309.2	2.091	204.4	16.6
		253.6	1.861	205.7	16.5
		212.5	1.674	205.6	16.5
		167.2	1.447	205.3	16.5
		131.4	1.255	204.6	16.4
		96.87	1.036	203.4	16.4
		70.64	0.8476	203.5	16.4
		44.67	0.6285	203.5	16.3
		23.41	0.4071	202.9	16.3
		9.951	0.2248	202.2	16.3
		8.219	0.1965	202.2	16.3
		9.627	0.2209	202.0	16.2
		6.066	0.1591	201.5	16.2
		3.567	0.1051	201.2	16.2
		1.632	0.05439	201.7	16.2

*Inner Radius = 0.013 m, Outer Radius = 0.139 m. Injection Pressure Correction: $P_m^2-P_i^2 = 2.476 \times 10^{12} Q_m + 3.233 \times 10^{16} Q_m^{1.9}$

†P_m = measured pressure, P_i = injection pressure, P_e = exhaust pressure (atmospheric)

NRC FORM 335 (6-83) U.S. NUCLEAR REGULATORY COMMISSION

BIBLIOGRAPHIC DATA SHEET

1 REPORT NUMBER (Assigned by TIDC add Vol. No., if any)
NUREG/CR-3680

2 Leave blank

3 TITLE AND SUBTITLE
Relationship Between the Gas Conductivity and Geometry of a Natural Fracture

4 RECIPIENT'S ACCESSION NUMBER

5 DATE REPORT COMPLETED
MONTH January YEAR 1984

6 AUTHOR(S)
Todd W. Schrauf and Daniel D. Evans

7 DATE REPORT ISSUED
MONTH April YEAR 1934

8 PERFORMING ORGANIZATION NAME AND MAILING ADDRESS (Include Zip Code)
Department of Hydrology and Water Resources
University of Arizona
Tucson, Arizona 85721

9 PROJECT/TASK/WORK UNIT NUMBER

10 FIN NUMBER
B 7291

11 SPONSORING ORGANIZATION NAME AND MAILING ADDRESS (Include Zip Code)
Division of Health, Siting and Waste Management
Office of Nuclear Regulatory Research
U.S. Nuclear Regulatory Commission
Washington, D.C. 20555

12a TYPE OF REPORT
Technical

12b PERIOD COVERED (Inclusive dates)

13 SUPPLEMENTARY NOTES

14 ABSTRACT (200 words or less)

In recent years considerable interest in determining the relationship between the hydraulic conductivity of a rock fracture and its average aperture has developed. The present study involved both theoretical and experimental studies of the geometrical factors which influence gas conductivity of rock fractures. Theoretical analysis of parallel plate gas flow revealed that the gas conductivity of a fracture is the same as for incompressible fluids and can be expected to follow a cubic law relationship. Application of the cubic law to practical field test situations, however, was found to be limited by uncertainties in flow boundary conditions, nonlinearity of flow behavior, and effects of fracture surface roughness. Quantitative assessment of uncertainties in flow boundary conditions including elliptical injection boundaries, secondary intersecting fractures, and estimation of effective radius was performed. Nonlinear flow behavior was also analyzed and the results applied to measurements of gas flow rate through a single natural fracture. Evaluation of these results suggested a general flow equation of the form: $-(dp/dx) = av + bv^2$, where a and b are constant coefficients defined by a fracture's average aperture and surface roughness.

15a KEY WORDS AND DOCUMENT ANALYSIS

15b DESCRIPTORS

Fracture Aperture
Gas Conductivity
Gas Flow
Hydraulic Conductivity
Intersecting Fracture Flow System
Parallel Plate Gas Flow

16 AVAILABILITY STATEMENT
UNLIMITED

17 SECURITY CLASSIFICATION (This report) UNCLASSIFIED

18 NUMBER OF PAGES

19 SECURITY CLASSIFICATION (This page) UNCLASSIFIED

20 PRICE
$

UNITED STATES
NUCLEAR REGULATORY COMMISSION
WASHINGTON, D.C. 20555

120555078877 1 1AN
US NRC
ADM-DIV OF TIDC
POLICY & PUB MGT BR-PDR NUREG
W-501
WASHINGTON DC 20555